Nanoscopic Studies of Conjugated Polymer Blends by (Electric) Scanning Probe Microscopy

Dissertation

zur Erlangung des Grades

“Doktor der Naturwissenschaften”

im Promotionsfach Chemie

am Fachbereich Chemie, Pharmazie und Geowissenschaften

der Johannes-Gutenberg-Universität Mainz

Ling Sun (M.Sc.)

geboren in Liaoning, V. R. China

Mainz, 2010

Tag der mündlichen Prüfung: 28. 06. 2010

Table of Contents

Abstract

Conjugated polymers and conjugated polymer blends have attracted great interest due to their potential applications in biosensors and organic electronics. The sub-100 nm morphology of these materials is known to heavily influence their electromechanical properties and the performance of devices they are part of. Electromechanical properties include charge injection, transport, recombination, and trapping, the phase behavior and the mechanical robustness of polymers and blends. Electrical scanning probe microscopy techniques are ideal tools to measure simultaneously electric (conductivity and surface potential) and dielectric (dielectric constant) properties, surface morphology, and mechanical properties of thin films of conjugated polymers and their blends.

In this thesis, I first present a combined topography, Kelvin probe force microscopy (KPFM), and scanning conductive torsion mode microscopy (SCTMM) study on a gold/polystyrene model system. This system is a mimic for conjugated polymer blends where conductive domains (gold nanoparticles) are embedded in a non-conductive matrix (polystyrene film), like for polypyrrole:polystyrene sulfonate (PPy:PSS), and poly(3,4-ethylenedioxythiophene):poly(styrenesulfonate) (PEDOT:PSS). I controlled the nanoscale morphology of the model by varying the distribution of gold nanoparticles in the polystyrene films. I studied the influence of different morphologies on the surface potential measured by KPFM and on the conductivity measured by SCTMM. By the knowledge I gained from analyzing the data of the model system I was able to predict the nanostructure of a homemade PPy:PSS blend.

The morphologic, electric, and dielectric properties of water based conjugated polymer blends, e.g. PPy:PSS or PEDOT:PSS, are known to be influenced by their water content. These properties also influence the macroscopic performance when

the polymer blends are employed in a device. In the second part I therefore present an *in situ* humidity-dependence study on PPy:PSS films spin-coated and drop-coated on hydrophobic highly ordered pyrolytic graphite substrates by KPFM. I additionally used a particular KPFM mode that detects the second harmonic electrostatic force. With this, I obtained images of dielectric constants of samples. Upon increasing relative humidity, the surface morphology and composition of the films changed. I also observed that relative humidity affected thermally unannealed and annealed PPy:PSS films differently.

The conductivity of a conjugated polymer may change once it is embedded in a non-conductive matrix, like for PPy embedded in PSS. To measure the conductivity of single conjugated polymer particles, in the third part, I present a direct method based on microscopic four-point probes. I started with metal core-shell and metal bulk particles as models, and measured their conductivities. The study could be extended to measure conductivity of single PPy particles (core-shell and bulk) with a diameter of a few micrometers.

Introduction

What is a conjugated polymer?

Conjugated polymers are a family of polymers containing delocalized π electrons in the backbone.[1,2] After chemically or electrochemically doped, conjugated polymers can become electrically conductive.[3-5] Most conjugated polymers are insoluble and infusible due to their rigid molecular structure. However, after substituted by flexible side chains (e.g. long alkyl or alkoxy side chains), these polymers can be processed, e.g. spin-coated or ink-jetted, from solutions.[5,6] Conjugated polymers are considered a most promising candidate in applications of biosensors and organic electronics due to their mechanical flexibility, processability, chemical tunability, and low cost.[6-9]

The first conjugated polymer that could be made conductive, polyacetylene was reported in the early 1970s by Shirakawa and co-workers using soluble Ziegler-type catalysts.[1,10] Heeger, MacDiarmid, and Shirakawa extended the study by doping *trans*-polyacetylene (**Figure 1**) with halogens.[3] By controlling the doping level, they were able to tune polyacetylene derivatives from insulators to plastic metals. Heeger, MacDiarmid, and Shirakawa were awarded the Nobel Prize in Chemistry in 2000 "for the discovery and development of conductive polymers". The application of conjugated polymers in optoelectronic devices started from the discovery of photo induced electron transfer from poly[2-methoxy,5-(2'-ethyl-hexyloxy)-p-phenylene vinylene] (MEH-PPV) to fullerene.[2] Since then, more and more conjugated polymers and their derivatives have been synthesized. Typical conjugated polymers include PPV derivatives, polythiophene derivatives,[11] polypyrrole (PPy) derivatives[12], polyaniline derivatives, and polyfluorene derivatives[5] (**Figure 1**).

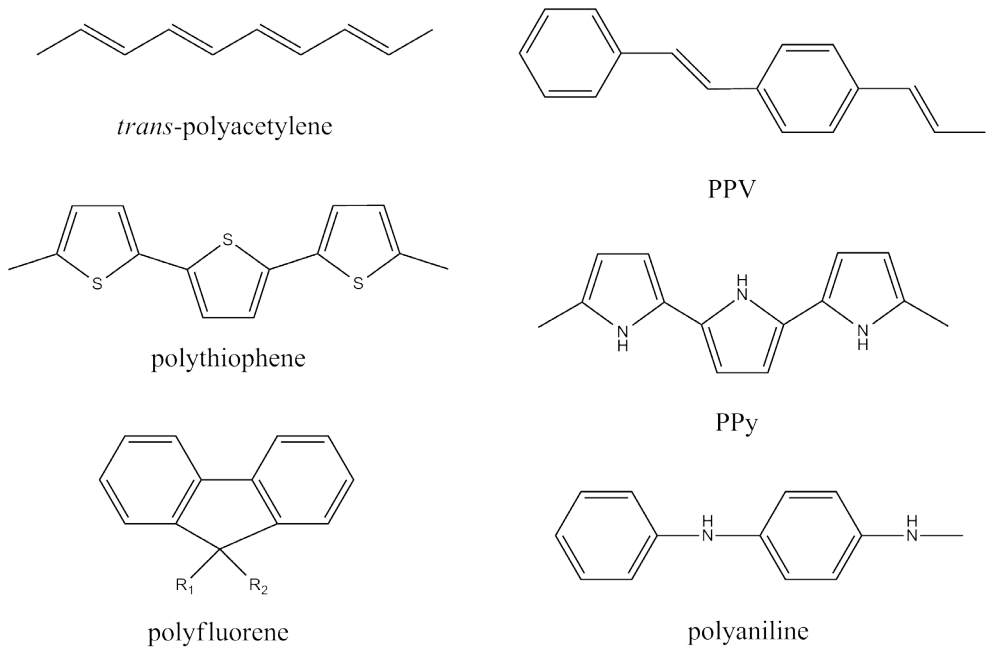

Figure 1. Molecular structures of typical conjugated polymers.

What is a conjugated polymer blend?

A polymer blend is a polymer alloy, in which two or more polymers are mixed to achieve desired properties without synthesizing new polymers. If at least one of the components in the blend is a conjugated polymer, this blend is called conjugated polymer blend. Although conjugated polymers with long side chains are flexible and soluble, the conductivity of the polymers is reduced by several orders of magnitude after substitution of the side chains.[5] Probably, the side chains distort the electron conjugation in the backbone, which reduces the conductivity of the polymer. After blended (or doped) by a counter ion made of a polymer, the conductivity of the blend is maintained and the solubility of it is increased compared to the original conjugated polymer.[6] The blending may also produce optimized optoelectronic properties by combining polymers with different electrical properties.[6,13-15]

For instance, poly(3-hexylthiophene):6,6-phenyl-C_{61} butyric acid methyl ester (P3HT:PCBM) (**Figure 2**) is a typical conjugated polymer blend used in bulk heterojunction solar cells.[15] P3HT acts as an electron donor and PCBM as an

electron acceptor. Due to the nanoscopic heterojunction of the P3HT:PCBM blend, the photo-generated excitons (electrically neutral electron-hole pairs) could reach the electron donors (P3HT) and acceptors (PCBM) and dissociate into electrons and holes before quenching (the diffusion length is ~10 nm). Solar cells of high efficiency (the external efficiency is up to 7.4%) can thus be produced by using conjugated polymer blend with such morphological and electrical properties.[6,15]

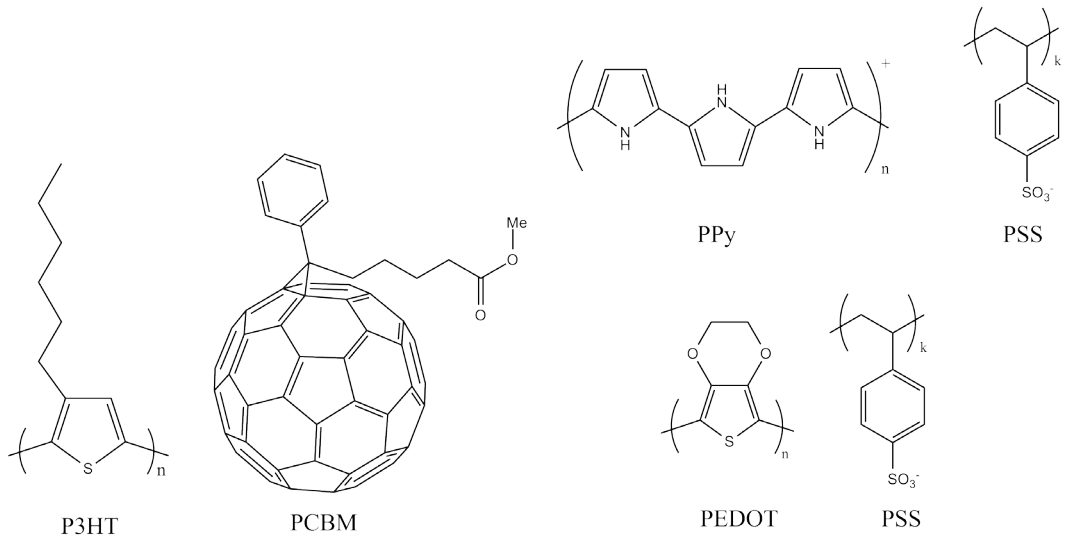

Figure 2. Molecular structures of typical conjugated polymer blends.

Another example is poly(3,4-ethylenedioxythiophene):poly(styrenesulfonate) (PEDOT:PSS[16], **Figure 2**), a water soluble polymer blend. In PEDOT:PSS, the conductive PEDOT is responsible for the electric charge transfer, and the non-conductive PSS allows the blend to be solubilized in water. PEDOT:PSS is typically used as a hole transport (electron blocking) or a buffer layer on indium tin oxide (ITO) electrodes in field effect transistors (FETs), organic light-emitting diodes (OLEDs) and solar cells.[17-19] In order to maintain a relatively high conductivity, PEDOT:PSS is acidic (the excess PSS is in its acidic form).[20] The acidic nature of PEDOT:PSS could cause degradation of ITO at the PEDOT:PSS/ITO interface during spin-coating, leading to reduced lifetime and efficiency of the semi-conductive devices.[21,22] Further, the devices using PEDOT:PSS show leakage current at the ITO anode, which decreases the

efficiency in blocking electrons.[22,23]

PPy doped by PSS (**Figure 2**) is pH neutral and could also be used as a hole transport layer in OLEDs, for example. The performance of devices using PPy:PSS was reported to be similar to those using PEDOT:PSS, and the leakage current lower.[24-26] Some advantages of PPy:PSS over PEDOT:PSS make it a potential alternative of PEDOT:PSS for some applications.

Why and how to correlate electric properties and nanoscopic morphology of conjugated polymer blends?

The distribution of conductive domains inside the non-conductive matrix or the local arrangement of electron donors and acceptors determine the nanoscopic electric (surface potential and conductivity) or dielectric (dielectric constant) properties of conjugated polymer blends.[4,6,15] When applied in semi-conductor devices, these electric and dielectric properties of the blend determine efficiency and lifetime of a device. For this reason, characterizing surface and interface properties of conjugated polymers and conjugated polymer blends is of paramount importance for understanding the functioning of devices. Electron microscopy techniques, x-ray techniques, and scanning probe microscopy techniques are most commonly used for this purpose.

Electron microscopy techniques: In an electron microscope, an electron beam is focused on a sample surface or inside a thin film. The scattered or transmitted electrons at each position are collected and the intensity of the electrons is analyzed, which provide the morphologic information of a sample.[27] Electron microscopy techniques include transmission electron microscopy (TEM), Scanning electron microscopy (SEM), and energy dispersive x-ray spectroscopy (EDX). TEM is used to characterize morphology of thin films (the maximum thickness is 50 μm) with a lateral resolution of ~2 nm.[27] SEM is used to characterize topography of conductive and semi-conductive samples. The resolution of SEM is usually one order of magnitude lower than that of TEM. However, SEM is not

restricted to measurements of thin films and can be used to characterize bulk samples. When the energy of the electron beam is high enough, electrons in the inner shell of the atom can be ionized. The electron in the outer shell fills the hole in the inner shell, which results in characteristic x-ray from the surface of the sample. The technique that detects such characteristic x-ray is called EDX, which is used to quantitatively analyze elemental compositions of the sample.[27] The penetration depth of the electron beam of EDX measurements is usually several micrometers.[27] The major disadvantage that the electron microcopy techniques suffer is that electron beams could damage the polymer samples.

X-ray techniques: Ever since the discovery of x-rays in 1895, many techniques based on x-rays have been developed, e.g. x-ray diffraction (XRD), small/wide-angle x-ray scattering (SAXS/WAXS), and x-ray photoelectron spectroscopy (XPS). In XRD, a coherent x-ray beam is directed onto a sample. The pattern of the diffracted beam is recorded, reflecting the crystalline structure of the sample. Depending on the intensity and angle of the incident beam, the penetration depth of x-rays can be limited to only 10 – 100 nm. XRD thus can be used to measure the orientation and crystal structure of crystalline components in conjugated polymer blends.[28-30] In SAXS or WAXS the elastic scattering of the incident x-rays is recorded at a small or at a wide angle (0.1° – 10°). The intensity of the scattered x-ray depends on the electron density of the sample materials. SAXS and WAXS are thus used to determine average domain sizes and inter-domain distances of conjugated polymer blends.[31,32] In XPS, x-ray beams irradiate the top layers (1 – 10 nm) of a sample. By measuring the kinetic energy and the number of the irradiated electrons, one could calculate the binding energy of them.[33] XPS is thus used to quantitatively analyze the average elemental composition of the sample surface (the minimal measure area is 10 – 200 nm).[34,35] The above mentioned x-ray techniques are considered non-destructive to sample surfaces, since x-rays of low energy (0.12 – 12 keV) are used for the measurements.[28-30]

Scanning probe microscopy techniques: Although electron microscopy and

x-ray techniques are widely used for characterizing conjugated polymers and their blends, they are not capable of correlating local morphology and electric properties. As surface characterization method with a high spatial resolution (of order of few nanometers), scanning probe microscopy techniques could provide such a critical link.[6,15,36,37] Electrical scanning probe microscopy is considered an ideal tool to measure simultaneously electric properties and surface morphology on the nanoscale. For instance, scanning tunneling microscopy (STM) measures the local density of states of a sample, which can be used to study the local charge transport.[37-39] Contact mode conductive atomic force microscopy (c-AFM) and scanning conductive torsional mode microscopy (SCTMM) are used to measure the currents, and thus charge transport, between a very sharp conductive tip and a sample.[37,39-43] Kelvin probe force microscopy (KPFM) is used to measure surface potentials and their variations of samples.[42,44,45] A more detailed description of the scanning probe microscopy techniques will be provided in **Chapter 1**.

Motivation

As previously written, PPy:PSS could be a promising substitute for PEDOT:PSS for making hole transport layers in applications in organic electronics. To optimize the properties of this material and to extend its application range, a thorough study of electric (surface potential and conductivity), dielectric (dielectric constant) and morphologic properties of PPy:PSS is required. In this thesis I used AFM, KPFM and c-AFM/SCTMM to study the electric, the dielectric and the morphologic properties of PPy:PSS films (thickness between 1 and 80 nm) on the nanoscale.

KPFM and c-AFM/SCTMM are widely used to characterize conjugated polymer blends, however both have limitations. The resolution and accuracy of KPFM and c-AFM/SCTMM are influenced by the nanoscopic heterogeneity of the materials. For instance, with c-AFM or SCTMM information on conductive domains (PPy) is not always accessible if they are embedded inside a non-conductive matrix (PSS) and do not form a conducting channel (percolation path) through the sample. The surface potential measured by KPFM is a weighted average of the surface potentials generated by the area (conductive or not) close to the apex of the sensing tip, resulting in a spatial resolution of up to a few hundred nanometers.[46,47] Thus when the distance between two adjacent PPy domains is beyond the resolution of KPFM, the measured surface potential turns out to be the convolution of two domains, leading to ambiguous results.

To overcome such limitations, I first performed a combined analysis by KPFM and c-AFM/SCTMM on a model system with controlled nanoscopic morphology and known electric properties. I used gold particles with diameters of around 20 - 30 nm and embedded them in thin polystyrene films. The size of the gold particles is similar to that of the PPy domains. Au is chemically inert in air

and with well known electric properties. Using the knowledge from the model Au/PS system I could study the nanoscopic correlation between electric properties and morphology of PPy:PSS films.

Water content is known to influence morphologic, electric and dielectric properties of conjugated polymers, which is especially an issue for water based PEDOT:PSS and PPy:PSS solutions.[48] Only a few studies have been carried out on this topic.[9,34,49-51] Most work was carried out without directly correlating topography and electric (or dielectric) properties. A thorough nanoscopic study of water-affected morphologic and electric properties is still missing.

The dielectric interaction between tip and sample during a KPFM measurement is sensitive to water content of the sample and can be used to study the dielectric constant of materials.[52,53] Since PSS is more hydrophilic while PPy is more hydrophobic,[49,54] they would show a different response to water. By performing an *in situ* KPFM measurement on PPy:PSS films at different relative humidity, I could correlate the influence of relative humidity on topography and dielectric constants of PPy:PSS films.

The conductivity of PPy may change after it is embedded in the non-conductive PSS matrix due to the electrostatic coupling between PPy and PSS. Very few studies have been carried out to characterize the conductivity of single molecules, nanoparticles or conductive domains.[55-58] In most work, the conductive component (molecules, nanoparticles or domains) was connected to two point electrodes and a current was measured with an applied DC voltage. The small contact area (from a few nanometers to sever micrometers square) between the electrode and the conductive component could result in non-negligible contact resistance between them. In this thesis I thus present a new method I developed to measure the nanoscopic conductivity of Ag core-shell and Au bulk particles by microscopic four-point probes. The method is intended to measure conductivity of single PPy particles with a diameter of a few micrometers.

Outline

The structure of this thesis is as follows:

In **Chapter 1** I introduce scanning probe microscopy techniques, in terms of STM, AFM, contact mode c-AFM, SCTMM and KPFM.

In **Chapter 2** I introduce materials I used and sample preparation procedures.

In **Chapter 3** I introduce a combined study of KPFM and SCTMM on the Au/PS model system. I also apply the knowledge I gained from the model system to interpret KPFM and SCTMM data of homemade PPy:PSS films.

In **Chapter 4** I introduce the influence of humidity on topography and dielectric constants of PPy:PSS films by KPFM using dielectric imaging. I compare results of thick and thin PPy:PSS films, as well as annealed and unannealed PPy:PSS films

In **Chapter 5** I introduce how to measure the nanoscopic conductivity of single particles by microscopic four-point probe method. I use Ag core-shell particles and Au bulk particles as models and measure their conductivities.

In **Chapter 6** I give general conclusions and outlook.

Chapter 1 Scanning Probe Microscopy Techniques

1.1 Scanning tunneling microscopy

Scanning tunneling microscopy (STM) was invented by Binnig and Rohrer in the early 1980s.[59,60] In STM, an atomically sharp conductive tip is brought close (0.5 – 2 nm) to a conductive sample surface. With a constant voltage V applied between tip and sample, electrons tunnel through the air gap between them.[61] The tunneling current I decays exponentially with increasing tip-sample distance z,[59,60]

$$I \propto V\rho \exp(-2\kappa z), \text{ with } \kappa = \frac{\sqrt{2mE}}{\hbar}. \quad (1.1)$$

Here ρ represents the local density of states of a sample, m is the electron mass, E is the barrier height for electron tunneling, and $\hbar$ is the reduced Planck constant. The tunneling current is kept constant by adjusting z, and the 3D motion of the tip (sample is kept still) is recorded as STM image. Since the tunneling current depends on ρ and z, the measured STM image contains information of topography and electronic structures of samples. If V, ρ, and κ are kept constant, a change of 0.1 nm in z results in one order of magnitude change in I (**Equation 1.1**). The vertical resolution of STM thus can reach down to ~0.01 nm.[62] The lateral resolution (typically ~0.1 nm) of STM is limited by the tip radius. Usually electrochemically etched tungsten or platinum tips (ideally only one atom at the end of the tip) are used. A clean environment is also important for high resolution STM imaging. As a consequence STM is usually performed in ultra high vacuum (UHV). STM can be used to study the heterogeneity in charge transport of conjugated polymers.[37-39]

1.2 Atomic force microscopy

1.2.1 Introduction

Atomic force microscopy (AFM) was invented by Binnig *et al*.[63] In an AFM setup, a laser beam is pointed onto the back side of a cantilever and reflected to a quadrant photo detector (**Figure 1.1**). When the cantilever is scanning over the sample surface (controlled by a piezo scanner), its 3D motion is detected by the laser beam reflected on the photo diode detector. The motion of the cantilever (deflection or oscillation) is used as topographic feedback (will be introduced later). The cantilever and the sample are thus not necessarily conductive. Typical cantilevers used in AFM are made of silicon or silicon nitride, with tip radius of a few to tens of nanometers.

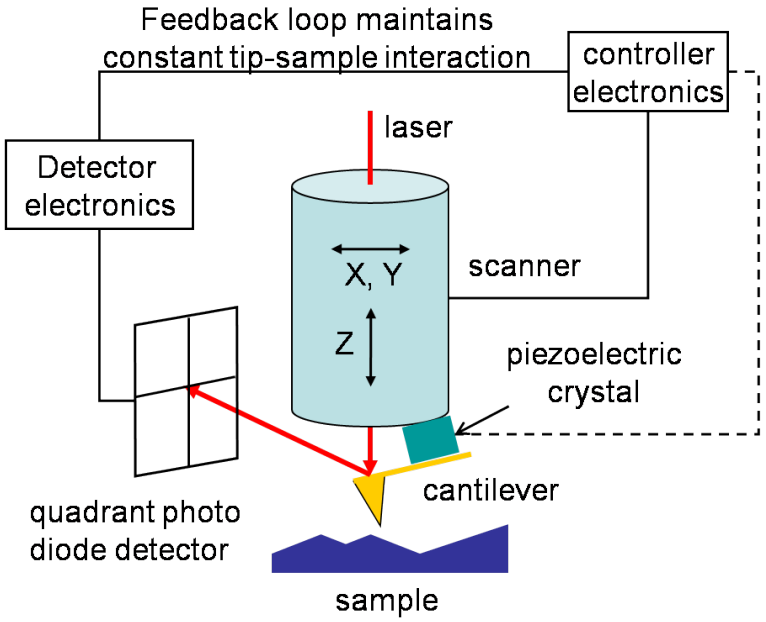

Figure 1.1. A schematic sketch of an AFM setup: solid lines, static mode; solid and dashed lines, dynamic mode.

1.2.2 Imaging modes

AFM imaging modes can be divided in static and dynamic. In the static mode the tip is in mechanical contact with the sample surface and repulsive forces are dominant. During the measurement, the tip-sample interaction causes a bending of the cantilever according to Hooke's law,

$$F = -k\Delta z \,. \tag{1.2}$$

where k is the spring constant of the cantilever and Δz is the bending distance of the cantilever. There are constant force mode and constant height mode in contact mode AFM. In the constant force mode, the vertical position of the tip is adjusted to keep the tip-sample interaction (i.e. Δz) constant. The 3D motion of the tip is thus recorded as a topography image. In the constant height mode, the vertical position of the tip is kept constant, and Δz of the cantilever is recorded as an image, which also reflects topography of samples. Typically soft cantilevers with $k < 1$ N/m are used in contact mode to avoid mechanical damage to sample surfaces. However the imaging force (1 – 10 nN/nm) in this mode is still too high for soft materials like polymers or biomaterials.

The dynamic modes are the amplitude modulation (AM) mode[64,65] and the frequency modulation (FM) mode[66]. In AM mode (also called AC mode or tapping mode® by some manufacturers), the cantilever is oscillated at (or very close to) its fundamental resonance frequency f_0 (50 – 400 kHz) by a piezoelectric crystal fixed under the cantilever holder (**Fig. 1.1**).[67] When the tip approaches the sample surface, the tip-sample interaction (at intermediate distance) results in shifts of oscillation amplitude, frequency and phase. The oscillation amplitude is detected by a lock-in amplifier and kept constant by adjusting tip-sample distance. Topography of samples is measured according to the 3D motion of the cantilever. One could record a phase image simultaneously with the topography image by measuring the phase shift of the tip oscillation with respect to the driving oscillation. The phase shift reflect variations of material properties, in terms of composition, adhesion, viscoelasticity, and etc.[68] However, it is still not clear that which force or material property (adhesion or viscoelasticity) dominates the measured phase image. In AM-AFM, the tip "taps" (intermittent contact) the sample surface instead of continuously contacting it, which reduces the imaging forces.[67] Soft cantilevers ($k < 1$ N/m) may be completely trapped to the sample surface due to attractive forces between tip and sample. Typically stiff cantilevers with $k \approx 40$ N/m are used in AM-AFM. AM-AFM can be used to image polymers

and biomaterials without damaging the sample surfaces.

In FM mode (also called non-contact mode by some manufacturers), the cantilever is oscillated at its resonance frequency (100 – 400 kHz), which is slightly different from its fundamental resonance frequency due to the tip-sample interaction. The excitation signal is controlled by a feedback loop to keep the oscillation amplitude (<10 nm) constant. The tip is 1 – 10 nm away from the sample surface, where attractive forces (on the order of pN) are dominant. The gradient of forces between tip and sample with respect to tip-sample distance is proportional to the shift of the oscillation frequency,[66]

$$\Delta f \propto -f_0 \frac{\partial F}{\partial z}. \tag{1.3}$$

The topography of samples is measured by regulating the tip-sample distance to maintain a constant Δf.

In AM-AFM the detection bandwidth (available bandwidth for detection) is restricted by the quality factor (the resonance frequency with respect to the bandwidth of the oscillation) of the cantilever, i.e. the higher the quality factor, the smaller the detection bandwidth.[66,68] The smaller bandwidth results in a longer measurement time, which is not practically favored. In FM-AFM, however, the bandwidth of the frequency demodulation detector is not restricted by the cantilever quality factor. The sensitivity of detecting Δf can thus be improved by using a cantilever with higher quality factor (~10^4),[66,68] providing higher spatial resolution. High resolution (e.g. atomic resolution) FM-AFM is usually performed in UHV.

1.3 Conductive atomic force microscopy

1.3.1 Contact mode c-AFM

Measurements of local resistance or conductivity of conjugated polymers and polymer blends are of great interest. Although STM could resolve the electric properties of samples with atomic resolution,[37,40] the use of tunneling current as the

feedback signal limits its application to conductive materials. It is difficult to measure samples mixed with conductive and non-conductive components, like PEDOT:PSS or PPy:PSS, by STM. Also, by STM one cannot measure the "physical topography" of samples, as stated previously.

The disadvantages of STM are overcome by contact mode c-AFM, which combines contact mode AFM with a voltage/current sensing capability.[69,70] In contact mode c-AFM, the deflection of the cantilever is used as the feedback signal instead of the tunneling current. A DC bias voltage *V* is applied to an electrode below the sample and the current is measured upon the formation of a percolation path, or a conducting channel, between tip apex and electrode (**Figure 1.2**). The current mapped over the scan area is recorded as a current image, which is obtained simultaneously with the topography image. In addition to current mapping, local current-voltage (*I*-*V*) curves can also be obtained by contact mode c-AFM. This is done by positioning the tip at a selected point, and by measuring the variation of *I* upon applying a potential *V*. *I*-*V* curves can be used, e.g., to calculate the local charge carrier mobility of conjugated polymers by the Mott-Gurney equation (Child's law).[37,61,71]

The contact force in c-AFM should be kept relatively small in order not to damage the sample. On the other hand, a bigger contact force could increase the contact area and improve the electric contact between tip and sample, which would influence the resolution of the current imaging.[69,70] Appropriate contact forces would typically be 1 nN – 1 μN. Such forces are large enough to ensure good ohmic contact between tip and surface, but they are still small enough for avoiding damage to the sample. The technique works best for hard conducting surfaces because there the limitation of small contact forces does not apply. It is not suited to study too soft surfaces or surfaces with weakly bonded structures, i.e. polymers, DNA, or carbon nanowires, which might be scratched by the tip.

1.3.2 Scanning conductive torsion mode microscopy

In intermittent or non-contact imaging modes the forces between tip and

surfaces are minimal. However, in intermittent-contact mode the vertical oscillation amplitude of the cantilever is 30 – 100 nm. In only 1% of the oscillation cycle, the tip contacts the sample.[72] While in non-contact mode, there is no mechanical contact between tip and sample at all. Both modes are not suitable for current measurements, in which a small tip-sample distance (a few nanometers) is required.

The cantilever can also be excited at its first torsional frequency by two anti-parallel driven piezoelectric crystals attached to the cantilever holder (**Figure 1.2** inset).[73,74] When the tip is scanning over a sample surface, the tip-sample interaction cause changes in the torsional oscillation amplitude. By adjusting the tip-sample distance the torsional amplitude can be kept constant, by which topography of the sample is measured.[73,74] During the torsional vibration, the vertical oscillation amplitude (perpendicular to the sample surface) of the cantilever is only a few nanometers, providing the possibility for current measurements.[72-74]

Harris *et al.* combined torsional AFM with current/voltage sensing devices, and obtained topography and current images simultaneously (**Figure 1.2**).[72] This method is called torsional TUNA® or scanning conductive torsional mode microscopy[41] (SCTMM). The current measured in SCTMM is due to tunneling of electrons across the air gap between tip and sample. If all other parameters (tip conductivity, sample conductivity and applied voltage) are kept constant, the current measured by SCTMM could be several orders of magnitude lower than that measured by contact mode c-AFM.[41] The much lower current measured in SCTMM results from a larger tip-sample distance in SCTMM measurements than that in c-AFM measurements, as described in **Equation 1.1**.[59,60] Nevertheless, since it employs low imaging forces, SCTMM allows local current measurements of nanoparticles, conjugated polymer blends and nanorods.[41-43]

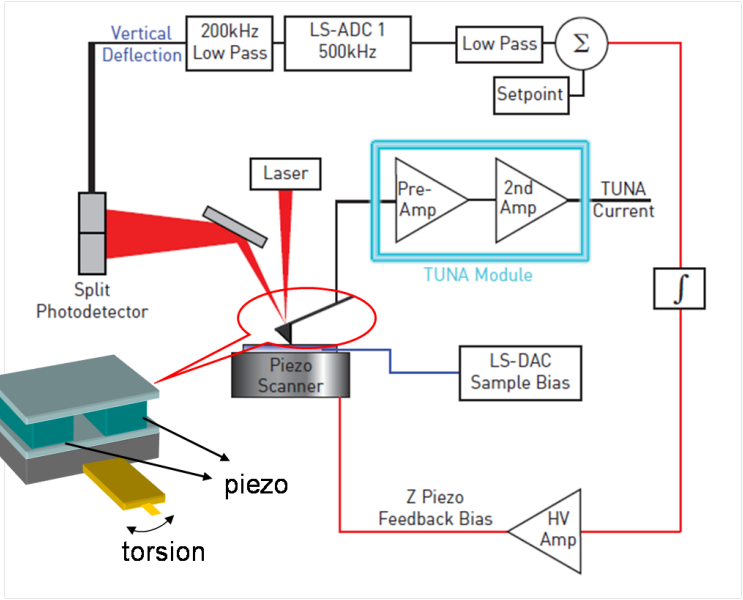

Figure 1.2. The configuration of a conventional contact mode c-AFM setup.[72] Copyright 2007 Veeco instruments Inc. Inset: cartoon of two piezos attached to the cantilever holder for a torsional mode excitation.

1.4 Kelvin probe force microscopy

The operation of KPFM is based on dynamic mode AFM, by which topography is measured. In this section, I will focus on how the surface potential is measured and how to distinguish signals induced by electrostatic force (used for surface potential imaging) from those by other forces (used for topographic imaging) in the intermittent contact region.

1.4.1 Basic principles of KPFM

I start with introduction of the material work function. The work function represents the minimal energy required to remove one electron from its Fermi level ε_f to vacuum ε_{Vac} (**Figure 1.3**). In KPFM a plate capacitor with a capacitance C is considered with tip and sample as two electrodes. Φ_t and Φ_s represent the work functions of the tip and the sample respectively (**Figure 1.3a**). When the tip is electrically wired to the sample, electrons start to transfer from a material of lower work function to a material of higher work function. For $\Phi_t > \Phi_s$, electrons transfer

from the sample to the tip, and vice versa for $\Phi_t < \Phi_s$. The Fermi levels of the tip and the sample start to align, leading to a difference in their local vacuum levels (**Figure 1.3b**). This difference is called contact potential difference,[75]

$$V_{CPD} = \frac{1}{e}(\Phi_s - \Phi_t), \tag{1.4}$$

where e is the elementary charge. Tip and sample are thus charged, resulting in an electrostatic force between them. The electrostatic force can be nullified by an external DC bias V_{dc} applied to the cantilever (**Figure 1.3c**).

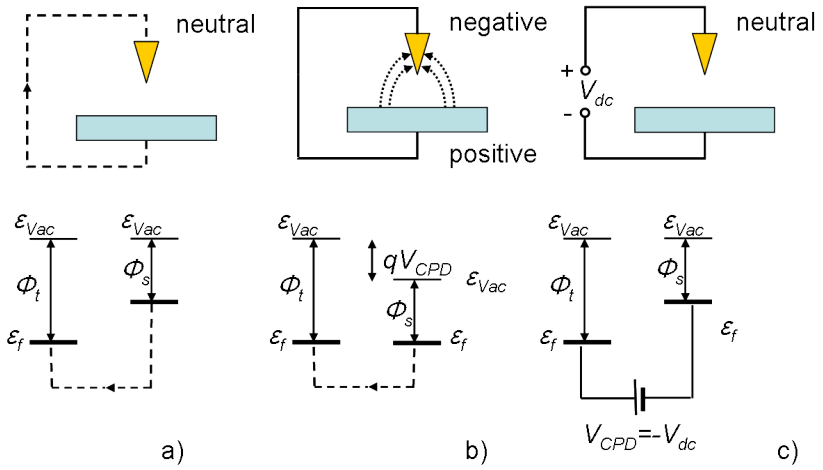

Figure 1.3. Schematic sketches of energy levels of tip and sample: a) the tip and the sample are not in contact; b) the tip and the sample are electrically wired; c) an external voltage V_{dc} is applied to the cantilever.

The electrostatic force between tip and sample contains three components: a topographic, an electronic and a dielectric one. To discern among them, an AC voltage $V_{ac}\sin(\omega t)$ is also applied to the cantilever, which oscillates the cantilever electrically.[76] The resulting electrostatic force between tip and sample is[45]

$$F_e = -\frac{1}{2}\frac{\partial C}{\partial z}\left[(V_{dc} - V_{CPD} + V_{ac}\sin(\omega t)\right]^2. \tag{1.5}$$

Here ω is the modulation frequency, and t is time. The three terms of the electrostatic force between tip and sample are:

$$F_{dc} = -\frac{\partial C}{\partial z}\left[\frac{1}{2}(V_{dc} - V_{CPD})^2 + \frac{1}{4}V_{ac}^2\right], \tag{1.6}$$

$$F_{\omega} = -\frac{1}{2}\frac{\partial C}{\partial z}(V_{dc} - V_{CPD})V_{ac}\sin(\omega t), \tag{1.7}$$

$$F_{2\omega} = \frac{1}{4}\frac{\partial C}{\partial z}V_{ac}^2\cos(2\omega t). \tag{1.8}$$

Equation 1.6 represents the topographic term, **Equation 1.7** the electronic one, and **Equation 1.8** the dielectric one.

The first harmonic term of the electrostatic force F_ω is nullified by monitoring $V_{dc} = V_{CPD}$, which is then recorded as a surface potential image (contact potential difference between tip and sample). If Φ_t is known, Φ_s can be calculated by

$$\Phi_s = \Phi_t - eV_{dc}. \tag{1.9}$$

Φ_t can be calibrated by a material with known work function, e.g. freshly cleaved graphite.

Although **Equation 1.7** is commonly accepted in KPFM, it is only strictly correct when a metallic tip-sample system is concerned. In a system of a metallic tip and a semi-conductive sample, capacitors in series connection should be considered. F_ω is thus expressed as,[77]

$$F_{\omega} = \frac{Q_s}{\varepsilon_0}C_{eff}V_{ac}\sin\omega t. \tag{1.10}$$

Here Q_s is surface charge of the sample, C_{eff} is effective capacitance of the capacitors, and ε_0 is vacuum permittivity. For a metallic tip-sample system,

$$Q_s = -C(V_{dc} - V_{CPD}). \tag{1.11}$$

Equation 1.10 thus reduces to **Equation 1.7**. The minus sign in front of V_{CPD} in **Equations 1.5**, **1.6**, **1.7** and **1.11** will be positive if V_{dc} is applied to the sample.

Since no current flows between tip and sample in KPFM measurements, samples do not need to be conductive. KPFM can probe material work functions,[78] doping levels of semiconductors,[79,80] surface potential distributions of conjugated polymer blends,[42] and dipole moments of insulators.[81] If conjugated polymers (or

polymer blends) are inserted in active devices, KPFM can also be used to study the nanoscopic charge transport and trapping, as well as photovoltaic properties of the polymers (or the blends).[37,82]

1.4.2 Detection of V_{CPD}

F_ω between tip and sample causes changes of amplitude and frequency of the electrically driven oscillation. Similar as dynamic AFM, in KPFM there are also AM mode and FM mode for detecting V_{CPD}. In AM-KPFM, the amplitude of the electrically driven oscillation is detected. By adjusting $V_{dc} = V_{CPD}$ F_ω is nullified, and thus the amplitude shift induced by it. Depending on the manufacturer, AM-KPFM can be realized in the "two-pass" mode[83] and the "single-pass" mode[84]. In the "two-pass" mode, the topography of the sample is measured during the first scan along a line, and the surface potential during the second (repeated) scan of the same line (also the same lock-in amplifier is used). In the second scan, the piezoelectric crystal stops to oscillate the cantilever. Instead an AC voltage (1 – 5V) modulated at ω is used to oscillate the cantilever. The cantilever is lifted by a defined distance (1 – 100 nm, non-contact) and driven to follow the topography obtained in the first scan. This way, the "cross-talk" of surface potential with topography could be minimized.[46] In "two-pass" AM-KPFM, ω is set to $2\pi f_0$ of the cantilever in order to obtain a strong oscillation signal.[85]

In the "single-pass" mode, topography and surface potential are measured simultaneously by two lock-in amplifiers. The cantilever is simultaneously oscillated by the piezoelectric crystal and by the AC voltage (1 – 5 V). ω is set to a frequency between 20 and 30 kHz, which is much lower than f_0 in order to distinguish between amplitude shifts induced by the electrostatic force and by other forces in the intermittent contact region (used for topographic feedback).[75] In order to obtain a strong oscillation signal and to separate from f_0, one could also set ω to the second fundamental resonance frequency of the cantilever.[86] This way, the "cross-stalk" between surface potential and topography can be avoided.

In AM-KPFM, the electrostatic force is due to an electric field formed

between tip and sample. Hence the tip apex, the tip shaft, and the cantilever all contribute to the electric field.[45,47] The measured surface potential is thus a weighted average of all the surface potentials generated in proximity to the tip apex.[46] Results obtained by AM-KPFM cannot be used for quantitative analysis (e.g. measuring work function of materials) directly. Several attempts have been made to extract the "real" surface potential from the "measured" surface potential.[46,47] Those methods, however, require 2D or 3D simulations, and the parameters for the simulations vary for different systems.

In FM-KPFM (single-pass), the system detects the frequency shift induced by the gradient of the electrostatic force with respect to tip-sample distance (**Equation 1.3**).[87,88] Since F_e is modulated at ω and 2ω, the oscillation frequency of the cantilever is also modulated at ω and 2ω by $\partial F_\omega / \partial z$ and by $\partial F_{2\omega} / \partial z$, leading to side peaks at $f_0 \pm \omega/2\pi$ and $f_0 \pm \omega/\pi$ (**Figure 1.4**).[88] When $V_{dc} = V_{CPD}$, the side peaks at $f_0 \pm \omega/2\pi$ disappear, and surface potential (V_{CPD}) is recorded.

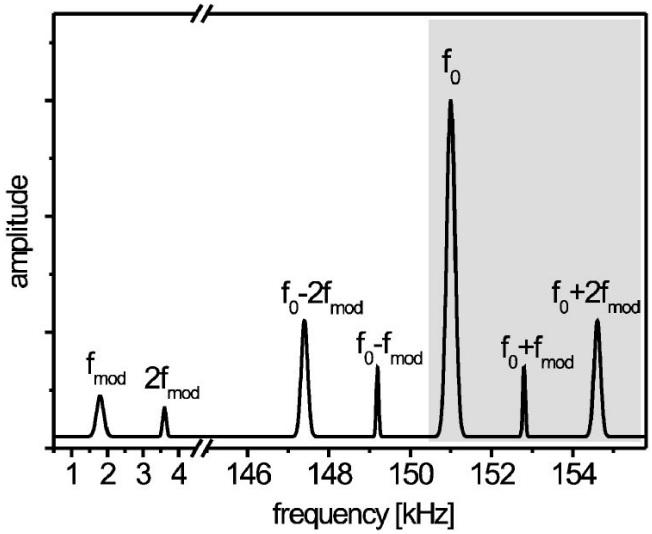

Figure 1.4. A schematic frequency spectrum of the tip oscillation with a modulation frequency of $f_{mod} = \omega / 2\pi$.[88] Copyright 2005 The American Physical Society.

ω is restricted to 1 - 5 kHz in FM-KPFM.[75] For a lower ω, $f_0 \pm \omega/2\pi$ may not be distinguished from f_0 by the frequency demodulation detector, leading to

cross-talk between surface potential and topography.[75] The upper limit of ω is constrained by the bandwidth of the frequency demodulation detector (~500 Hz). Typically a smaller V_{ac} (1 – 2 V) is used in FM-KPFM, since the detection of the force gradient is more sensitive than that of the force, as explained previously. The smaller AC voltage contributes less to the topographic term (**Equation 1.6**), and influences electronic structures of samples less.[84] The way that a force gradient is detected also minimizes the contributions of the shaft and the lever of the cantilever to the measured surface potential. The lateral resolution of FM-KPFM is thus improved down to ~10 nm and the vertical resolution is down to ~5 mV when performed in UHV.[88] To this end, FM-KPFM is superior to AM-KPFM.

1.4.3 Detection of $F_{2\omega}$

$F_{2\omega}$ induces an amplitude shift at 2ω, $\Delta A_{2\omega}$, which is proportional to $F_{2\omega}$.[53] During the KPFM measurement, V_{dc} is monitored to nullify F_{ω} and $\Delta A_{2\omega}$ can be detected by an additional lock-in amplifier. If V_{ac} is kept constant, changes of $F_{2\omega}$ only result from changes of $\partial C / \partial z$ (**Equation 1.8**). In a system of a metallic tip and a semi-conductive sample, C_{eff} replaces C in **Equation 1.8**. A complete expression of $F_{2\omega}$ for the metallic-semiconductive system depends on individual system studied, which will be introduced in **Chapter 4**. Measurements of $F_{2\omega}$ can be used to characterize local dielectric properties (e.g. dielectric constant) and their variations of samples.[53,89,90]

In the KPFM modes introduced previously, topography (height image) is obtained by maintaining a constant tip-sample interaction (except for the electrostatic interaction). The height image can also be obtained by adjusting the tip-sample distance to maintain a constant $F_{2\omega}$. The measured height image in this way contains information of topography and polarizability of samples.[79,91] Some people also call this imaging method as scanning polarization force microscopy.[52]

Chapter 2 Materials and Sample Preparations

2.1 Materials

The gold nanoparticles (AuNPs) and the conjugated polymer blend (PPy:PSS) introduced in this chapter were synthesized by Jianjun Wang.

2.1.1 Gold nanoparticles

The aqueous colloidal gold suspension was prepared according to Frens' method.[92] Solid sodium citrate ($Na_3C_6H_5O_7$) was added directly into a boiling solution of 500 ml chloroauric acid ($HAuCl_4$). The ratio of the sodium citrate was varied to adjust the particle size. For a particle diameter of ~30 nm, the molar ratio of the sodium citrate and the chloroauric acid is 1:1. The solution became pink right after the addition of the sodium salts and finally became wine red. The refluxing lasted for one hour and the solution was cooled down to room temperature. The surfaces of the AuNPs contain carboxylate ions, which make the AuNP-suspensions negatively charged and thus stabilize the AuNPs. The carboxylate ions hydrolyze at pH = 4,[93] leading to aggregation of AuNPs below that pH.

AuNPs with a diameter of ~30 nm were made because this is similar to the size of the conductive domains inside some conjugated polymer blends,[4,94] as well as in mine. To measure the size distribution of the AuNPs, I used tapping mode AFM (Dimension D3100 cl, Veeco Instrument Inc., Santa Barbara, USA) with 70 kHz (resonance frequency) silicon cantilevers (**Figure A4a**, OMLAC240 TN, Olympus, Japan). I determine the the relative height Δh of the particles' apices with respect to the flat silicon substrate. The average diameter of the AuNPs is $\bar{d}$ = 29.9 ± 6.1 nm, as determined from 65 AuNPs (**Figure 2.1**). The measured $\bar{d}$ of the

AuNPs is very close to the expected value (~25 nm).

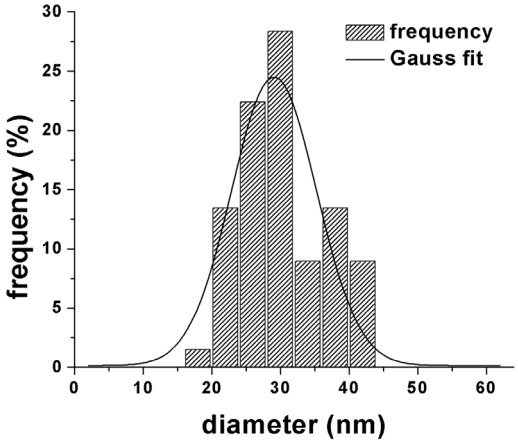

Figure 2.1. Size distribution of AuNPs.

2.1.2 PPy:PSS

Pyrrole can be oxidized by Fe^{3+} and conductive PPy (cation) is formed.[5] To prevent PPy from aggregation, PSS (anion) is used.[24,25] However, the addition of Fe^{3+} causes a collapse of PSS, which is a typical polyelectrolyte effect.[95] The collapse of PSS results in domains that are not accessible to PPy, leading to the formation of large colloidal gels in suspension. Spin coating such suspension on a substrate produces a film with large roughness. To reduce the film roughness, Fenton's reagent was used for oxidizing pyrrole (**Scheme 2.1**). Since only a catalytic amount of Fe^{3+} is added, PSS does not collapse upon addition of the oxidant (Fe^{2+}/H_2O_2). Polystyrene sulfonic acid (PSSH, $M_w \approx 7123$ g mol^{-1}), $FeSO_4 \cdot 4H2O$, pyrrole and H_2O_2 (35 wt% in water) were bought from Aldrich. Pyrrole was distilled under reduced pressure before the reaction, while the other chemicals were used as received. The PPy:PSS blend was prepared by drop-wise addition of H_2O_2 to the aqueous solution of pyrrole, PSSH and $FeSO_4$. The reaction lasted for 24 hours. Afterwards, the product was purified by several cycles of ultrafiltration with Milli-Q water.

$$Fe^{2+}(aq) + H_2O_2 + 2\ H^+(aq) \rightarrow 2\ Fe^{3+}(aq) + 2H_2O(l)$$

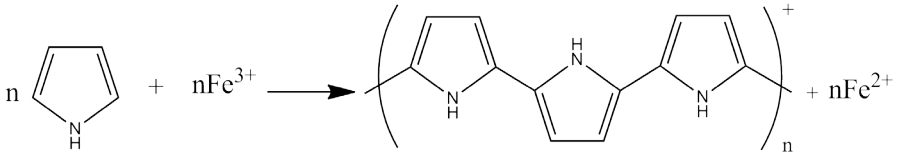

Scheme 2.1. Reaction Procedure of PPy oxidized by Fenton's reagent.

The weight ratio of PPy to PSSH in the prepared PPy:PSS blend is 1:2.7, as calculated from results of elemental analysis measured in Ciba Inc. (now part of BASF). The hydrodynamic radius of PPy:PSS is ~13 nm, as measured by dynamic light scattering (ALV Goniometer-System, ALV 5000 and ALV 7002 Muliple Tau Digital Correlator, He-Ne Laser, **Figure A1**). The conductivity of PPy:PSS is 2×10^{-2} S cm^{-1}, as measured by dielectric spectroscopy (**Figure A2**). The route mean square (RMS) roughness of PPy:PSS thick films (~80 nm) was ~1 nm, as measured by tapping mode AFM. The work function of PPy:PSS is 4.96 ± 0.03 eV, as measured by KPFM (**Figure A6**).

2.1.3 Ag core-shell particles

Ag-plated melamine resin particles (2 μm, **Figure 2.2a**) were bought from Microparticles GmbH (Berlin, Germany). I diluted the Ag core-shell particles in MilliQ water with a volume ratio of 1:1000. To determine the thickness of the Ag layer of the core-shell particle I first etched the particle by focused ion beam (FIB, FEI Nova 600 Nanolab, FEI Company, Eindhoven, The Netherlands). I selected the auto milling program for Au^{96} and chose the etching depth of 600 nm. The current of the ion beam was set to 10 pA and the voltage to 30 kV. Since the ion beam has stronger influence on polymers, the polymer core was completely removed during etching the Ag shell. The thickness of the Ag layer is 100 - 200 nm as I measured by SEM (**Figure 2.2b**). This value will be used to calculate the conductivity of the Ag core-shell particles.

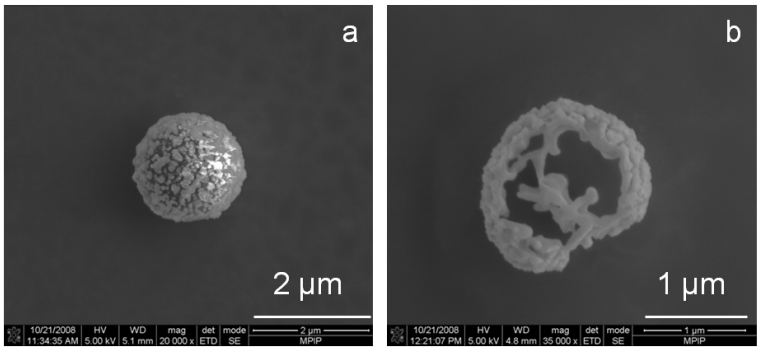

Figure 2.2. SEM images of Ag core-shell particles before (a) and after (b) FIB etching.

2.1.4 Au bulk particles

The Au bulk particles (1.5 – 3.0 µm, **Figure 2.3a**) were bought from Johnson Matthey GmbH (Karlsruhe, Germany). I suspended the Au particles in MilliQ water with a volume ratio of 1:1000. The actual size of individual Au particle was determined by SEM (**Figure 2.3a**). I also etched some Au bulk particles by FIB using the auto milling program for Au (**Figure 2.3b**).[96] The etching depth was set to 800 nm. The SEM image after the FIB etching proves that the particles entirely consist of gold.

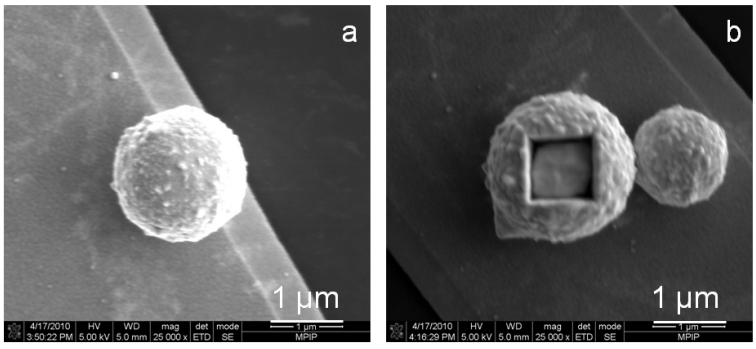

Figure 2.3. SEM images of Au bulk particles before (a) and after (b) FIB etching.

2.2 Sample preparations

2.2.1 Individual AuNPs and Au clusters

The aqueous suspension of the AuNPs is sensitive to pH and impurities. PS is dissolved in toluene. Mixing the PS solution and the AuNP suspension could result in Au aggregates randomly distributed in the mixture. To control the distribution of the AuNPs in the PS matrix, I deposited the AuNPs and PS in two steps (**Scheme 2.2**). In the first step, I deposited the AuNPs on a silicon substrate with two arrangements. In the second step, I deposited the PS film on top of the AuNPs.

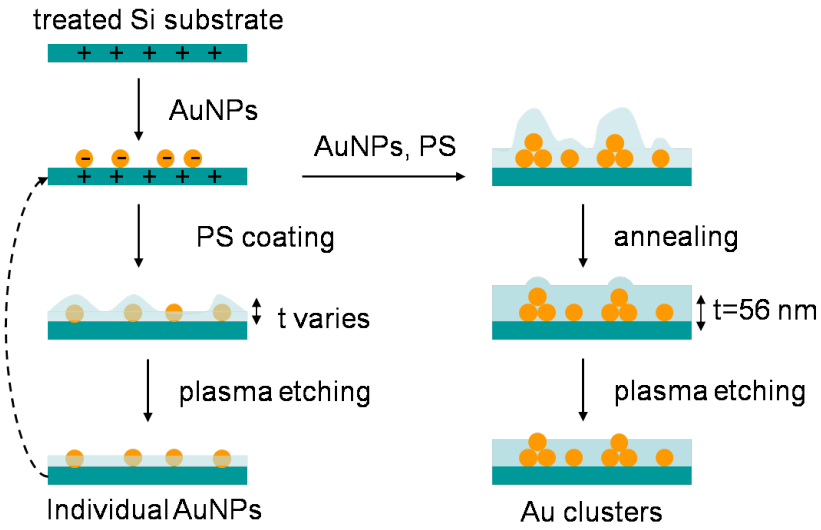

Scheme 2.2. A schematic sketch of how to control the nanoscopic morphology of the Au/PS system.

Functionalization of the silicon substrate: I used highly doped silicon wafers (Boron doped, (100), resistivity 1 – 20 Ω cm, Crys Tec GmbH, Berlin, Germany) as substrates. The purchased silicon wafers were pre-cleaned and protected by an adhesive foil. I removed the transparent foil on the polished side by rinsing the silicon wafer in ethanol,[97] and further cleaned the wafer with plasma (90% argon and 10% oxygen at 300 W, 200-G Plasma System, Technics Plasma GmbH, München, Germany) for 10 min. Right after the plasma cleaning, I immersed the silicon substrate in a methanol solution of 1% N-trimethoxysilylpropyl-N,N,N-trimethylammonium chloride (NR_4^+, 50% in methanol, ABCR ABCR/Gelest, Karlsruhe, Germany) for 30 min, washed it with

Milli-Q water (resistance was 10.2 MΩ), and baked it at 95°C for 1 h (Thermolyne Furnace Model 47900, Thermo Fisher Scientific Inc., Waltham, USA). By this procedure a monolayer of positive NH_4^+ groups was bounded to the substrate.[98] If not specified, otherwise I treated all the silicon substrates I used in this thesis the same way.

Deposition of AuNPs: The negative AuNPs can be electrostatically attracted by the NH_4^+ groups on the functionalized silicon surface. I therefore immersed the silicon substrate in the aqueous colloidal gold suspension for 30 min. By this procedure I deposited "individual AuNPs" on the substrates (**Scheme 2.2**). I re-immersed the sample in the suspension for another 10 min. I changed pH of the suspension from 6.7 to 4.0, causing aggregation of AuNPs. By this procedure I deposited both individual AuNPs and small aggregates of AuNPs on the substrate. I call this type of samples as "Au clusters".

t (nm)	PS concentration (mg / ml)	Spin-coating speed (rpm)
25	5	1500
40	10	2000
56 (annealed)	10	1200
70	11	1000
133	12	1000

Table 2.1. Detailed parameters for preparing PS films of different thicknesses.

Deposition of PS film: I spin-coated PS (M_n = 11200, M_w/M_n = 1.06, Polymer Standards Service, Mainz, Germany) onto samples with individual AuNPs or Au clusters. By changing the concentration of the PS solution and the spin-coating speed, I varied the thickness *t* of the PS film on the substrate from 25 nm to 133 nm (**Table 2.1**). The detailed description of measurements of film thickness is introduced in **Appendix A.2**. To further tune *t* I etched the PS layer by Ar plasma (50% Argon, 60 W) and controlled the etching depth by controlling the plasma

etching time. After each plasma etching step I re-measured *t*.

2.2.2 HOPG substrate and HOPG sample

I first painted four sides of HOPG (resistivity 4 x 10^{-5} Ω cm, SPI-3 grade, SPI supplies, West Chester, USA) with silver paste (Acheson Silver DAG 1415, Plano GmbH, Wetzlar, Germany). By this procedure I was able to ground the top layer of HOPG. I then used a "Scotch" tape to remove a few graphite layers right before coating polymer films or directly characterizing the bare graphite surface. The clean HOPG was inserted into the environmental chamber of the AFM apparatus (Agilent Technologies, Inc., Santa Clara, USA) directly. The total time that a clean HOPG surface remained exposed to lab air (relative humidity ≈ 20%) was always less than 5 min.

2.2.3 Thick PPy:PSS films

The aqueous PPy:PSS solution (4 wt % in water) was spin-coated onto freshly cleaved HOPG, with a spin-coating speed of 3000 rpm. The film thickness of PPy:PSS is ~60 nm. The unannealed sample was immediately put into the environmental chamber of the AFM apparatus, with controlled atmosphere and characterized by KPFM. I used unannealed and annealed samples. I annealed them in air at 180 °C for 10 min right after spin-coating. The annealing parameters are typically used for conducting polymers used for preparing OLEDs.[24,25] After annealing, the samples were inserted in the environmental chamber for the measurements. The total time that PPy:PSS was exposed to lab air (relative humidity ≈ 40%) after annealing was always less than 5 min.

2.2.4 Thin PPy:PSS films

The aqueous PPy:PSS solution (4 wt % in water) was drop-coated onto freshly cleaved HOPG. The excess PPy:PSS was blown off by a nitrogen gun after a few seconds. The unannealed sample was immediately put into the environmental chamber, with controlled atmosphere and characterized by KPFM. I also used

annealed samples at 180 °C for 10 min in a nitrogen-filled Glovebox (O_2 < 10 ppm, RH < 5%, GB2202-C S1/mol, Mecaplex, Switzerland) right after drop-coating. After annealing, the samples were inserted in the environmental chamber and measurements performed. The total time that unannealed and annealed PPy:PSS films remained exposed to lab air (relative humidity ≈ 40%) was less than 5 min.

2.2.5 Thin PSSH films

I used the same PSSH (PSSH, 7 500 g/mol, 18 wt % in water) that was used to synthesize PPy:PSS for reference measurements. The dielectric constant of PSSH is $\varepsilon \approx 9$, as measured by dielectric spectroscopy.[99] I diluted PSSH to 0.6 wt % prior to sample deposition. Handling and experiments with samples of PSSH thin films were similar as with samples of PPy:PSS thin films. The total time that PSSH was exposed to air (relative humidity ≈ 20%) was less than 5 min.

2.2.6 Design of electrode array

Figure 2.4a is a schematic sketch of a silicon chip used to measure conductivity of single particles. There are 16 pyramidal pits on each silicon chip. The dimension of the pit is 3 x 3 μm^2 and the distance between two neighboring pits is 50 μm (**Figure 2.4b**). This dimension is designed for particles with a diameter of 1 – 3 μm. A layer of 200 nm SiO_2 on the silicon chip is used to insulate the entire chip. The thermally deposited microelectrodes (10 nm Ti and 200 nm Au) were electrically wired to a socket, which leads to the source meter (**Figure 2.4c**). The individually bonded chips were fabricated by IMM (IMM GmbH, Mainz, Germany) with two geometries of the electrode arrays (**Figure 2.5**), following the design from Max Planck institute for polymer research.

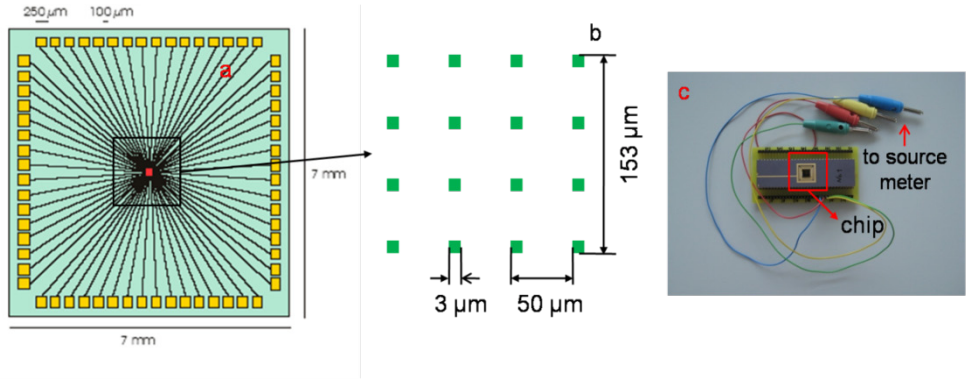

Figure 2.4. Schematic sketches of a silicon chip (a) and the center area of it (b); c) a photo of a wired chip ready for micro four-point probe measurements.

In **Figure 2.5a**, each pyramidal pit is coated with a layer of Ti-Au and connected to the surrounding four microelectrodes. This electrode array is used to contact the particle at the bottom. I therefore call this geometry as "bottom contact". In **Figure 2.5b**, the pyramidal pits are not coated by Ti-Au. The four microelectrodes are 3 µm away from the edge of the pyramidal pit they surround. This electrode array is used to contact the particle on the top. I therefore call this geometry as "top contact".

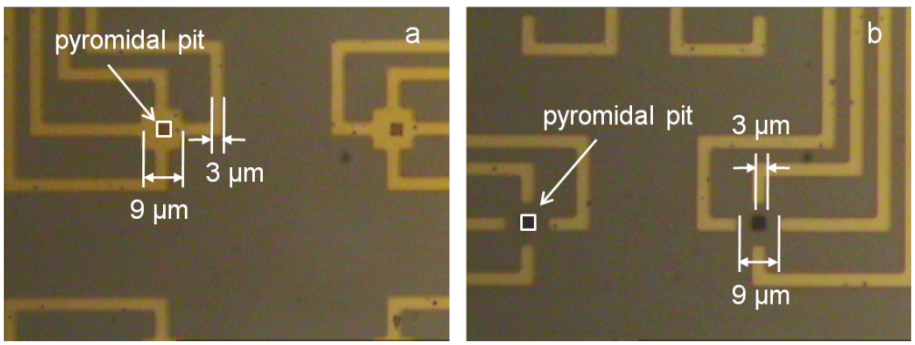

Figure 2.5. Optical microscopy images of two geometries of the electrode array: a) bottom contact; b) top contact. The magnification is 50 x.

2.2.7 Two geometries of electrode array

Bottom contact: I separated the four microelectrodes by FIB (auto milling program for Au, **Figure 2.6a**). The current of the ion beam for the milling was set to 10 pA and the voltage to 30kV. I first etched the electrodes outside the pyramidal

pit with a dimension of 400 x 400 nm^2 (width x depth). Then I separated the electrodes inside the pyramidal pit with a dimension of 0.23 x 4.5 μm^2 (width x length) by a series of etching with decreasing depth, i.e. 400 nm, 100 nm, and 50 nm. The separation distance of the electrodes inside the pyramidal pit is small (~0.23 μm). The extra ions sputtered on the milling surface during FIB etching could result in short curt between these electrodes.[96] The etching procedure I used could reduce the amount of ions sputtered on the surface. The resistance between the two electrodes (connected to the same pit) was 40 – 60 Ω before the FIB etching and > 999 MΩ after the FIB etching, as measured by a multimeter (Fluke 77 Multimeter, Kassel, Germany). The increased resistance indicates that the Ti-Au electrodes were completely separated by the FIB etching. After the electrodes had been separated, I firstly drop coated particle suspension on them. Then I moved one particle inside each pyramidal pit by using a tipless silicon nitride cantilever (NP-O, Vecco Instrument Inc., Santa Barbara, USA) controlled by a hydraulic micromanipulator (MMO-203, Narishige co., Ltd., Tokyo, Japan). The four contacts were established between the single particle and the four walls (Ti-Au coated) of the pyramidal pit (**Figure 2.6b**).

Top contact: I first put the particle inside the uncoated pyramidal pit (**Figure 2.6c**) by the tipless cantilever (NP-O). Then I deposited Pt electrodes (with ~50% carbon[100]) by FIB to connect each particle to the four pre-evaporated Ti-Au electrodes (**Figure 2.6d**). The thickness of the Pt electrode is 200 nm. The dimension of each deposited Pt electrode is 4.8 x 0.4 μm^2 (length x width) for Ag core-shell particles, and 0.8 x 0.4 μm^2 (length x width) for Au bulk particles. The current of the ion beam for Pt deposition should be 2 – 3 times as big as the deposited area.[100] For connecting the Ag core-shell particles, the current was set to 10 pA, and for connecting the Au bulk particles, the current was set to 1 pA. I carefully controlled the position of each Pt electrode to achieve four similar contact areas of 400 x 400 nm^2.

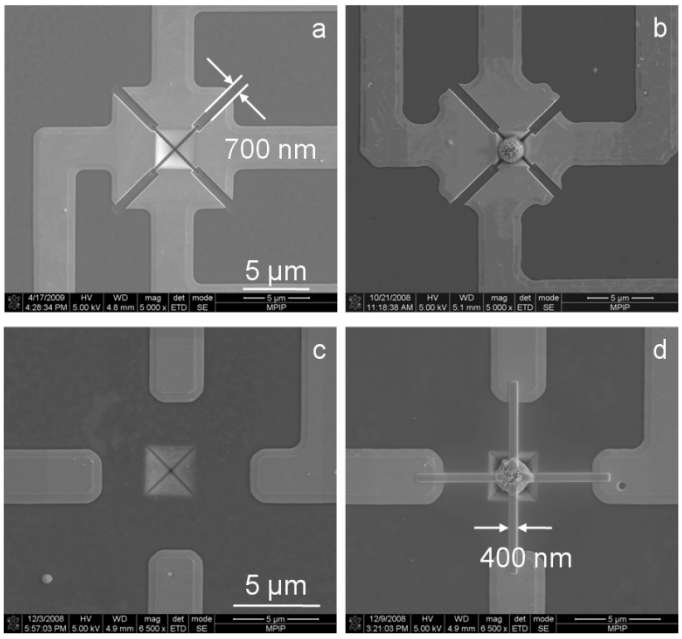

Figure 2.6. SEM images of electrode array: a) bottom contact after FIB etching; b) four electrodes are in bottom contact with an Ag core-shell particle; c) top contact before FIB deposition; d) four Ti-Au electrodes are connected to an Ag core-shell particle by Pt electrodes deposited by FIB.

2.2.8 Pt electrodes for contact resistance test

I deposited some Pt electrodes on top of the two Ti-Au electrodes by FIB (**Figure 2.7**) to check the contact resistance between them. The dimension of the Pt electrodes was controlled to be 2.1 x 0.7 x 0.2 μm^3 (length x width x height). The current of the ion beam for the deposition was set to 1 pA.

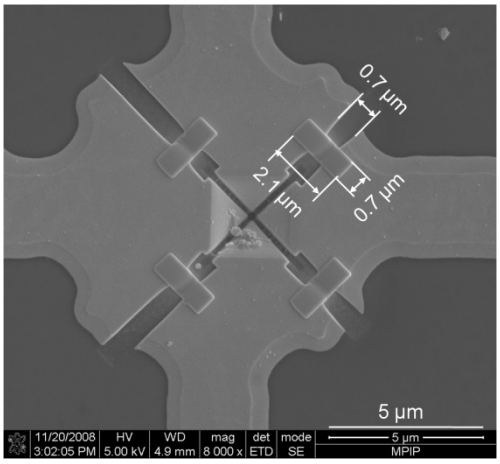

Figure 2.7. A SEM image of Pt electrodes connecting each two Ti-Au electrodes.

Chapter 3 Nanoelectronic Properties of a Model System

3.1 Introduction

In this chapter I introduce a combined KPFM and SCTMM study on a model system with controlled nanoscale morphology and known electronic properties. I used the gold/polystyrene system with conductive gold nanoparticles (AuNPs) embedded into a non-conductive PS film as a model. The AuNPs represent the conductive domains and the PS the non-conductive polymer matrix. I controlled the nanoscale morphology of the model system by varying two parameters: (i) the distribution of the AuNPs inside the PS film (from individual particles to clusters); (ii) the thickness of the PS layer around and on top of the AuNPs. Later I apply the knowledge from the model system to interpret KPFM and SCTMM data of a conjugated polymer blend: PPy:PSS.

3.2 Experimental

3.2.1 Phase measurement

The phase signal detected by the "two-pass" mode KPFM could be influenced by the electric field between the tip and the sample.[85] I therefore used tapping mode AFM (Dimension D3100cl) with 70 kHz (resonance frequency) silicon cantilevers (OMLAC240 TN, **Figure A4a**), and obtained height and phase images simultaneously. The amplitude set-point was set to ~0.9 V and the scan rate to 1.5 Hz for all the phase measurements. I post-treated all the height and phase images by the 3rd order of "flattening" with NanoScope v7.20. Afterwards, I measured the relative height Δh and the relative phase $\Delta\varphi$ of the AuNPs with respect to the PS film or silicon substrate by "cross-section" analysis. To control that the cantilevers

were not damaged during the AFM measurements, all cantilevers were imaged by SEM (1530 Gemini, Carl Zeiss SMT, Oberkochen, Germany) by Maren Müller after usage (**Figure A5a**).

3.2.2 KPFM measurement

I performed "two-pass" mode KPFM measurements in air on a Multimode TR-TUNA® (Veeco Instrument, Santa Barbara, USA) with a IIIa controller, with 70 kHz (resonance frequency) Pt-Ir coated cantilevers (PPP-EFM NanosensorsTM, Neuchatel, Switzerland). The tip radius is <25 nm, as proved by SEM images of new tips (**Figure A4b**). The lift scan height was set to 5 nm and the AC drive voltage to 5 V for all KPFM measurements. The amplitude set-point was set to ~0.9 V and the scan rate to 1 Hz. I lifted the cantilever only after a stable height image had been obtained. Before recording the surface potential image, I tuned the "drive phase" to nullify the "potential input" signal to eliminate cross-talk between topography and surface potential.[85]

The surface potential measured in KPFM is a relative value that depends on the work function of the tip, as discussed in **Chapter 1**. In this chapter I only discuss the relative surface potential difference ΔV between the AuNPs and the surrounding PS film or the bare silicon substrate. Hence for the study in this chapter, I can exclude the influence of the particular tip work function. The calibration of the tip work function is thus not necessary. To avoid any damage to the tip, I did not calibrate the work function of the tip used in all KPFM experiments described in this chapter. Nevertheless I measured the work function of the Pt-Ir coated cantilevers by KPFM on freshly cleaved HOPG (Φ = 4.65 eV in air[101]) for routine characterizations of the cantilevers. The work function of the Pt-Ir cantilevers is 4.95 ± 0.05 eV (**Figure A6a** and **Figure A6b**). To control that the cantilevers were not damaged during the KPFM measurements, they were imaged by SEM (1530 Gemini, Carl Zeiss SMT) after usage (**Figure A5b**). Since the electron beam of SEM could damage the metal layer of the conductive tips, SEM characterization was performed only after the measurements.

All the KPFM images showed in this chapter were recorded in "retrace" channels. However I always recorded potential images in both "trace" and "retrace" channels. I can exclude the tip artifacts if images recorded in the two channels are similar. I post-treated all height images taken by KPFM by 3rd order "flattening" and surface potential images by 1st order "plane fit" with the NanoScope software v7.20. Afterwards, I measured Δh and ΔV of the AuNPs by "cross-section" analysis.

3.2.3 SCTMM measurement

The measured tunneling current is influenced by the conductivity of the tip. I therefore did *I-V* curve measurements by contact mode c-AFM on freshly cleaved HOPG to check the conductivity of the tips before each SCTMM measurement (**Figure A5b**). During the *I-V* curve measurement I controlled the deflection set-point to make sure that the minimum force was applied to the sample surface. The whole AFM apparatus was wrapped in aluminum foil acting as a Faraday cage to avoid electronic noise during the SCTMM measurements. The sensitivity of the current preamplifier was set to 1 pA V^{-1} in all measurements if not specified otherwise. The torsional amplitude set-point was set to ~0.2 V and the scan rate to 0.8 Hz.

The conductive layer of the tip could be damaged due to a sudden increase of the electric field between the tip and the sample. Therefore I only applied the bias voltage to the sample once the cantilever approached the sample surface. After a stable height image was obtained, I slowly increased the bias voltage with a step of 0.2 V. Once the current signal became measurable, I increased the applied bias voltage by 0.5 – 1.0 V. By this procedure the voltage was tuned to sense all the conductive domains but not to cause any electric breakdown between tip and sample.

All the SCTMM images shown in this chapter were recorded in "retrace" channels. I also always recorded current images in both "trace" and "retrace" channels to exclude any tip artifacts. Same as KPFM measurement, all cantilevers

used in the SCTMM measurements were imaged by SEM only after they had been used. I post-treated all height images taken by SCTMM by 3rd order "flattening" with the NanoScope software v7.20. The current images display absolute values. I measured Δh and current of the AuNPs by "cross-section" analysis.

3.3 KPFM and SCTMM studies on Au/PS model system

Here I look for the correlation between the nanoscopic morphology of the Au/PS system and its electronic properties. I therefore discuss the role played by the distribution of the AuNPs inside the PS matrix on both surface potential and current.

3.3.1 Phase analysis of individual AuNPs

The thickness of the PS film on top of the AuNP or the embedding depth of the AuNP, Δt influences the measured surface potential and current. Therefore I first analyze Δt. Naked AuNPs and PS films should exhibit a strong phase contrast due to their different elastic modulus ($E_{Au} \approx 79$ GPa and $E_{PS} \approx 3$ GPa[102]). If Δt is very thin, the tip could still sense the AuNP underneath. The measured $\Delta\varphi$ is dominated by E_{Au}. With increasing Δt, the influence of Au to the measured $\Delta\varphi$ decreases, while the influence of PS increases. By analyzing phase images of individual AuNPs embedded in PS films of different t: $t = 25$ nm and $t = 46$ nm, I could obtain information of Δt.

For $t = 25$ nm, t is smaller than the average particle diameter $\bar{d}$; while for $t = 46$ nm, $t > \bar{d}$. The phase images of the AuNPs are different when they are embedded in PS films of different t (**Figure 3.1**). $\Delta\varphi$ of the AuNPs embedded in a thinner PS layer ($t = 25$ nm) is almost constant and is ~70° (**Figure 3.1a** and **Figure 3.1b**). $\Delta\varphi$ of the AuNPs imbedded in a thicker PS layer ($t = 46$ nm) is smaller (5° – 40°) and exhibits a dependence on Δh (**Figure 3.1c** and **Figure 3.1d**).

For the sample of $t = 25$ nm, the big phase contrast (~70°) between the PS covered AuNPs and the PS film indicates that the measured $\Delta\varphi$ was dominated by

E_{Au}. For the sample of t = 46 nm, the small phase contrast (5° – 40°) between the PS covered AuNPs and the PS film indicates that the measured $\Delta\varphi$ was dominated by E_{PS}. Hence Δt is thinner for smaller t and thicker for bigger t. The dependence of $\Delta\varphi$ on Δh for the thicker PS film indicates that Δt also depends on the diameter d of the AuNPs.

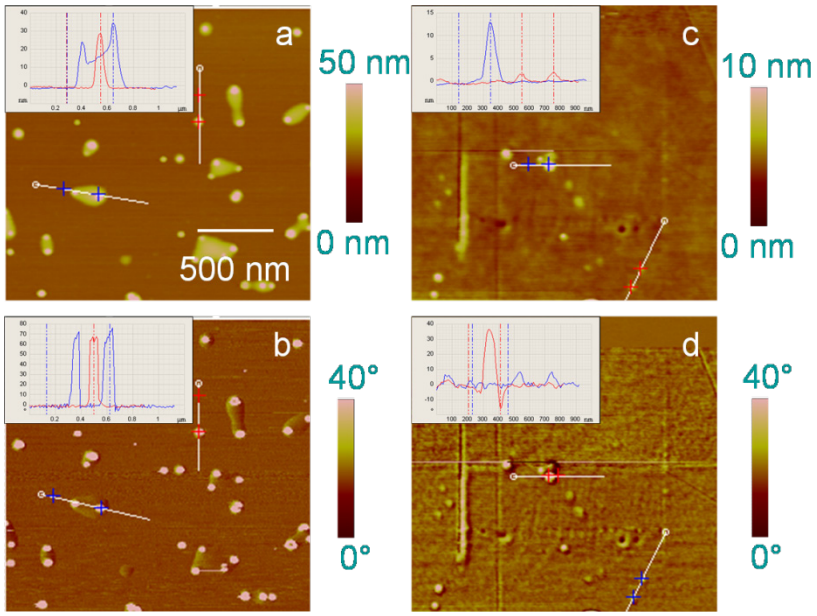

Figure 3.1. Height (a and c) and phase (b and d) images of AuNPs embedded in PS films of different t: a) and b) t = 25 nm; c) and d) t = 46 nm; inset, surface profile analysis along the white lines. The colored crosses on the height and the phase images correspond to the curves of the same color on the surface profile.

To quantitatively relate Δt to d and t, I plotted $\Delta\varphi$ versus Δh (**Figure 3.2a**) at different t. For t = 25 nm, $\Delta\varphi$ remains unchanged within the limits of the experimental error. For t = 46 nm. $\Delta\varphi$ nearly linearly increases with Δh. Apparently in this system, spin-coating does not yield films of equal thickness on the particles (Δt) and on the flat surface (t). Instead Δt is related to $\bar{d}$ (**Figure 3.2b**). If $t < \bar{d}$, the PS film that covers the AuNPs is small and of similar thickness. If $t > \bar{d}$, the PS film that covers the AuNPs decreases linearly with increasing d. Thus, AFM phase images in combination with height images help me to qualitatively estimate the thickness of soft thin polymer films on top of hard nanoparticles. I will use this

information for interpreting the KPFM results.

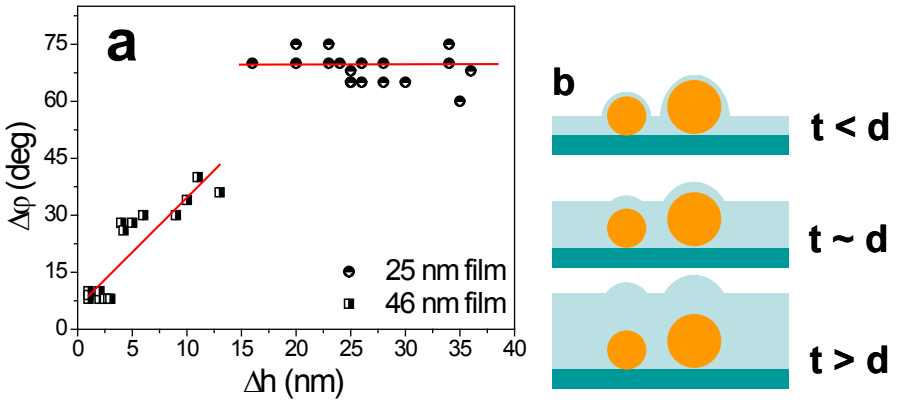

Figure 3.2. a) A plot of $\Delta\varphi$ versus Δh for AuNPs embedded in PS films of t = 25 nm and t = 46 nm. The red lines serve as a guide for the eye. b) Cartoon of the growth of the film on top of particles of different sizes.

3.3.2 KPFM analysis of individual AuNPs

Figure 3.3 shows height and surface potential images upon different t, i.e. t = 0, 25, 40, 70 and 130 nm. On the height images, I find some particles and a flat surface. The particles represent the AuNPs and the flat surface represents silicon substrate or PS film. With increasing t, the AuNPs become less visible on the height images. They almost disappear on the height image of t = 130 nm (**Figure 3.3i**). On the surface potential images, the AuNPs show lower surface potential compared to the PS film or the silicon substrate. With increasing t, the relative surface potential difference ΔV of the individual AuNPs with respect to the PS film decreases from ~100 mV (t = 0 nm) to ~30 mV (t =130 nm). For all samples, the particles that exhibit maximum ΔV are also the ones that exhibit maximum Δh within one image.

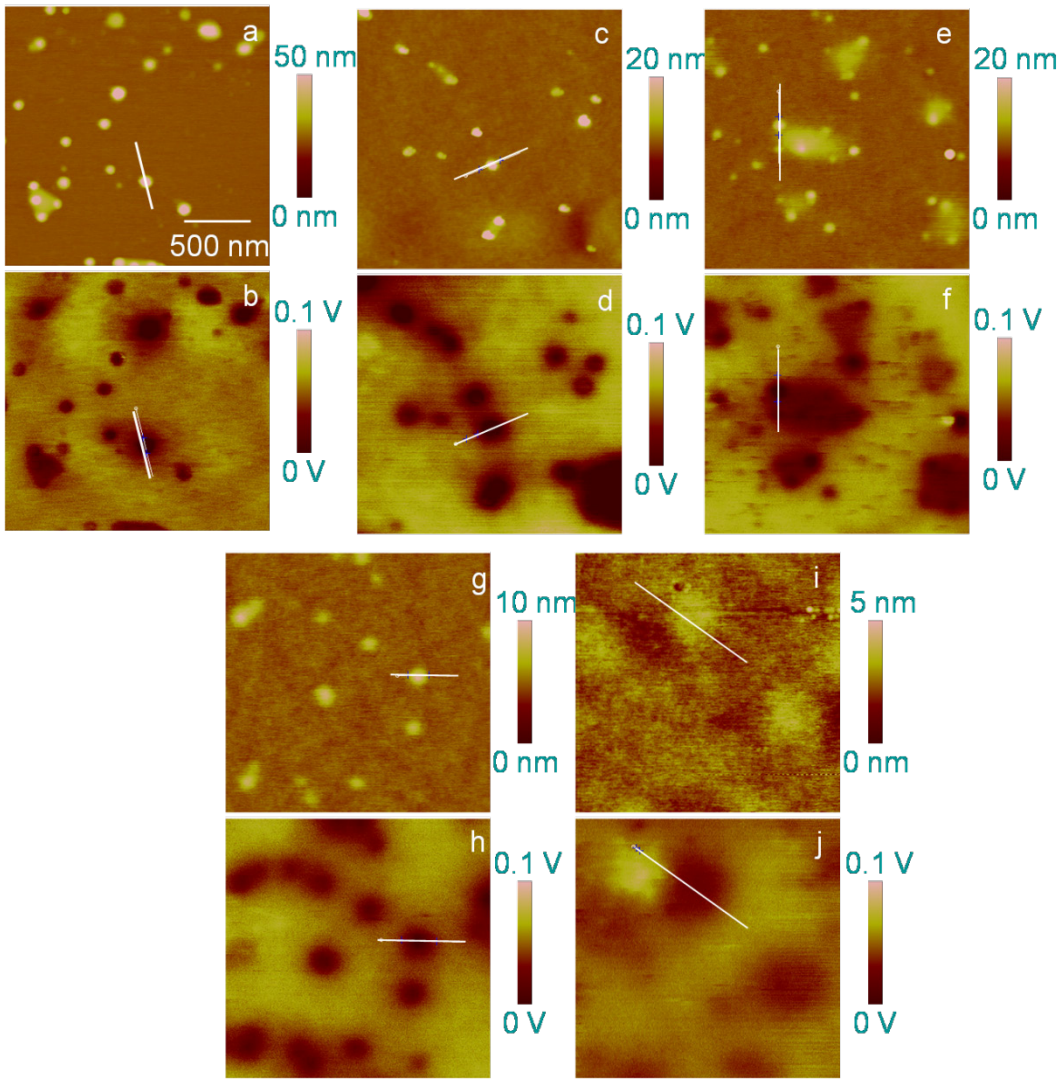

Figure 3.3. Height (a, c, e, g, and i) and surface potential (b, d, f, h, and j) images of individual AuNPs embedded in PS films of different *t*: a) and b) on the bare silicon wafer; c) and d) *t* = 25 nm; e) and f) *t* = 40 nm; g) and h) *t* = 70 nm; i) and k) *t* = 130 nm.

Δ*t* increases upon *t*, leading to less visibility of the AuNPs, as expected. When *t* approached 130 nm, the AuNPs were almost completely covered by the PS film. According to **Equation 1.9** the lower surface potential corresponds to higher work function. The work function of Au is between 5.1 and 5.47 eV,[102,103] and the work function of p-doped silicon (100) is 4.91 eV.[102] Hence the measured Δ*V* of ~100 mV between the AuNPs and the silicon substrate is consistent with results from literature. Although I used a new cantilever for each experiment, Δ*V* would not be

influenced by the small work function variation of different cantilevers, as discussed. Moreover, I also always used a constant "lift scan height" of 5 nm. Therefore changes of ΔV are due to the decreased contribution of the AuNPs with increasing Δt. Nevertheless, KPFM is till sensitive enough to track the AuNPs that are not visible on the height image (**Figure 3.3i** and **Figure 3.3j**). Hence KPFM is able to measure the surface potential of conductive domains that are covered by some protecting layer with a different electronic work function up to a considerable thickness.

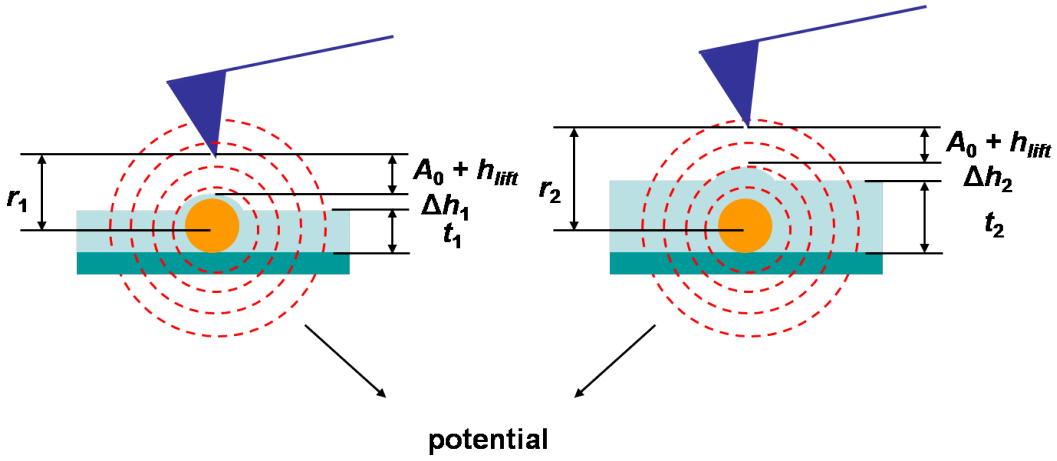

Figure 3.4. Schematic sketches of potential generated by an AuNP imbedded in a thin (left) and a thick (right) PS film.

To explain the influence of t on ΔV, I consider the AuNP as a sphere with charge Q (**Figure 3.4**). The potential V generated at a distance r is described as[104]

$$V(r) = \left(\frac{Q}{4\pi\varepsilon_0\varepsilon_r} \right) \frac{1}{r}. \tag{3.1}$$

Here ε_0 is the vacuum permittivity and ε_r is the relative permittivity of the medium. The distance r is

$$r = t - \frac{1}{2}\bar{d} + h_{lift} + A_0 + \Delta h. \tag{3.2}$$

Here h_{lift} is the lift scan height, which was 5 nm, and A_0 is the half oscillation amplitude of the cantilever in "lift mode", which was 20 nm. I consider $\bar{d} \approx 30$ nm for a rough calculation. Hence **Equation 3.2** can be written as

$$r = \Delta h + t + C\,, \tag{3.3}$$

where $C \approx 10$ nm.

According to **Equation 3.1**, V is influenced by both r and ε_r. As described in **Equation 3.3**, r increases with t. The surface potential of silicon or PS is constant. Hence ΔV decreases with increasing t. The projection of the surface potential on the sample surface also becomes larger with increasing r. Hence the surface potential profile is broader for the AuNPs with a thicker PS film on top. During the KPFM measurement, there were two dielectrics between the AuNP and the conductive tip, i.e. a PS film of different t and air. The dielectric constants of PS and air thus also influenced V. V would show a stronger dependence on $1 / r$, if air ($\varepsilon_{r,air} = 1$) was the predominant dielectric; and V would show a weaker dependence on $1 / r$, if PS ($\varepsilon_{r,PS} = 2.5$) was the predominant dielectric.

To quantitatively analyze the dependence of ΔV on r and ε_r, I plotted ΔV versus $1 / r$ (**Figure 3.5**). For each t, I measured and averaged ΔV and Δh of 5 – 10 particles. I used the average Δh for each t to calculate r according to **Equation 3.3**. There are two linear parts in the graph, one is from $t = 0$ to $t = 40$ nm, and the other from $t = 40$ to $t = 130$ nm. The kink at $t = 40$ nm corresponds roughly to the average diameter of the AuNPs. The ratio of the two slopes is roughly 2.87.

Each linear part indicates influences of the sample geometry on ΔV. The different slopes of the two lines indicate influences of dielectric properties of PS and air. If $t < \bar{d}$, air was the predominant dielectric while the PS film covering the particles was only a few nanometers thin, as proved by the phase analysis. Thus the slope of the line is mainly related to the dielectric constant of air. If $t > \bar{d}$, the PS film on top of the particle was thicker and its contribution dominated over that of air. The slope of the line is then mainly related to the dielectric constant of PS. The ratio of the two slopes is very close to that of $\varepsilon_{r,PS}$ and $\varepsilon_{r,air}$, which further proves that the measured surface potential is also influenced by the dielectric properties of samples.

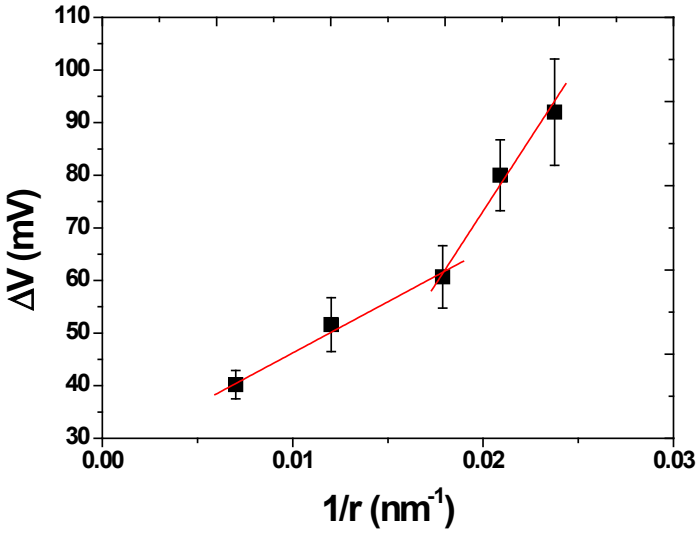

Figure 3.5. A plot of ΔV versus r.

I took the surface potential images in "lift mode", by which the cross-talk of the surface potential with topography is minimized.[83] To verify that this rule held for my measurements, I compare the height and surface potential images of individual AuNPs embedded in the PS film of t = 130 nm before and after annealing (**Figure 3.6**). t was almost constant before and after annealing, as measured by tapping mode AFM. The peak-to-valley value of the topography decreased from 7 nm before annealing to 5 nm after annealing. On the height image taken after annealing the AuNPs are almost not visible (**Figure 3.6c**). However ΔV of the AuNPs remains ~30 mV on the surface potential image taken after annealing (**Figure 3.6d**). The fading of some formerly clear particle topologies indicates that the PS film relaxed and flattened upon annealing. Nevertheless the slightly changed topography did not cause pronounced change in the measured surface potential. Hence there was no cross-talk between the surface potential and the topography.

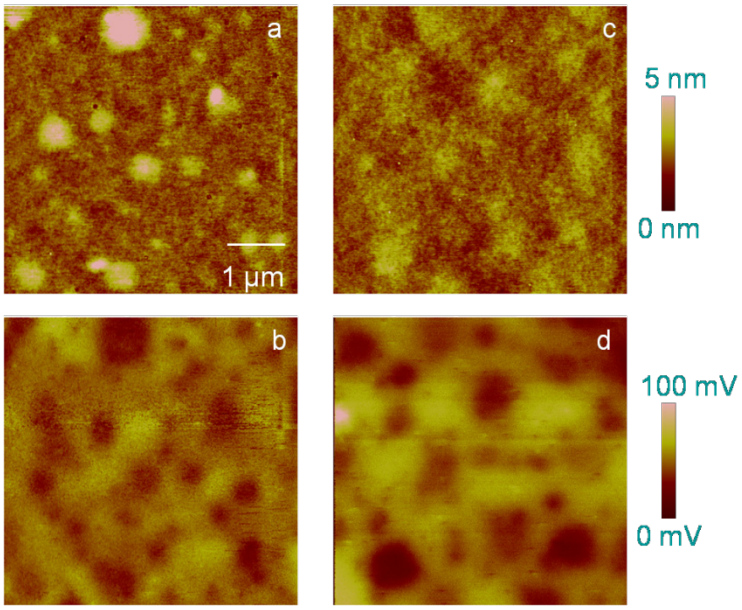

Figure 3.6. Height (a and c) and surface potential (b and d) images of individual AuNPs embedded in a PS film of t = 130 nm: a) and b) before annealing; c) and d) after annealing at 100 °C for 5 min.

The surface potential measured by KPFM is influenced by both, the embedding depth of the AuNPs and the dielectric properties of the non-conductive PS matrix. Conductive domains, like AuNPs, can be detected by KPFM even when they are embedded in non-conductive matrix, like PS. For particles with a $\bar{d} \approx 30$ nm this depth is up to 100 nm. The lateral resolution of KPFM is not as high as its vertical resolution due to the broadening effect discussed above. Already on a bare silicon surface the surface potential of a 30 nm AuNP is ~100 nm broad, and it broadens to ~300 nm when t = 130 nm. Apparently with KPFM only I cannot study the distribution of the percolation channels formed by the AuNPs in the non-conductive PS matrix, or the conductivity variations of the channels. I need a complementary method, i.e. c-AFM or SCTMM.

3.3.3 SCTMM analysis of individual AuNPs

Since the AuNPs are only physically attached to the silicon substrate, they will be swept away by the conductive tip when operated in contact mode. I therefore used SCTMM to study the conductivity of the Au/PS system. The

percolation threshold in conjugated polymer blends depends on the distance between neighboring domains and on the morphology of individual domains. In the Au/PS system, the formation of percolation paths is determined by the distance between the conductive tip and individual AuNPs on the silicon substrate, i.e. Δt.

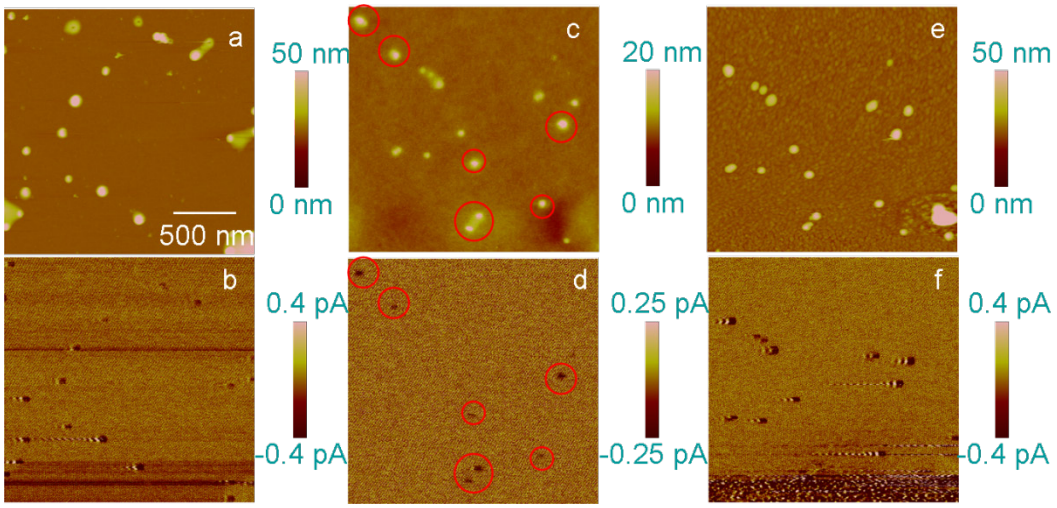

Figure 3.7. Height (a, c, and e) and current (b, d, and f) images of individual AuNPs embedded in PS films of different *t*: a) and b) on the bare silicon wafer, current bias = -9V; c) and d) *t* = 25 nm, current bias = -12 V; e) and f) same position as c) and d) after 10 min plasma etching, current bias = -8 V.

Figure 3.7 shows a representative series of height and current images of individual AuNPs. I applied always a negative bias to the sample. Therefore a more negative current corresponds to a percolation path with a higher conductivity. Each AuNP on the bare silicon surface corresponds to a current of ~6 pA with a bias voltage of -9 V (**Figure 3.7a** and **Figure 3.7b**). After coating a 25 nm thin PS film, Δh of the AuNPs reduced to 7 – 17 nm (**Figure 3.7c**). On the current image, less than half of the particles (marked by red circles) still correspond to a current (**Figure 3.7d**). These particles are the largest AuNPs. The current decreased to 0.4 ~0.8 pA despite that I increased the voltage to -12 V. After plasma etching, *t* reduced to ~12 nm and Δh increased to 17 – 25 nm (**Figure 3.7e**). All the AuNPs correspond to the current again (**Figure 3.7f**). The measured current increased to ~5 pA, which is very close to the current measured on the bare AuNPs.

The corresponding height and current images of the naked AuNPs indicate that all the AuNPs were conductive and of similar conductivity. The reduced current after the PS coating indicates that the thin PS film raises the tunneling barrier. The tunneling current is bigger on bigger particles, indicating that Δt is smaller for bigger particles. This difference was not sensed by the phase imaging (t = 25 nm). The height images of the AuNPs covered by the PS film before and after the plasma etching proves that both images were taken at the same position. The plasma etching with a depth of ~13 nm could completely remove the PS layer on top of the AuNPs, since Δt was only a few nanometers before the plasma etching. Therefore all the AuNPs became naked after the plasma etching, as proved by the current image. The small difference of the current in the two experiments is probably due to the different conductivities of the tips used and to the slightly different bias voltages.

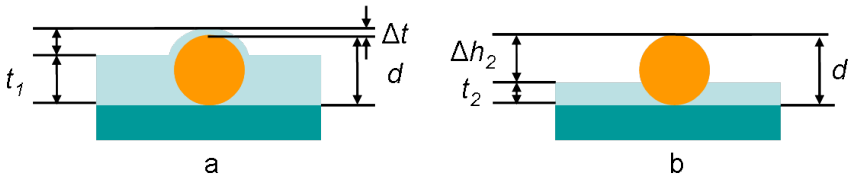

Figure 3.8. Schematic sketches of geometries of an AuNP embedded in a PS film (t = 25 nm) before (a) and after (b) the plasma etching.

Δt determines the barrier height for the electronic tunneling. I therefore evaluate Δt by comparing Δh of the same AuNP before and after the plasma etching. **Figure 3.8** represents geometries of an AuNP covered by a thin PS film before and after the plasma etching. The diameter of the AuNP can be determined as

$$d = \Delta h_1 + t_1 - \Delta t = \Delta h_2 + t_2 . \qquad (3.4)$$

Here Δh_1 and Δh_2 are the height differences between the apex of the AuNP and the PS surface before and after the plasma etching, and t_1 and t_2 are the thicknesses of the PS film on silicon surface before and after the plasma etching. By applying t_1 = 25 and t_2 = 12 into **Equation 3.4** I have

$$\Delta t = \Delta h_1 - \Delta h_2 + 13 . \quad (3.5)$$

Δh_1 and Δh_2 can be measured from **Figure 3.7c** and **Figure 3.7e**.

For t = 25 nm, Δt < 4 nm. It decreases to less than 2 nm for the 'big' particles protruding out of the PS film. These particles are the ones that already conducted current before the plasma etching, as proved by the height (**Figure 3.7c**) and current (**Figure 3.7d**) images. Apparently the non-conductive PS film, even if very thin, reduces the tunneling current measured on top of individual AuNPs. In this view the SCTMM imaging mode is superior to the KPFM mode in telling if there is yet a sub-nanometer thin dielectric film on top of a conductive sample.

The bias of 9 V is high for measurements on a conductive AuNP. There are two reasons for this. Firstly, most of the applied voltage was consumed by the semi-conductive silicon substrate, since the voltage was applied to the back side of it. The actual voltage difference between the conductive tip and the AuNP was thus much smaller. Secondly, as addressed in **Section 1.3.2**, a higher voltage is required in SCTMM than that in c-AFM.

On some current images small damping oscillations are associated to the left side of the current signal (e.g., **Figure 3.7b** and **Figure 3.7f**). The oscillation amplitude increases with the magnitude of the measured current. This damping oscillation would appear on the right side of the current signal if I recorded the current in a "trace" channel (**Figure A8**). The damping oscillations are thus artifacts introduced by the electronic interference of the instrument. The anomaly on the lower part of the current image (**Figure 3.7f**) is also an artifact caused by the deterioration of the tip. I discard the data contained there since they were acquired at the end of the scanning process (the image was acquired from the top).

If t > 40 nm no current was measured by SCTMM. Here I show one example. **Figure 3.9** shows KPFM and SCTMM results of AuNPs embedded in the PS film of t = 70 nm. On the height and the corresponding surface potential images, all the AuNPs correspond to lower surface potential (**Figure 3.9a** and **Figure 3.9b**). However when performing SCTMM on the same position, I measured only noise

(**Figure 3.9c** and **Figure 3.9d**). After 24 min. plasma etching, each AuNP corresponds to a current up to ~2.4 pA (**Figure 3.9e** and **Figure 3.9f**). The film thickness reduced to t = 15 nm and Δh of the AuNPs increased from ~3 nm (before the plasma etching) to ~25 nm (after the plasma etching).

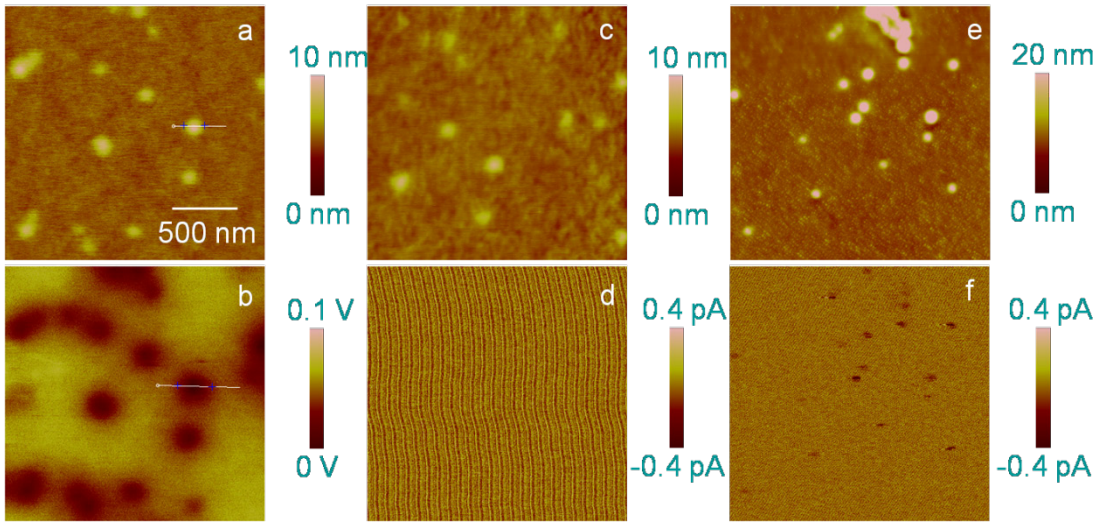

Figure 3.9. KPFM (a and b) and SCTMM (c, d, e, and f) measurements on individual AuNPs embedded in PS films of different t: a) and b) height and surface potential images before plasma etching, t = 70 nm; c) and d) height and current images before plasma etching, t = 70 nm, current bias = -12 V; e) and f) height and current images after 24 min plasma etching, t = 15 nm,current bias = -11.5 V.

The resolution of the current amplifier is 60 fA,[72] beyond this value I measure only noise. The tunneling current decreases exponentially with distance.[59,60] When the tip-AuNP distance exceeds 2 nm the current is too small to detect. For t > 40 nm, Δt is always >2 nm. For instant, when t = 70 nm, Δt is ~40 nm. Hence I could not observe any current signal for t = 70 nm. The plasma etching with a depth of 55 nm completely removed the PS film on top of the AuNPs. The electrons were thus able to tunnel through the percolation channel formed by the AuNP and the conductive tip. However, KPFM was able to detect the AuNPs even before the plasma etching. In this view the KPFM imaging mode is superior to the SCTMM mode if the conductive domains are covered by a thick dielectric film (>2 nm).

From the SCTMM measurements I conclude that no charge carriers tunneled more than 2 nm through the non-conductive PS matrix. Thus, when the AuNPs are too far away from the surface SCTMM fails. However, as discussed before, in this case I can still track them by KPFM.

With the combined analyses of KPFM and SCTMM on individual AuNPs I gain complementary information helping me to correlate the surface potential and the conductivity of the Au/PS system to its nanoscale morphology. By these two methods, I could determine the size of individual domains and the distance between them. However, the real structure of the conjugated polymers and their blends is usually not a simple 2D structure like my model system. The conductive domains are usually inhomogeneously distributed in the non-conductive polymer matrix. As well, the inter-distance between the domains varies. The measured surface potentials and conductivities will be different from those of individual AuNP samples. Hence I extend the study to analysis of samples of Au clusters.

3.3.4 KPFM and SCTMM analyses of Au clusters

In Au clusters, there are AuNPs stacking vertically, leading to surface of high roughness (peak to valley value). As proved previously, the cross-talk between topography and surface potential is minimized when the surface is smooth. To reduce the surface roughness I annealed the sample at 100 °C for 8 min after spin-coating PS film.

Figure 3.10 represents height and surface potential images of Au clusters embedded in a PS film of 56 nm thick (after annealing). On the height image I find two structures: the flat PS surface, and some clusters with $\Delta h \approx 5$ nm (**Figure 3.10a**). The surface potential of the clusters has a shadow-like feature (reddish area on **Figure 3.10b**), which is rather different from that of individual AuNPs. This shadow, or halo, is characterized by a smaller ΔV of only ~15 mV. There are also some areas that show the lowest surface potential inside the shadow (marked by red circles). ΔV of the red circled areas is up to ~150 mV. Outside the big shadow, there are also some areas (marked by white circles on) that show ΔV of ~40 mV.

However, on the height image these areas (marked by white circles) are completely flat.

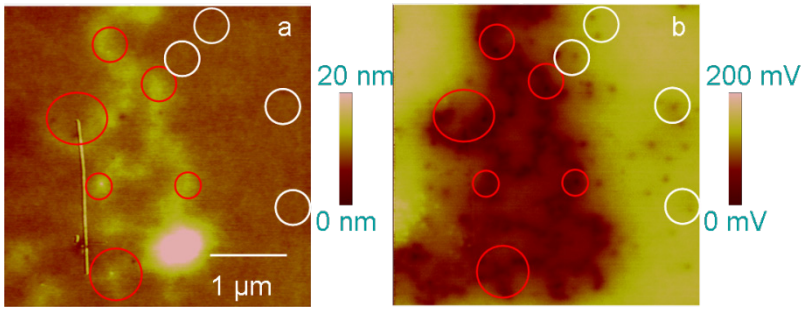

Figure 3.10. Height (a) and surface potential (b) images of Au clusters embedded in a PS film of t = 58 nm (after annealing); the red and white circled areas are the same position as the red circled area on **Figure 3.11**.

As addressed in **Section 2.2.1**, samples of Au clusters have both Au aggregates and individual AuNPs on the surface. The individual AuNPs should be completely covered by the PS film of t = 56 nm after annealing due to the stretching of PS during annealing. The height difference of ~5 nm is thus due to the presence of small aggregates, not to the individual AuNPs. ΔV of the shadow is too small for being generated by an individual AuNP embedded in a 56 nm thick PS film. In fact, I still measured ΔV of ~30 mV for an individual AuNP embedded in a 130 nm thick film (**Figure 3.3l**). Hence, the halo of the surface potential results from averaging all potentials generated by AuNPs that were proximal to the tip.[46,47] On the other hand, ΔV of the red circled areas is larger than that of the naked individual AuNP (~100 mV, **Figure 3.3b**). This ΔV could be generated by two vertically stacked AuNPs. ΔV of the white circled areas could be due to individual AuNPs completely covered by the PS film. However, at this stage, with KPFM only, I could not interpret all my observations. Hence I also carried out a SCTMM analysis on the same position of the sample.

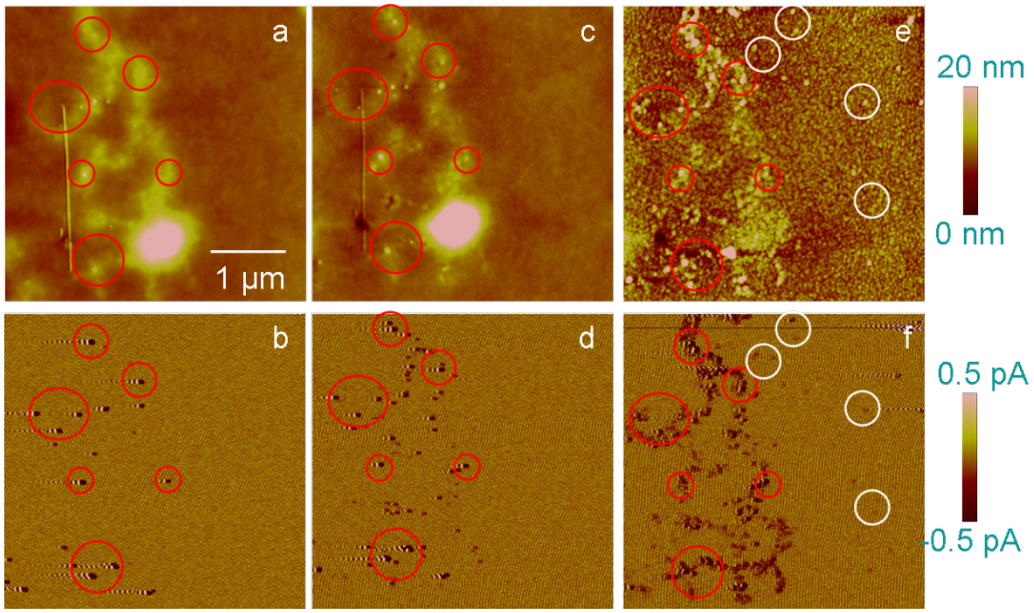

Figure 3.11. Height (a, c, and e) and current (b, d, and f) images of Au clusters embedded in PS films of different *t*: a) and b) before plasma etching, *t* = 56 nm, current bias = -10.5 V; c) and d) after 4 min plasma etching, *t* = 50 nm, current bias = -8.5 V; e) and f) after further 12 min plasma etching *t* = 24 nm, current bias = -6.0 V.

The height images in **Figure 3.10** and **Figure 3.11** confirm that both KPFM and SCTMM measurements were performed on exactly the same position. I marked similar features/areas on both by red and white circles. Before the plasma etching I measured single spot currents of up to ~10 pA inside the red circles by applying a bias voltage of -10 V (**Figure 3.11b**). After the first plasma etching *t* was reduced to ~50 nm. On the height image the topography of the clusters becomes clearer and the clusters inside the red circles also protrude out of the surface more than others (**Figure 3.11c**). The number of percolation channels also increases (**Figure 3.11d**). In this case, I measured again ~10 pA of the channels, but I applied a smaller bias voltage of -8.5 V. After further plasma etching of 12 min, *t* was reduced to ~24 nm. The surface becomes rougher and new particles start to appear inside the white circled areas (**Figure 3.11e**). I measured a similar current of ~9 pA through the red circled areas but with a even smaller voltage of -6 V. I also measured a current of ~2 pA for the particles that were previously not visible

on either height or current images (**Figure 3.11f**). The shape of the clusters on the current image is very similar to that on the height images (**Figures 3.12a**, **3.12c**, and **3.12e**). Different from the KPFM results, I do not observe any halos on the current images, as expected.

I have shown that electrons could only tunnel through a non-conductive layer of up to 2 nm. Here the non-conductive PS film is ~56 nm thick before the plasma etching. If there were only individual AuNPs on the surface Δt should be 15 – 35 nm, which is far beyond the tunneling limit. If two AuNPs stacked vertically, however, Δt could decrease to less than 1 nm. Hence the current measured on the sample of t = 56 nm (before plasma etching) results from conducting channels formed by two vertically stacked AuNPs with the silicon surface. The height images after the plasma etching further prove that the red circled areas represent parts of bigger clusters. The increasing number and conductivity of the conducting channels indicate that the PS film covering the AuNPs was progressively removed. The PS film was only partially removed after the first plasma etching, since only limited clusters were conducting current. The shape of the clusters is similar on both height and current images after the second plasma etching, indicating that the PS film was mostly removed. By comparing the KPFM and SCTMM results of the white circled areas, I confirm that the particles inside these areas are individual AuNPs. The measured current of these particles is still smaller (~2 pA) than that of the naked AuNPs (~6 pA). Apparently there is still residual PS on top of those individual AuNPs, but Δt is less than 2 nm.

The increasing surface roughness is possibly due to inhomogeneous plasma etching. No current or surface potential show a similar feature for the elevated bump (bright yellow area on the lower side of the images) in the height images (**Figures 3.11a**, **3.12a**, **3.12c**, and **3.12e**). It also disappears after the second plasma etching. Hence the bump is probably an inhomogeneity in the PS film.

Current flows only through individual channels and is not influenced by channels nearby. Hence SCTMM allows imaging with higher lateral resolution than KPFM, i.e. distinguishing among different conducting channels, and

measuring their distributions across the surface. Such information is essential for a quantitative analysis of the charge transport routes and of their distribution in conjugated polymers on the nanoscale.[4,6,37] However the trace of the individual AuNPs is completely lost in SCTMM when they are too deeply buried by the PS film. Only the supplementary information from KPFM allows doing so.

3.3.5. Influence of SCTMM measurement on KPFM measurement

All the KPFM measurements described above were performed before the SCTMM measurements. The current flow during SCTMM measurements could change the surface potential of samples. To study the influence of SCTMM measurement on KPFM measurement I performed two KPFM measurements right after the SCTMM measurement on individual AuNPs embedded in the PS film of t = 40 nm (**Figure 3.12**). I first applied a bias voltage of 12 V and scanned on an area of 2 x 2 μm by SCTMM. Then I performed a KPFM measurement on the same area with a larger scale of 5 x 5 μm. The surface potential of areas inside the white square is lower than that outside the square if a positive bias was applied (**Figure 3.12b**). While the surface potential of areas inside the white square is higher than that outside the square if a negative bias was applied (**Figure 3.12d**). The difference of surface potentials between the two regions is smaller if a smaller bias was applied.

The different sign of the applied voltage in SCTMM means different directions of the current flow. With a positive applied voltage, electrons tunnel from the tip to the sample, and vice versa. As a non-conductive polymer, the thick PS layer limits the electrons to tunnel through. The electrons thus accumulate on the PS surface during the SCTMM measurement and polarize the PS film. Hence the surface potential decreases after a positive voltage was applied to that area, and vice versa. The magnitude of the applied voltage determines degree of the change.

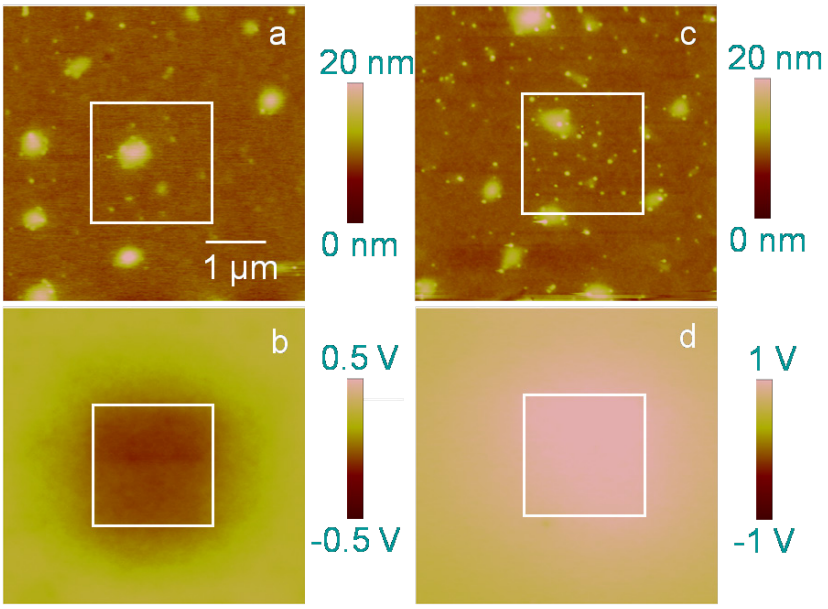

Figure 3.12. Height (a and c) and surface potential (b and d) images of individual AuNPs embedded in a PS film of t = 40 nm: a) and b) after a positive bias of 12 V was applied, c) and d) after a negative bias of 12 V was applied. Areas inside the white squares are positions where SCTMM measurements were performed.

I also observe similar surface potential changes on samples of t < 40 nm. Changes of the surface potential are smaller if Δt is smaller. However, the surface potential was always altered after the SCTMM measurement. Therefore the dielectric properties and the thickness of the barrier layer (PS film) influence the surface potential of the sample after SCTMM measurements.

From the combined KPFM and SCTMM study on the model system, I am able to correlate the KPFM and SCTMM data to material properties. I next tested the combined use of KPFM and SCTMM on a real system, PPy:PSS.

3.5. KPFM and SCTMM studies on PPy:PSS films

I used HOPG as the substrate, which is more conductive (resistivity 4 x $10^{-5}\Omega$ cm) than the highly doped silicon wafer (resistivity 1 – 20 Ω cm). Therefore in the STMM measurements of PPy:PSS films, I applied a lower voltage (~4 V) and used a less sensitive current amplifier (10 pA/V). **Figure 3.13** shows height, surface

potential, and current images acquired on the PPy:PSS film of ~80 nm. On the height images I find domains (yellowish areas on **Figure 3.13a**) with size of 20 – 30 nm. They protrude slightly out of the surroundings, but have a lower surface potential than the surroundings (reddish areas on **Figure 3.13b**). The current image shows that the percolation channels are mainly inside these domains (**Figure 3.13d**). When I compare the surface potential and the current images I notice some differences. The surface potential of each individual domain is rather uniform and of similar size, similar to the height image. The current signal of an individual domain, instead, appears like a bundle of two or more channels of smaller dimension.

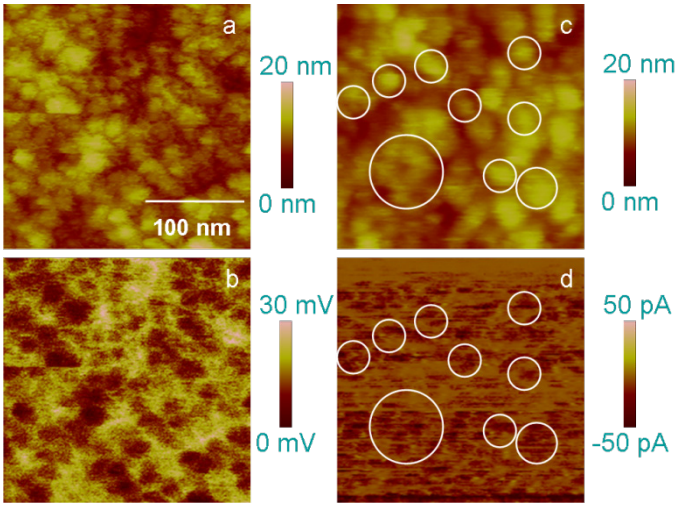

Figure 3.13. KPFM (a and b) and SCTMM (c and d) images of PPy:PSS films: a) and b) height and surface potential images; c) and d) height and current images, current bias = -4.1 V.

During the synthesis, PPy forms aggregates rather than being homogeneously dispersing in PSS. Therefore in the polymer film there must be regions with a higher PPy concentration, i.e. PPy domains; and regions with a higher PSS concentration, i.e. a PSS rich phase. In the next chapter I will prove that there is also PPy in the PSS rich phase and PSS in the PPy domains. The domains on the height images are thus conductive PPy domains, as supported by the current image. The diameter of the PPy domains measured here is consistent with that measured

by DLS (~26 nm, **Figure A1**). Based on the results of the Au/PS model system, I conclude that each individual conductive PPy domain with diameter of 20 ~ 30 nm consists of several PPy sub-domains with diameters smaller than 10 nm (**Figure 3.14**). The PPy sub-domains embedded in the PSS matrix form the actual percolation paths through the PPy:PSS film.

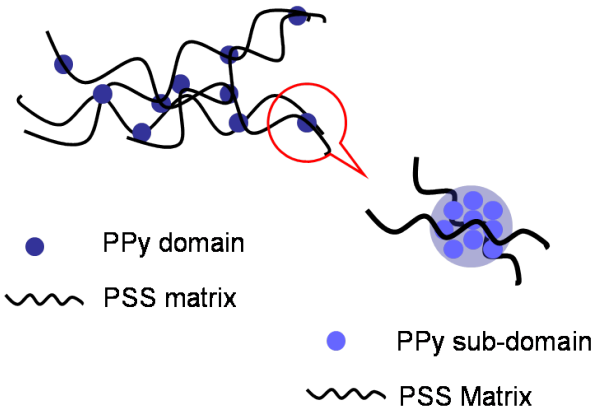

Figure 3.14. A schematic sketch of nanoscopic structure of PPy:PSS.

3.6 Summary and Conclusions

In this chapter I presented topography, KPFM and SCTMM studies on a model system of AuNPs embedded in a PS matrix. The nanoparticles were dispersed as individual particles or as clusters. The KPFM technique is very sensitive to changes of the surface potential, but its lateral resolution is of the orders of tens to hundreds of nanometers.[46,47] The SCTMM technique is a valid complement to KPFM, since it can map the distribution of conducting channels with a lateral resolution of a few nanometers.

I applied combined KPFM and SCTMM studies on films of a home-made conjugated PPy:PSS blend. I could relate surface potential and conductivity data with the nanoscale morphology of the blend. The analysis I presented is also consistent with information I have from the synthesis of the conjugated polymer blend and with data obtained by dynamic light scattering measurements. In the next chapter, I will show the influence of RH on the topography, electric and

dielectric properties of PPy:PSS films.

Chapter 4 Nanoscopic Topography and Dielectric Constants of PPy:PSS Films upon Humidity

4.1 Introduction

In the previous chapter, I have demonstrated that PPy forms conductive domains (20 – 30 nm) embedded in the non-conductive PSS matrix. Water content has a different influence (in terms of morphology, surface potential and dielectric constant) on PPy domains and on the PSS matrix, since PSS is more hydrophilic while PPy is more hydrophobic.[48,49,54] In this chapter I present an *in situ* study on the topographic, the electric (surface potential) and the dielectric (dielectric constant) response of PPy domains and PSS matrix to relative humidty (RH). I performed FM-KPFM on both thick and thin PPy:PSS films before and after annealing.

4.2 Experimental

4.2.1 Dielectric constant characterization by KPFM

The half oscillation amplitude, A_0, of the cantilever I used in this chapter is ~10 nm. This is of similar length scale as the thickness of thin film samples. Hence the contribution of the air gap above the sample to $\Delta A_{2\omega}$ cannot be neglected. This influence was also demonstrated in the previous chapter.[42] I therefore consider two capacitors in series that describe the gap between tip and substrate (**Figure 4.1**). One capacitor represents the contribution of the environment, and the other the contribution of the sample. The effective total capacitance is,

$$\frac{1}{C_{eff}} = \frac{1}{C_{envir}} + \frac{1}{C_s}, \text{ with } C_{envir} = \varepsilon_{envir} a / A_0 \text{ and } C_s = \varepsilon_s a / d . \quad (4.1)$$

Here a is the contact area, ε_{envir} is the dielectric constant of the environment, ε_s is the dielectric constant of the sample, and d is the sample thickness. **Equation 1.5** thus can be rewritten as

$$F_{2\omega} = \frac{1}{4} f(\varepsilon) g(a) V_{ac}^2 \cos(2\omega t) . \tag{4.2}$$

Here $f(\varepsilon)$ and $g(a)$ represent contributions from dielectric constants and tip geometry, respectively. Hence in the system described in this chapter, $F_{2\omega}$ depends on the dielectric constants of the environment and the sample, as well as on the tip geometry.

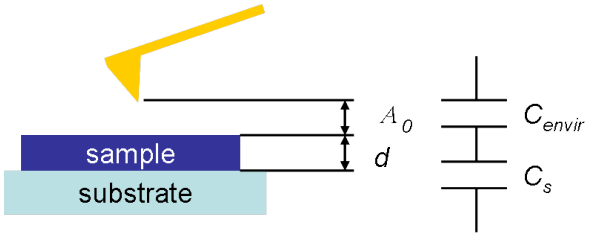

Figure 4.1. A schematic sketch of two capacitors formed between the tip and the substrate.

When the sample is protected in nitrogen, ε_{envir} is ~1.0.[105] The dielectric constant of water is ~78.[102] With increasing RH, the environment becomes a mixture of nitrogen and water. The contribution of water to ε_{envir} increases with RH. The dielectric constant of PPy:PSS also changes with RH due to the presence of water. In the following I will discuss how I distinguish between these two contributions.

4.2.2 KPFM measurement in controlled humidity

I used single-pass AM-FM KPFM (Agilent 5500 AFM with MAC III auxiliary controller, Agilent technologies Inc., Santa Clara, US) to obtain topography, surface potential and dielectric images simultaneously.[84] Topography was detected by AM mode by the first lock-in amplifier. Surface potential was detected by FM mode in the second lock-in amplifier. The change of the amplitude

at 2ω was detected by the third lock-in amplifier.

Only the height images were post-treated by the first order "line correction" with "Pico image basic" (version 5.1.1.5450). All other images display absolute values. I measured the height, phase, surface potential and $\Delta A_{2\omega}$ of the samples by cross-section analysis. For all experiments I used Pt-Ti coated conductive cantilevers (AC240, resonance frequency 70 kHz, Olympus, Japan) with tip radius of ~15 nm (**Figure A4c**).

I used two mass flow controllers (35828 mass flow controller, Analyt-Mtc Messtechnik GmbH, Müllheim, Germany) to control flow of nitrogen into the environmental chamber and into a washing bottle filled with MilliQ water. I controlled the two flows (mixed in the environmental chamber) until the desired RH was reached. RH was measured by a homemade temperature/humidity controller (precision of ± 5% in the range 5% < RH < 90%) with the sensor attached under the sample stage.

4.2.3 Types of samples

Thick PPy:PSS films: I performed KPFM measurements at two controlled states on both unannealed and annealed films: (i) the environmental chamber was dried with nitrogen overnight and RH ≈ 6%; (ii) water vapor was added overnight and RH ≈ 90%. The AC drive voltage to oscillate the cantilever was set to 0.9 V for unannealed samples, and to 1.1 V for annealed ones. The scan rate was set to 1.2 Hz, the modulation frequency ω to 5 kHz, and the detection gain of $\Delta A_{2\omega}$ to 2 x.

Thin PPy:PSS films: For each sample I selected areas covered by thinner films (brighter areas under an optical microscope of the AFM apparatus) and performed KPFM measurements at four controlled states on both unannealed and annealed films: (i) the first dry state, i.e. the environmental chamber was dried with nitrogen overnight for the first time and RH ≈ 7%; (ii) the first swollen state, i.e. water vapor was added until RH ≈ 80% for the first time; (iii) the second dry state, i.e. the environmental chamber was filled with nitrogen overnight for the second time and RH ≈ 7%; (iv) the second swollen state, i.e. water vapor was added again in

the environmental chamber until RH ≈ 80%. I call the first increase of RH from 7% to 80% the "first swelling procedure", and the second increase of RH the "second swelling procedure". The AC drive voltage to oscillate the cantilever was set to 1 V, the scan rate to 0.8 Hz, ω to 5 kHz, and the detection gain of $\Delta A_{2\omega}$ to 2 x.

Reference samples: I performed similar KPFM measurements at four controlled states on freshly cleaved HOPG and unannealed PSSH thin films. The four states were the same as those for PPy:PSS thin films. The practical parameters (V_{ac}, ω, scan rate and the detection gain of $\Delta A_{2\omega}$) for KPFM measurements on the reference samples were also set to be the same as those for measurements on the thin PPy:PSS films.

4.3 Thick PPy:PSS films

In OLEDs that use polymers as luminescent layer, the typical thickness of a hole transport layer is between 80 and 100 nm in order to smoothen the native roughness of the ITO electrode.[24,25] Therefore, I start with KPFM measurements on thick PPy:PSS films. The results I show in this section were from two representative samples (annealed and unannealed). Results of other samples were similar.

4.3.1 Influence of humidity on unannealed PPy:PSS

Figure 4.2 represents KPFM results of unannealed PPy:PSS film at RH = 6% and RH = 90%. On the height image taken at RH = 6%, I find some round domains with a diameter between 20 and 30 nm (**Figure 4.2a**). Compared to the surroundings each domain corresponds to lower surface potential and $\Delta A_{2\omega}$, as marked by red arrows (**Figures 4.2b** and **Figure 4.2c**). The surface potential difference ΔV of the domains with respect to the surroundings is ~100 mV and $\Delta A_{2\omega}$ of the domains is ~0.032 V. On the height image taken at RH = 90%, the contour of the domains becomes obscure and the diameter of them reduces to only 10 – 20 nm (**Figure 4.2d**). The surface potential and $\Delta A_{2\omega}$ of the entire PPy:PSS

film shift to higher values (more yellowish). There is almost no contrast between the domains and the surroundings on the surface potential image taken at RH = 90% (**Figure 4.2e**). However, on the dielectric image each domain still corresponds to lower $\Delta A_{2\omega}$, as marked by red arrows (**Figure 4.2f**). $\Delta A_{2\omega}$ of the domains is ~0.035 V.

The KPFM results obtained by Agilent instrument are in good agreement to those by Veeco instrument introduced in the previous chapter. The round domains are thus PPy domains, and the surrounding is PSS matrix. The PSS matrix absorbed water at high RH, while the PPy domains not.[49,54] The swollen PSS thus filled the voids between the PPy domains, which smoothened the entire film. This also explains why the round domains appeared shrunken on the height image taken at RH = 90% (**Figure 4.2d**).

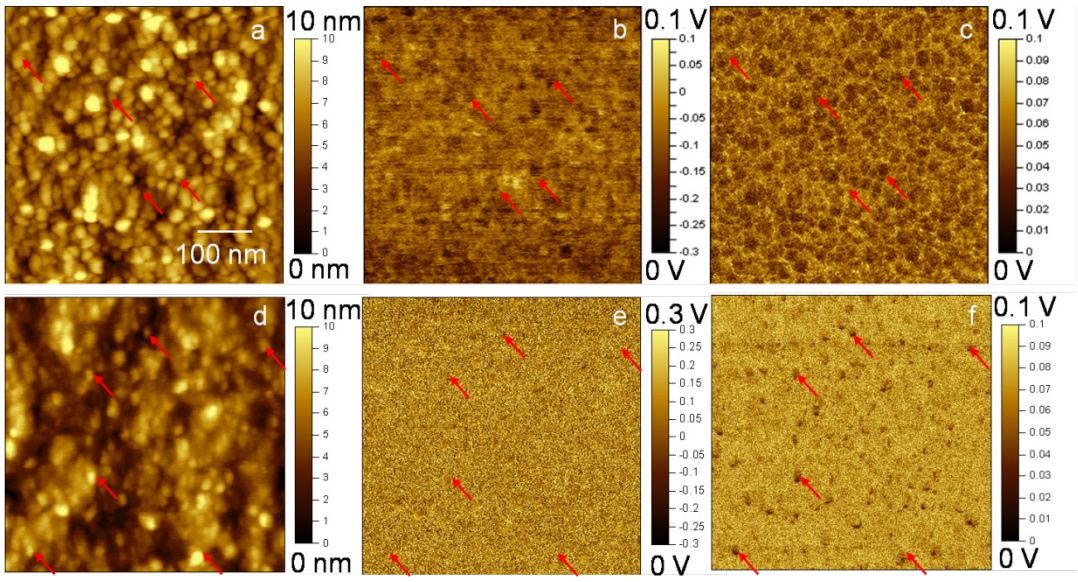

Figure 4.2. Height (a and d), surface potential (b and e), and dielectric images (c and f) of unannealed thick PPy:PSS film at different RH: a), b), and c) RH = 6%; d), e) and f) RH = 90%.

Surface potential of a single point measured by FM-KPFM is less averaged by its surroundings than that by AM-KPFM, as discussed in **Section 1.4.2**. This

explains why ΔV between the PPy domains and the PSS matrix measured by Agilent instrument (FM-KPFM, ~100 mV) is higher than that by Veeco instrument (AM-KPFM, ~30 mV). The adsorption of water on the sample surface caused ΔV between the PPy domains and PSS matrix decreasing to almost zero when RH increased to 90%. On the other hand, the surface potential of the entire film increased upon RH. There are two reasons for this. Firstly, the work function of the cantilever changed due to the adsorption of water, leading to changes of the measured surface potential of the sample (**Equation 1.9**). Secondly, water molecules adsorbed on the PPy:PSS surface in preferred dipole orientation.[106,107] The positive end (hydrogen) towards the environment caused an increase of the surface potential.

The lower $\Delta A_{2\omega}$(PPy) than $\Delta A_{2\omega}$(PSS) indicates that the dielectric constant of PPy is lower. Since only the dielectric constant of PSS increased with water sorption, and the dielectric constant of PPy remained almost unchanged, I could still track PPy on the dielectric image. The dielectric imaging is thus superior to the surface potential imaging in resolving materials of different dielectric constants upon RH.

4.3.2 Influence of humidity on annealed PPy:PSS

Figure 4.3 represents KPFM results of annealed PPy:PSS thick film at RH = 6% and RH = 90%. The topography of the annealed film is similar to that of the unannealed one at RH = 6% (**Figure 4.2a** and **Figure 4.3a**). Surface potential and dielectric constant of the annealed PPy domains are still lower than those of the PSS matrix at RH = 6% (**Figure 4.3b** and **Figure 4.3c**). With increasing RH, the topography of the annealed film remained almost unchanged (**Figure 4.3d**). However, I observe almost no contrast on either surface potential or dielectric image at RH = 90% (**Figure 4.3e** and **Figure 4.3f**).

The PSS segments shrink after thermal annealing if the coupling between PSS and the cation (in this case is PPy) is not strong.[108,109] Shrinking reduces the accessibility of PSS to water molecules, leading to a smaller degree of water

sorption and swelling. Hence the topographic change of the annealed film is smaller than that of the unannealed one. However, water vapor still adsorbed on the annealed sample surface, since the potential contrast between the PPy domains and the PSS matrix also became less pronounced upon RH. Different from the unannealed film, the surface potential of the annealed film is smaller at high RH (~90%) than that at low RH (~6%). This is possibly due to the fact that I used a new cantilever for each measurement. The reason for the dielectric changes is not yet clear at this stage.

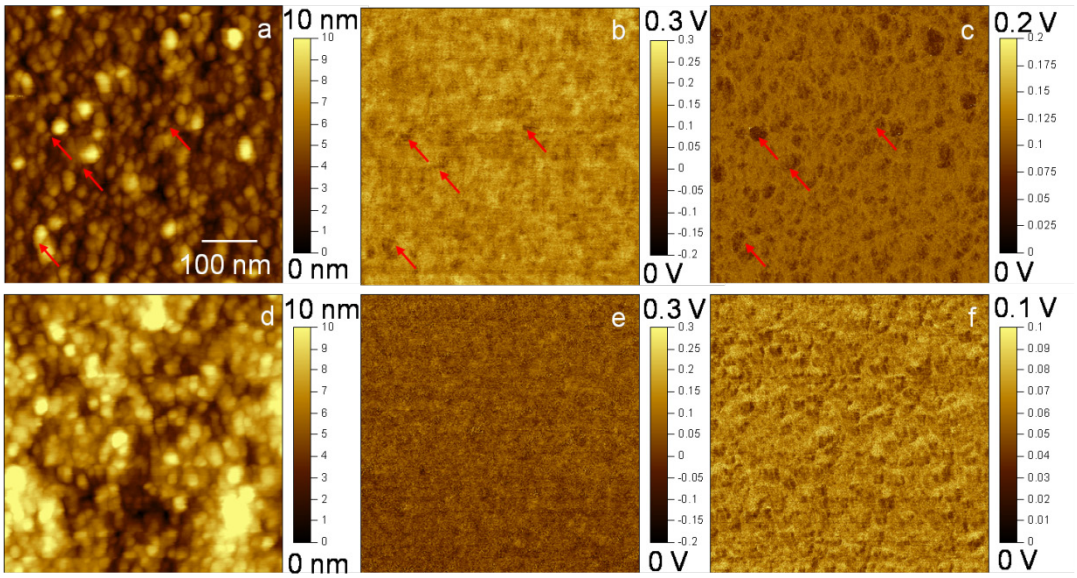

Figure 4.3. Height (a and d), surface potential (b and e), and dielectric images (c and f) of annealed thick PPy:PSS film at different RH: a), b), and c) RH = 6 %; d), e) and f) RH = 90%.

The unannealed and annealed PPy:PSS thick films show different topographic dependence on RH. The unannealed thick film becomes smoother upon RH due to the swelling of PSS, while the topography of the annealed film remains almost unchanged, due to the reduced water sorption.

However, there are some observations that I could not interpret, e.g. changes of $\Delta A_{2\omega}$ of annealed film upon RH. Further, the lateral resolution of KPFM is also reduced to several hundred nanometers for measurements on thick films, as

discussed in the previous chapter.[42] It is thus difficult to do quantitative analysis on surface potential or dielectric constant of PPy domains or PSS matrix individually. To this end, I performed similar KPFM measurements on thin PPy:PSS films upon RH. The measured surface potential is influenced by the tip work function, which also varies upon RH. Therefore for the following study, I do not discuss surface potential results. Nevertheless, I still recorded surface potential images (**Figure A9** and **Figure A10**) with topography and dielectric images simultaneously.

4.4 Thin PPy:PSS films

In this section for each study (i.e. unannealed and annealed studies) I only show results from one position of one representative sample. However, I observed similar changes of topography and dielectric constants upon RH on different positions of the same sample as well as of different samples (with the same preparation procedure).

4.4.1 Influence of RH on the topography of unannealed PPy:PSS

Topographic and dielectric images were taken simultaneously. I first look at the influence of humidity on topography and phase of unannealed PPy:PSS thin films. **Figure 4.4** represents the height and phase images of unannealed PPy:PSS thin film at different RH. On the height image taken in the first dry state (**Figure 4.4a**) I observe three types of structures with different heights: the flat HOPG surface at the bottom (dark color), some quasi-spherical particles (bright color) and some thin films (intermediate color). The relative height Δh of the thin films with respect to HOPG is ~1 nm, while that of the particle apices with respect to HOPG is up to ~9 nm. The height image taken at RH = 50% is similar to that in the first dry state (**Figure 4.4b**). The thin films grew in height (up to 7 nm) and appeared swollen and "rounded" after RH increased to 80% (**Figure 4.4c**). The overall topography of the thin film did not further change in the second swelling procedure (**Figure 4.4d** and **Figure 4.4e**), only Δh first decreased to ~4 nm and then increased

to ~7 nm. The shape and the size of the particles did not change significantly with RH. Δh of the particles increased ~10 % when RH increased from 7% to 80%.

On the phase images taken at RH = 7% and RH = 50%, I only observe phase contrast between the particles and HOPG (**Figure 4.4f** and **Figure 4.4g**). The contrast between the thin films and HOPG was small (1° – 2°). The phase contrast between the thin films and HOPG became more pronounced in the first swollen state (**Figure 4.4h**). This phase contrast persisted during the second swelling procedure (**Figure 4.4i** and **Figure 4.4j**).

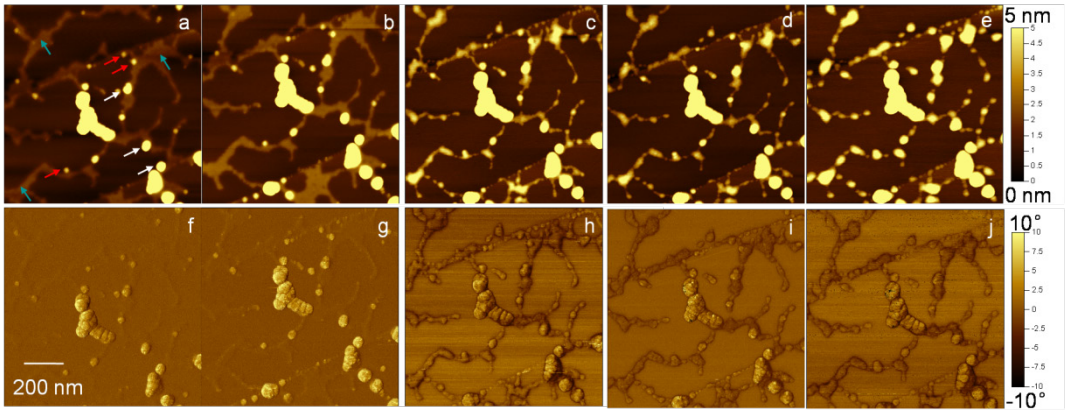

Figure 4.4. Height (a, b, c, d, and e) and phase (f, g, h, i, and j) images of unannealed thin PPy:PSS film at different RH: a) and f) the 1st dry state, RH = 7%; b) and g) RH = 50%; c) and h) the 1st swollen state, RH = 80%; d) and i) the 2nd dry state, RH = 7%; e) and j) the 2nd swollen state, RH = 80%.

The structure changes in the first swelling procedure indicate that a phase separation occurred in the PPy:PSS blend. The topography of the thin films shows RH dependence, while the topography of the particles does not. Hence the thin films could be the PSS matrix and the particles the PPy domains. The transformation of the PSS matrix from thin film patches to semi-spherical droplets indicates PSS swelling and dewetting on HOPG. At low RH, water preferably adsorbs on the PSS matrix. With increasing partial pressure of water, the PSS matrix also starts to absorb water and hence the PSS matrix swells. Since PSS is

not covalently attached to the HOPG surface, with increasing absorption of water the PSS matrix dewetts the HOPG surface. In fact, the water contact angle on HOPG is ~72°.[110] The critical RH for the onset of dewetting is ~80%. The sorption/desorption of water thus increased/decreased Δh of the PSS matrix. This result also confirms my previous conclusions of topographic response of the unannealed thick PPy:PSS films to RH. Similar behavior was also observed on other polyelectrolytes.[111] However, Δh of the PSS matrix in the second dry state is still larger than that in the first dry state. There could be two reasons for this. Firstly, dewetting induced an irreversible increase of Δh. Secondly, PPy sub-domains are also mixed in the PSS matrix, even if only in small amount. The morphologic changes of PSS were thus reduced when water desorbed, due to the electrostatic coupling between PPy (cation) and PSS (anion). The bulk PPy, on the other hand, should not show any swelling/de-swelling due to RH rising/sinking. The small variation of Δh of the PPy domains most probably resulted from some PSS mixed inside.

Before the swelling of the PSS matrix, I spot the PSS matrix only on the height images, but not on the phase images. PSS and HOPG, though, should exhibit a strong phase contrast due to their different elastic modulus ($E_{HOPG} \approx 10$ GPa and $E_{PSS} \approx 1$ GPa[112,113]). Hence, the small phase contrast between the PSS matrix and HOPG means that the PSS layer was so thin (~1 nm) that the tip still felt the HOPG surface underneath. The contribution of HOPG becomes less pronounced when Δh of the PSS matrix increases. The pronounced phase contrast between the PSS matrix and HOPG in the first swollen state confirms this conclusion.

The PPy domains and the PSS matrix exhibit different topographic response to RH in the unannealed thin PPy:PSS film. The morphology of the PSS matrix changed from a thin film to a semi spherical droplet in the first swelling procedure, due to combined swelling and dewetting of PSS. In the second swelling procedure, RH only influenced the water sorption of the PSS matrix, leading to a thickness variation of the PSS matrix. The topographic changes of thin PPy:PSS film upon

RH is in good agreement with those of thick PPy:PSS film. I will show in the next section that the dielectric constant of PPy:PSS is strongly influenced by the film morphology and by its water content. Controlling RH I could control topography, and thus alter the dielectric interaction between tip and sample.

4.4.2 Influence of RH on dielectric constants of unannealed PPy:PSS

Figure 4.5 represents dielectric images taken at different RH. Dielectric images were acquired simultaneously with the corresponding height and phase images in **Figure 4.4**. On the image taken in the first dry state, I only observe a dielectric contrast between HOPG and PPy, with $\Delta A_{2\omega}$(PPy) < $\Delta A_{2\omega}$(HOPG) (**Figure 4.5a**). The contrast between PSS and HOPG is negligible (~0.01 V). On the image taken at RH = 50%, the contrast between PSS and HOPG becomes more pronounced, with $\Delta A_{2\omega}$(PPy) < $\Delta A_{2\omega}$(HOPG) < $\Delta A_{2\omega}$(PSS) (**Figure 4.5b**). The dielectric contrast among PPy, PSS and HOPG persists but $\Delta A_{2\omega}$ of them shift to higher values on the image taken at RH = 80% (**Figure 4.5c**). In the second dry state, the dielectric contrast between PSS and HOPG 'switched', i.e. $\Delta A_{2\omega}$(PSS) < $\Delta A_{2\omega}$(HOPG) (**Figure 4.5d**). Finally, the dielectric image in the second swollen state is similar to that in the first swollen state (**Figure 4.5e**). Compared to the dielectric image in the first dry state, I also observe more black spots on that in the second swollen state (**Figure 4.5a** and **Figure 4.5e**).

The dielectric constant of HOPG (ε = 12 – 15[102]) is higher than that of PSSH ($\varepsilon \approx 9$[99]). Ideally $\Delta A_{2\omega}$(PSS) should be smaller than $\Delta A_{2\omega}$(HOPG) in a dry state. The similar $\Delta A_{2\omega}$(PSS) and $\Delta A_{2\omega}$(HOPG) in the first dry state thus resulted from the dominant contribution of HOPG under the PSS matrix, as proved by the phase images (**Figure 4.4f** and **Figure 4.4g**). At RH = 50%, water only adsorbed on the PSS matrix. Therefore, at RH = 50% $\Delta A_{2\omega}$(PSS) increased, while the topography of the PSS matrix remained nearly unchanged (**Figure 4.4b**). The dielectric response is thus more sensitive to the adsorption of a thin water film compared with the topographic response. With increasing RH, the sorption of water further increased $\Delta A_{2\omega}$(PSS), as shown by the dielectric image in the first swollen state. The

dielectric image taken in the second dry state reflects the intrinsic dielectric constants of PPy, PSS and HOPG. Hence, $\varepsilon_{PPy} < \varepsilon_{HOPG} < \varepsilon_{PSS}$. The dielectric response of unannealed thin PPy:PSS film to RH is in good agreement with that of unannealed thick one.

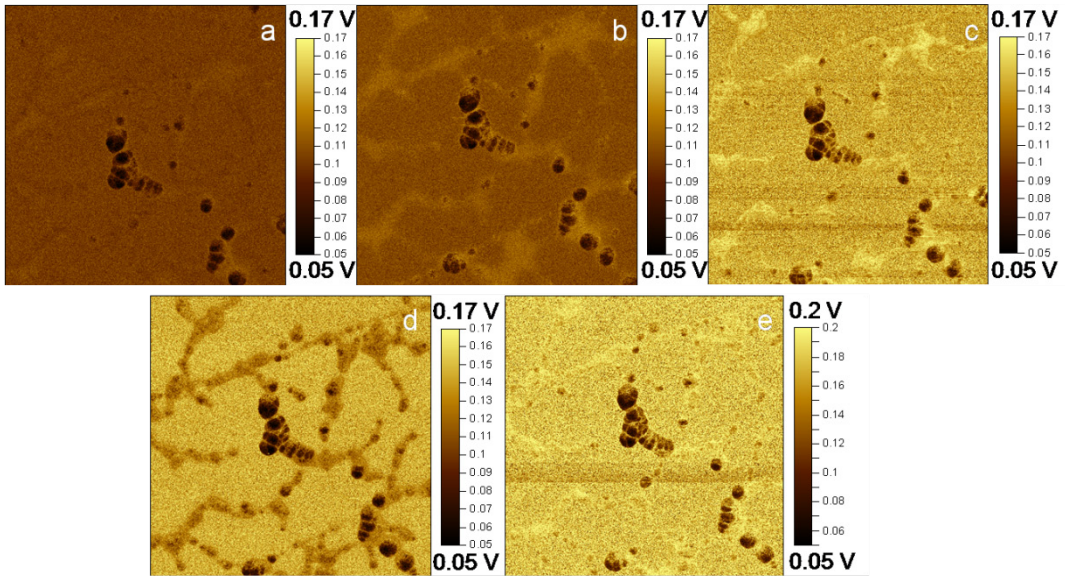

Figure 4.5. Dielectric images of unannealed PPy:PSS at different RH: a) the 1st dry state, RH = 7%; b) RH = 50%; c) the 1st swollen state, RH = 80%; d) the 2nd dry state, RH = 7%; e) the 2nd swollen state, RH = 80%.

I speculate the "newly appearing" black spots as PPy sub-domains. In the PSS matrix, PPy sub-domains are of small concentration and most of them were deeply embedded in the PSS matrix. Since water absorption swells the PSS matrix, new PPy sub-domains could be exposed to the surface, as detected by KPFM. The "newly appearing" PPy proves also that some PPy is dispersed in the PSS matrix from the beginning, although at a low concentration.

To specify the contribution of environment and sample to the measured $\Delta A_{2\omega}$, I measured and averaged $\Delta A_{2\omega}$ of selected areas on the PPy:PSS thin films (indicated by differently colored arrows in **Figure 4.4a**) and on HOPG, and plotted $\Delta A_{2\omega}$ versus RH (**Figure 4.6**). In the first swelling procedure, only $\Delta A_{2\omega}$(PSS) and $\Delta A_{2\omega}$(HOPG) show RH dependence. $\Delta A_{2\omega}$(PPy) is independent of RH. The

increase of $\Delta A_{2\omega}$(PSS) is stronger than that of $\Delta A_{2\omega}$(HOPG). However, $\Delta A_{2\omega}$(PSS) in the two dry states is similar. In the second swelling procedure, $\Delta A_{2\omega}$ of all structures shows stronger RH dependence compared to that in the first swelling procedure. The increase of $\Delta A_{2\omega}$(PSS) is strongest among the three materials. The "inversion" of the dielectric contrast between PSS and HOPG took place at RH between 70% and 80%, i.e. $\Delta A_{2\omega}$(PSS) < $\Delta A_{2\omega}$(HOPG) when RH ≈ 70%, while $\Delta A_{2\omega}$(PSS) > $\Delta A_{2\omega}$(HOPG) when RH ≈ 80%.

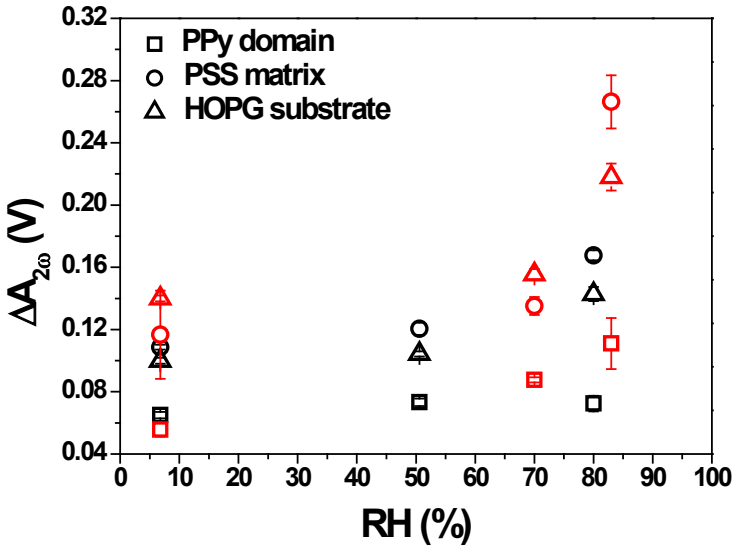

Figure 4.6. A plot of $\Delta A_{2\omega}$ of PPy, PSS and HOPG versus RH: Black symbols represent values taken from the 1st swelling procedure; red symbols represent values taken from the 2nd swelling procedure.

The constant $\Delta A_{2\omega}$(PPy) in the first swelling procedure indicates that the influence of ε_{envir} could be neglected and ε_s(PPy) dominated the measured $\Delta A_{2\omega}$(PPy). As I imaged PPy, PSS and HOPG simultaneously, the influence of ε_{envir} on $\Delta A_{2\omega}$(PSS) and $\Delta A_{2\omega}$(HOPG) could also be neglected. Hence, in the first swelling procedure the dielectric constants of materials dominated the measured $\Delta A_{2\omega}$. Although HOPG is very hydrophobic, Liscio *et al.*[107] reported that water could adsorb on the HOPG surface. I therefore attribute the increase of $\Delta A_{2\omega}$(PSS) and $\Delta A_{2\omega}$(HOPG) to the adsorption of water upon increasing RH. This result is also

in good agreement with the reference tests on HOPG and PSSH thin films, as I will show later. Due to the combined adsorption and absorption of water on the PSS matrix, the influence of RH on ε_s(PSS) is stronger than that on ε_s(HOPG). The switch of the dielectric contrast between PSS and HOPG in the second swelling procedure happened at higher RH (70 – 80%) compared to that in the first swelling procedure (RH ≈ 50%). This is possibly due to a nanoscopic rearrangement of PPy and PSS after the swelling of the PSS matrix, which I already addressed.

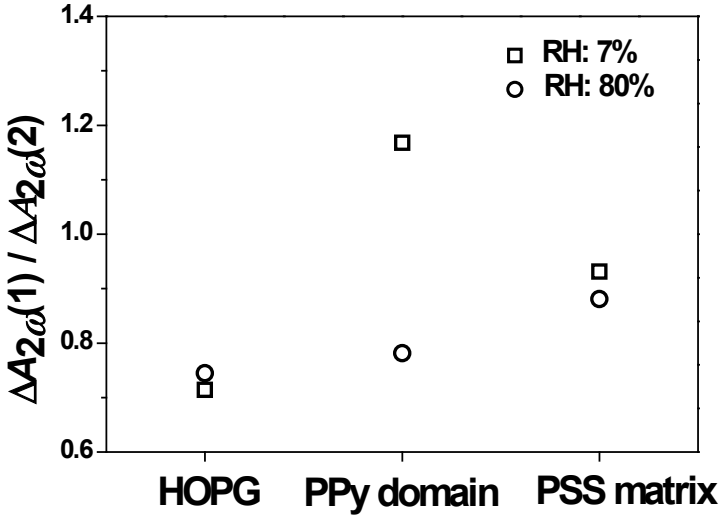

Figure 4.7. A plot of $\Delta A_{2\omega}(1) / \Delta A_{2\omega}(2)$ of different structures at RH = 7% (squares) and RH = 80% (circles).

The stronger RH dependence of $\Delta A_{2\omega}$ of all structures in the second swelling procedure indicates that other factors apart from RH influenced the dielectric interaction between tip and sample. The dielectric interaction depends not only on the ionic polarizability, but also on the tip geometry,[52,114] i.e. the contact area a. Although I used the same tip during a whole series of experiments, changes of the geometry at the end of the sharp tip after many scans could not be neglected. To exclude the tip effect, I compare $\Delta A_{2\omega}(1) / \Delta A_{2\omega}(2)$ of PPy, PSS and HOPG at the same RH respectively. If the difference between $\Delta A_{2\omega}(1)$ and $\Delta A_{2\omega}(2)$ was only caused by the geometry of the tip, for the same RH I should have $f(\varepsilon_{envir1}) = f(\varepsilon_{envir2})$,

and $f(\varepsilon_{s1}) = f(\varepsilon_{s2})$. By applying them to **Equation 4.2**, I have

$$\Delta A_{2\omega}(1) / \Delta A_{2\omega}(2) = F_{2\omega}(1) / F_{2\omega}(2) = g(a_1) / g(a_2) = a_1 / a_2 . \quad (4.3)$$

Therefore, for the same RH the ratio $\Delta A_{2\omega}(1)$ / $\Delta A_{2\omega}(2)$ should only depend on changes of the contact area, regardless of which structure is studied.

I selected $\Delta A_{2\omega}$ of PPy, PSS and HOPG at RH = 7% and RH = 80% from **Figure 4.6** and plotted $\Delta A_{2\omega}(1)$ / $\Delta A_{2\omega}(2)$ (**Figure 4.7**). The ratio is different for different structures at both RH = 7% and RH = 80%. For each measurement, PPy, PSS and HOPG were contacted similarly by the tip. If the stronger increase of $\Delta A_{2\omega}$ in the second swelling procedure was only due to changes of the tip geometry, the ratio should remain constant for the same RH. This is not the case. I suggest that the stronger increase of $\Delta A_{2\omega}(2)$ may result from a change of surface composition of PPy:PSS, as explained previously. A similar water induced composition variation was also observed on PEDOT:PSS by Koch *et al*.[34] They observed a stronger absorption signal from PEDOT by XPS after exposing the sample to water.

In summary $\Delta A_{2\omega}$ is more sensitive to study humidity changes and it shows different RH dependence compared to topography. In the first swelling procedure the sorption of water in the PSS matrix dominated changes of $\Delta A_{2\omega}$. In the second swelling procedure the swelling of the PSS matrix induced changes of surface composition, leading to different $\Delta A_{2\omega}$. The surface composition change or rearrangement was not detected by the topographic imaging or on the thick PPy:PSS film. The study of dielectric response of thin PPy:PSS films upon RH allows me to understand more in detail the nanostructure of PPy:PSS films and their response to humidity.

4.4.3 Influence of RH on annealed PPy:PSS

Figure 4.8 represents height images of annealed thin PPy:PSS film at different RH. On the height image taken in the first dry state, there are also three structures: particles, thin films and the flat HOPG surface (**Figure 4.8a**). The

particles are thus PPy domains, the thin films are PSS matrix. The topography of the annealed PPy:PSS film at RH = 7% is similar to that of the unannealed one (**Figure 4.8b**). There are small "holes" appearing in the PSS matrix (as indicated by white arrows) at RH = 90%. Δh of the PSS matrix also increased from ~1 nm at RH = 7% to ~2 nm at RH = 90%. The height image taken in the second dry state is very similar to that in the first swollen state, only Δh of the PSS matrix decreased back to ~1 nm (**Figure 4.8c**). The topography of the PPy domains, however, remained unchanged upon RH.

Compared to the unannealed film, the topography of the annealed film (both PPy domains and PSS matrix) was only weakly influenced by RH. The formation of small holes in the PSS matrix in the first swollen state indicates that the PSS matrix still swelled and dewetted on HOPG in the swollen state, but to a smaller degree. As discussed in **Section 4.3.2** thermal annealing reduces the absorption of water in the PSS matrix. On the other hand, annealing also increases the adhesion of the PPy:PSS film to the HOPG substrate, thus reducing dewetting.

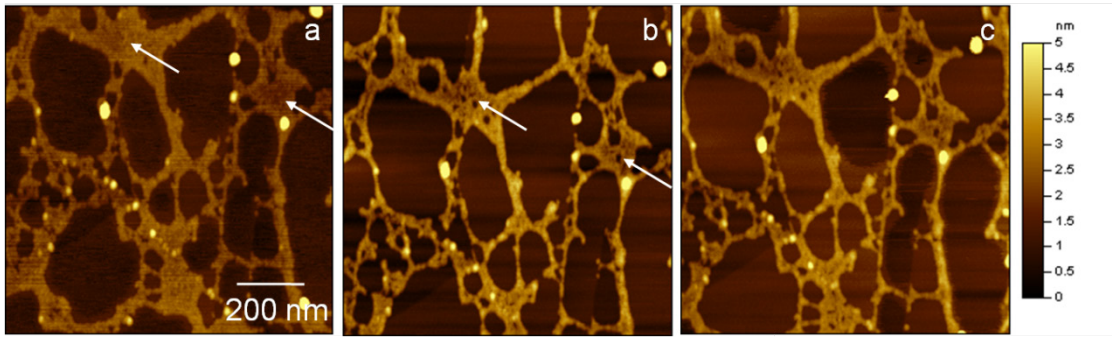

Figure 4.8. Height images of annealed PPy:PSS thin film at different RH: a) the 1st dry state, RH = 7%; b) the 1st swollen state, RH = 90%; c) the 2nd dry state, RH = 5%.

To quantitatively compare changes of the dielectric constants of annealed thin PPy:PSS film at different RH, I plotted $\Delta A_{2\omega}$ of PPy domains and PSS matrix versus RH (**Figure 4.9**). Each data point on the plot was averaged from $\Delta A_{2\omega}$ of minimum 5 positions (**Figure A11**). Similar as unannealed PPy:PSS, for annealed

PPy:PSS, $\Delta A_{2\omega}$(PPy) is smaller than $\Delta A_{2\omega}$(PSS) in all states. $\Delta A_{2\omega}$(PPy) is almost constant, while $\Delta A_{2\omega}$(PSS) increased by ~30% when RH increased from 7% to 90%. This increase is much smaller compared to that of unannealed thin films (~150 % for $\Delta A_{2\omega}$(PSS)). Changes of $\Delta A_{2\omega}$ were mainly induced by water for unannealed thin PPy:PSS films. The reduced water sorption of the PSS matrix thus decreases the degree of the RH dependence of $\Delta A_{2\omega}$ for the annealed PPy:PSS thin films. Also I do not observe swelling induced surface composition variation on annealed thin PPy:PSS film due to the reduced degree of the swelling of PSS.

Both the topographic and dielectric changes of annealed thin PPy:PSS film are smaller compared to those of unannealed one. These results are also in good agreement with those of thick PPy:PSS films. The annealed films show thus a stronger resistance to the sorption of water and the processes associated with it. This finding could well explain why annealing of conjugated polymers usually results in an improved device performance.[115,116]

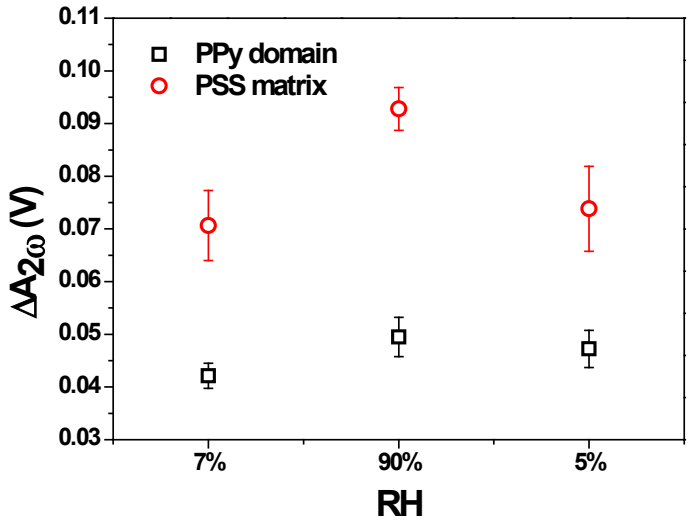

Figure 4.9. A plot of $\Delta A_{2\omega}$ of PPy domains and PSS matrix at different RHs.

4.5 Reference tests

4.5.1 Influence of RH on freshly cleaved HOPG

Some of my previous discussions are based on dielectric properties of HOPG. Although after drop-coating the excess PPy:PSS was removed by a nitrogen gun, there might be some residual thin patches of PPy:PSS on the HOPG substrate. The residual PPy:PSS patches may not be detected by the topographic imaging, but they could change the dielectric constant of HOPG. I thus used freshly cleaved HOPG as a reference and studied its dielectric response to RH. The dielectric image of the freshly cleaved HOPG is homogeneous over the entire scan area regardless of topographic variations (**Figure 4.10a** and **Figure 4.10b**). $\Delta A_{2\omega}$(HOPG) increases with RH (**Figure 4.10c**). There are two reasons. Firstly ε_{envir} increases with RH, resulting in a stronger dielectric interaction between tip and HOPG. Secondly, the thin water layer adsorbed on the HOPG surface[107] can also increase $\Delta A_{2\omega}$ (HOPG). The dielectric response of the freshly cleaved HOPG to RH is similar to that of the HOPG substrate used for drop-coating thin PPy:PSS films. This validates the conclusions of the previous paragraphs.

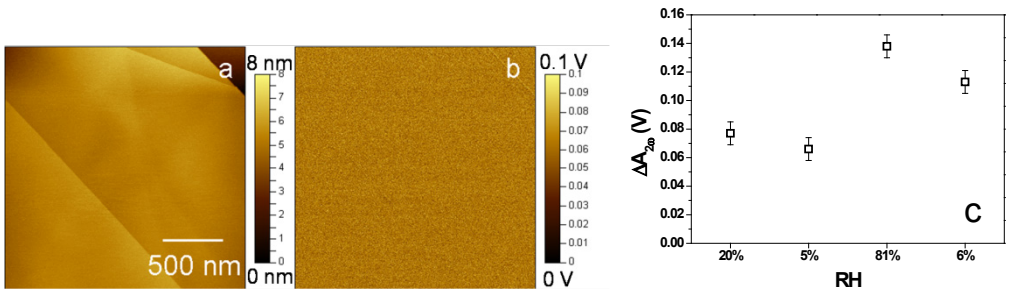

Figure 4.10. Height (a) and dielectric (b) images of freshly cleaved HOPG taken in the first dry state (RH = 7%); (c) a plot of $\Delta A_{2\omega}$ at different RH.

4.5.2 Influence of RH on unannealed thin PSSH films

Figure 4.11 shows height and dielectric images of PSSH thin film taken at different RH. In the first dry state I observe a thin film with some small "holes" (**Figure 4.11a**). The thin film is PSSH and the holes represent HOPG that was not covered by the polymer film. The topography of the PSSH film changed when RH = 80% (**Figure 4.11b**). The holes grew larger and Δh of the PSSH film increased

from ~3 nm to ~5 nm. The film was also thicker at the rim of the holes, which is typical for dewetting features.[117] The topography of the PSSH film remained unchanged in the second swelling procedure (**Figure 4.11c** and **Figure 4.11d**). Only Δh of the PSSH film increased again from ~3 nm to ~5 nm. $\Delta A_{2\omega}$(PSSH) was smaller than $\Delta A_{2\omega}$(HOPG) in both dry states (**Figure 4.11e** and **Figure 4.11g**). The difference between $\Delta A_{2\omega}$(PSSH) and $\Delta A_{2\omega}$(HOPG) was ~0.04 V in the first dry state and ~0.01 V in the second dry state. In the two swollen states, $\Delta A_{2\omega}$(PSSH) was larger than $\Delta A_{2\omega}$(HOPG) (**Figure 4.11f** and **Figure 4.11h**), with a similar difference of ~0.02 V.

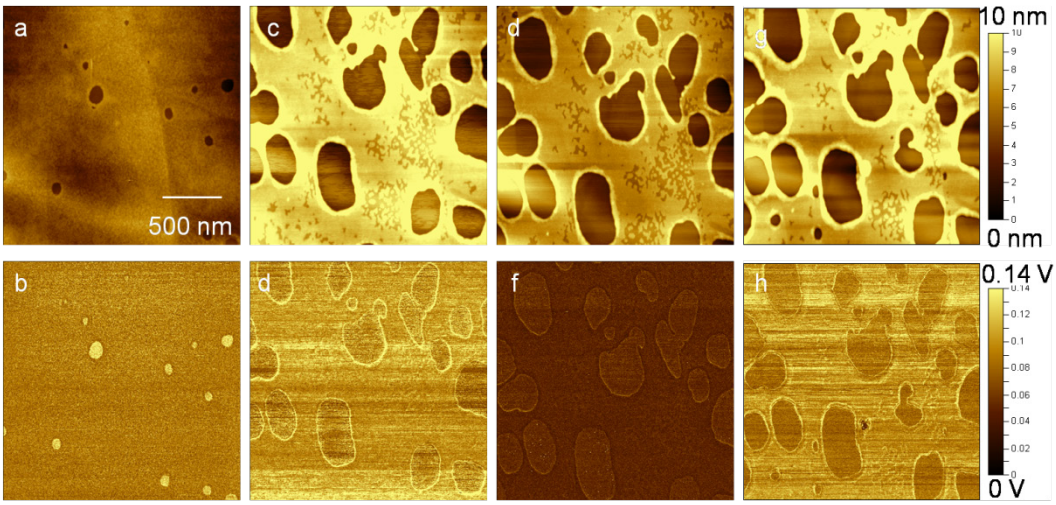

Figure 4.11. Height (a, b, c, and d) and dielectric (e, f, g, and h) images of thin PSSH film at different RH: (a) and (e) the 1st dry state, RH = 7%; (b) and (f) the 1st swollen state, RH = 80%; (c) and (g) the 2nd dry state, RH = 7%; (d) and (h) the 2nd swollen state, RH = 80%.

The topographic response of the PSSH film to RH is very similar to that of the PSS matrix in the PPy:PSS films. PSSH also swelled and dewetted in the first swollen state. Δh of the PSSH film was influenced by two factors due to the larger covered area compared to the PSS matrix in the previous experiments. At the rim of the holes, the dewetting caused an increase of Δh, which was irreversible. Away from the rim, the swelling of PSSH was reversible.

The difference of $\Delta A_{2\omega}$(PSSH) and $\Delta A_{2\omega}$(HOPG) in the first dry state is higher compared to that of $\Delta A_{2\omega}$(PSS) and $\Delta A_{2\omega}$(HOPG). The PSSH film is thicker than the PSS matrix in the PPy:PSS film. Hence, the measured $\Delta A_{2\omega}$(PSSH) was dominated by the dielectric constant of PSSH other than that of HOPG. The dependence of $\Delta A_{2\omega}$(PSSH) on RH is similar to that of $\Delta A_{2\omega}$(PSS). Further I did not observe dark spots on the dielectric image of the PSSH film in the swollen states, since there is no PPy inside. Also these results validate the conclusions of the previous paragraphs.

4.6 Summary and conclusions

In this chapter, I have demonstrated by KPFM that water could change the nanoscopic structure and the dielectric constant of both thin and thick films of a conjugated polymer blend, PPy:PSS. The thick and thin PPy:PSS films show similar topographic and dielectric response to RH. However, I can perform a quantitative analysis only on thin PPy:PSS films, due to the low spatial resolution of KPFM on thick films.

For unannealed thin films, I observed irreversible topographic and surface nanostructure changes, due to the swelling and dewetting of the hydrophilic PSS matrix on HOPG. Swelling of the PSS matrix also initiates a phase separation and changes the surface composition of the PPy:PSS blend. Dielectric imaging, which is a variety of KPFM, is more sensitive to water sorption than topographic imaging. I was only able to detect the change of surface composition by measuring the dielectric interaction between tip and thin PPy:PSS film. Thermally annealed PPy:PSS films (both thick and thin films) exhibit a stronger resistance to water sorption compared with unannealed ones. This substantiates the practice of annealing conductive polymer films for better device performances.

Chapter 5 Nanoscopic Conductivity Measurement of Single Particles

5.1 Introduction

In previous chapters I have introduced the electric and dielectric property studies of conjugated polymer films formed on substrates after spin-coating or drop-coating. In this chapter, I introduce a direct and versatile method to measure the nanoscopic conductivity of single particles by a microscopic four-point probe method. The method is intended to measure conductivity of single PPy particles with a diameter of a few micrometers. I started with metal and metal coated particles of a few micrometers as models. I used square pyramidal pits on a silicon chip to immobilize the single particle and developed two geometries of electrode arrays to establish the four contacts, i.e. bottom contact (the particle is contacted from its bottom) and top contact (the particle is contacted from its top). To apply the concept of the macroscopic four-point probe method,[118,119] I controlled the distance *d* between two adjacent electrodes to be equal.

5.2 Experimental

5.2.1 Macroscopic four-point probe method

In the macroscopic four-point probe method, four equidistanced electrodes contact the sample and are arranged either in a line[118,119] or a square (Van der Pauw method[120]). The current *I* is applied to the two outer electrodes, and the voltage drop *V* is measured between the two inner ones (**Figure 5.1a**). Since no current flows through the two inner electrodes, the contact resistance between these electrodes and the sample surface is eliminated.[119] The same also applies for the

square geometry (**Figure 5.1b**). The conductivity σ is calculated by

$$1/\sigma = \frac{\pi}{\ln 2} \cdot \frac{V}{I} \cdot t \,. \tag{5.1}$$

Here t is the film thickness. **Equation 5.1** is valid with three criteria: (i) the contacts are sufficiently small and of equal size; (ii) t is much smaller than the area of the measured sample; (iii) $t << d$.

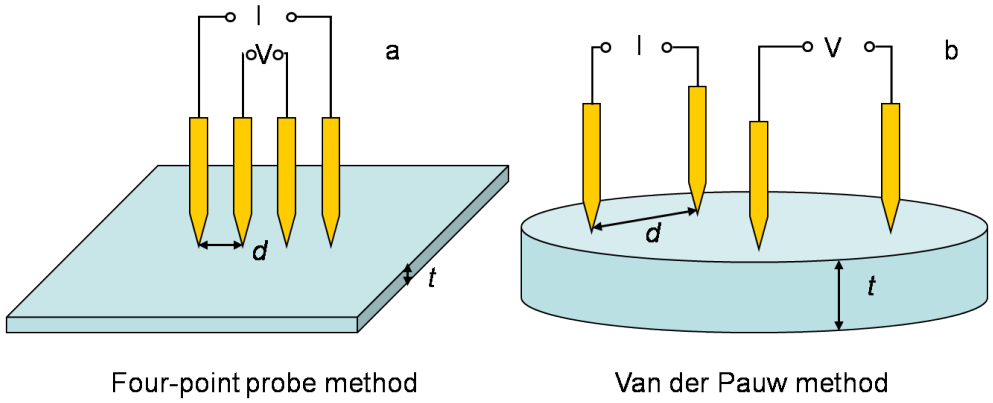

Figure 5.1. Schematic sketches of conductivity measurements by four-point probe method (a) and Van der Pauw method (b).

5.2.2 Microscopic four-point probe measurement

I used a Keithley sensitive source meter (6430, Keithley instruments GmbH, Germering, Germany) to measure the nanoscopic conductivity of single particles. The connection between the four probes of the source meter and the microelectrodes is established through a socket, as described in **Section 2.2.6** (**Figure 2.4c**). I connected every two adjacent electrodes to the voltage meter, and the other two to the current source (constant current) of the source meter. Therefore for each particle (connected by the four electrodes), there are four different connections (different electrodes connected to the source meter). For each connection, I applied constant I and measured V. I also increased and decreased I and measured V for each change of I.

5.2.3 EDX measurement on Ag core-shell particles

To measure the content of sulfur in the conductive Ag layer, I did EDX

measurements (FEI Nova 600 Nanolab) on Ag core-shell particles. The current and voltage of the electron beam were set to 0.15 nA and 20 kV respectively. The atomic ratio of sulfur to silver was analyzed from the resulting spectra (**Figure A12**).

5.3 Results and discussion

The distribution of the electric field inside the conductive layer depends on its thickness and conductivity. Therefore the measured resistance ($R = V/I$) and the formula used to calculate the conductivity are different for core-shell and bulk particles. I thus discuss the results of Ag core-shell particles and Au bulk particles separately. For each type of particles, I used both "bottom contact" and "top contact" electrode configurations.

5.3.1 Conductivity measurement of Ag core-shell particles

The silver layer of the Ag core-shell particles is between 100 – 200 nm thick, which is much smaller than their diameter (~2 μm). This geometry corresponds to requirements of the four-point probe method, since $t << d$.[119] One can thus derive a formula to calculate the conductivity of the core-shell particle.

5.3.1.1 Conductivity measured via "bottom contact"

In the "bottom contact" geometry, the particle was deposited after the electrode separation. Electric properties of the particle are thus not modified by electron or ion beams. After placing the Ag core-shell particle inside the pyramidal pit, the four electrodes should be contacted by the conductive Ag layer. Therefore, the measured resistance V/I should decrease. However V/I of all tested Ag core-shell particles remains in the range of TΩ, which is too high for a particle with a conductive layer of silver of 100 – 200 nm. According to the SEM images of the Ag core-shell particle before and after the FIB etching, the conductive layer is not homogeneous (**Figure 2.2a** and **Figure 2.2b**). Instead, nanoscopic Ag domains

(~10 nm in diameter) are formed. The contact area between the particle and the Ti-Au electrodes thus decreased. Further, some particles did not sit right in the center of the pits, as proved by SEM images taken after the measurement (**Figure 5.2**). Hence, the four contact areas are not similar anymore and the contact resistance cannot be neglected.

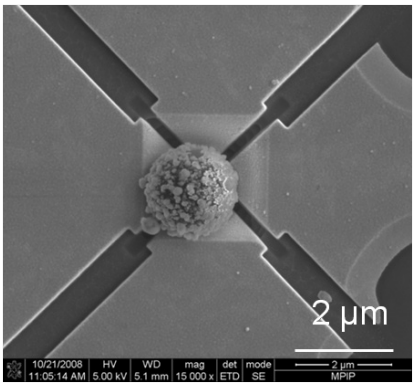

Figure 5.2. A SEM image of an Ag core-shell particle sitting inside a pyramidal pit.

5.3.1.3 Conductivity measured via "top contact"

In the "top contact" geometry the contact area between the particle and electrodes, as well as the distance between the two adjacent electrodes were controlled during the FIB deposition. I therefore overcome disadvantages of the bottom contact geometry. **Figure 5.3a** shows a representative plot of *V*/*I* for an Ag core-shell particle upon applying *I*. The squares represent *V* recorded upon increasing the current, and the circles represent *V* acquired upon decreasing the current. Each curve represents a connection of the corresponding electrodes (as indicated by the same number) to the voltage sensor of the source meter (**Figure 5.3a** inset). The measured values of *V*/*I* are similar (80 – 200 kΩ) for all three connections with only small deviations. For each connection, *V*/*I* is independent on *I*.

The similar values of *V*/*I* of the three connections indicate that the four contact areas are similar. For metals, the value of *V*/*I* should be constant according

to Ohm's law. For polymers (semi-conducting or insulating), however, I is proportional to V^2 as described by Mott-Gurney equation.[61] The constant value of V/I over the whole measuring range thus indicates that the current only flows inside the conductive Ag layer, i.e. through percolation channels formed by nanoscopic conductive Ag domains.

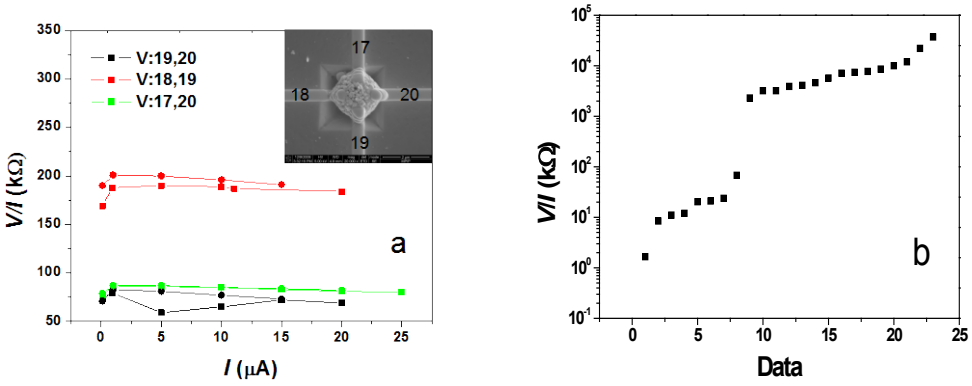

Figure 5.3. a) V/I of an Ag core-shell particle upon increasing (squares) and decreasing (circles) I; insect: a SEM image of the Ag core-shell particle connected with numbered electrodes; b) a statistic analysis of V/I.

Figure 5.3b represents a statistic analysis on V/I of 28 particles from two chips. Some electrodes were damaged during the measurement. I discarded the data obtained by the damaged electrodes, and collected 23 effective data points. The values of V/I of most particles lie in the two regions, 100 kΩ and 10 MΩ. The deposition of Pt electrode was not only on the flat Ti-Au electrode, but also on the spherical Ag particle. During the Pt deposition, the deposited Pt might fall into the pyramidal pit that the Ag particle sits in. Therefore, there might be small gaps in the Pt electrodes, which results in higher V/I. I thus discard the higher values of V/I and choose V/I = 100 kΩ for the calculation.

The conductivity of the Ag core-shell particle is calculated by a formula developed by Andrienko,[121]

$$\sigma = 0.11t/\left(\frac{V}{I}\right), \text{ with } t << d. \tag{5.3}$$

Here t is the thickness of the conductive layer and d is the distance between the two adjacent electrodes. Geometry of a conductive plane with 4 electrodes standing in a square is considered in **Equation 5.3**. The equation for the spherical geometry is not yet completed. But it will only differ from **Equation 5.3** by a prefactor. Hence I use **Equation 5.3** for a preliminary calculation. According to values obtained from SEM images (**Figure A13a**), $t \approx 200$ nm and $d \approx 1.2$ μm. For $V/I = 100$ kΩ, the conductivity is $\sigma \approx 0.1$ S/cm.

The calculated conductivity of the Ag core-shell particle is much lower than that of pure Ag, i.e. 6.3 x 10^5 S/cm.[122] There are several reasons for this. Firstly, in the core-shell Ag particle, the conductive Ag layer is only ~200 nm, and the rest is insulating melamine resin. The conductivity of the entire particle thus decreases. Secondly, due to the nanoscopic inhomogeneity of the Ag layer, current percolates between neighboring Ag domains, leading to reduced conductivity of the particle. Thirdly, Ag can be vulcanized and oxidized when stored in air. The conductivity of Ag_2S is 10^{-3} – 10^{-5} S/cm.[123-125] The existence of Ag_2S could thus reduce the conductivity of the Ag layer by several orders of magnitude, depending on its concentration.

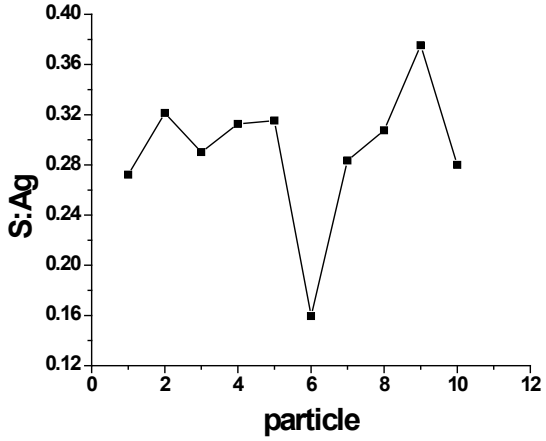

Figure 5.4. A plot of the atomic ratio of S to Ag in 10 Ag core-shell particles, as measured by EDX spectroscopy.

Figure 5.4 represents the atomic ratio of sulfur to silver (S:Ag) in 10 Ag core-shell particles, as measured by EDX. The absorption signal of S in the EDX spectra (**Figure A12**) only results from vulcanized Ag (Ag_2S). The average S:Ag ratio is ~0.3, indicating that almost 50% Ag was vulcanized. I therefore attribute the vulcanization of Ag as the main reason for the conductivity decrease of Ag core-shell particles.

The bottom contact geometry is not suitable for measuring the conductivity of the single Ag core-shell particle due to the poor contact between the particle and the microelectrodes. With the top contact geometry, I obtain conductivities of Ag core-shell particles of ~0.1 S/cm. The vulcanization of the conductive Ag layer could be the main reason for the low conductivity. The non-uniform conductive layer could also reduce the total conductivity of the particle. A particle with a uniform and stable conductive layer should be used as a comparison. I therefore performed similar experiments on Au bulk particles.

5.3.2 Conductivity measurement of Au bulk particles

Compared to Ag, Au is relatively chemically inert and thus will not be oxidized or vulcanized when stored in air. The surface of the Au bulk particle is also relatively smooth, as proved by SEM images (**Figure 2.3**). However for the bottom contact geometry, the measured V/I is also in the range of TΩ. A good contact between the four electrodes and the single Au particle could thus not be established, most probably due to the small contact area (point contact) between the spherical particle and four flat surfaces.

Since current could not flow through the contact of the Au-Ti electrode and the conductive particle, I directly deposited Pt electrodes on top of the Au particle (**Figure 5.5a**). The dimension of the Pt electrodes is described in **Section 2.2.7** and shown on the SEM image (**Figure 5.5a**). **Figure 5.5b** represents V/I values of a single Au particle upon applying I. Each curve represents the corresponding electrode (as indicated by the same number) connected to the voltage sensor of the source meter. $V/I \approx 100\ \Omega$ and is almost constant over the whole range, with some

exceptions occurring at I = ~100 µA. The four curves almost overlap except for those jumps.

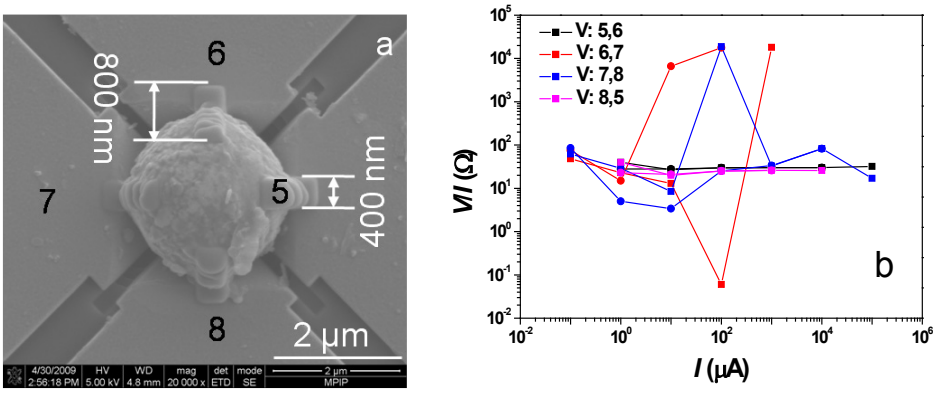

Figure 5.5. a) A SEM image of an Au particle connected by four Pt electrodes; b) a plot of V/I measured upon increasing (squares) and decreasing (circles) I.

The preamplifier of the source meter automatically switched detection range at $I \approx 100$ µA. This switching probably caused the instabilities in the measured values, leading to the abnormal V/I at $I \approx 100$ µA. I thus discarded data of V/I measured at 100 µA. The diameter of the Au bulk particle is between 1.5 and 3 µm, which is of similar length scale as d (~1.6 µm, **Figure A13b**). **Equation 5.3** is thus not valid for the Au particles. A new more complex formula would be required for the exact conductivity calculation, but it is not yet completed. The completion will be an outlook of this work.

5.3.3 Conductivity measurement of FIB deposited Pt electrodes

The Pt electrodes deposited by FIB is used to connect the particle and the four Ti-Au electrodes, as shown previously. To measure the conductivity of the particles, contact between the Pt electrodes and the Ti-Au electrodes needs to be ohmic. I therefore measure the resistance R between two Ti-Au electrodes connected by FIB deposited Pt electrodes (**Figure 5.6**). R is ~120 Ω with a small deviation. The resistivity ρ of FIB deposited Pt is 2 – 3 orders of magnitude higher than that of

pure Pt.[100] Hence if the contact between the Ti-Au electrode and Pt electrode is ohmic, R is determined by ρ and the dimension of the Pt electrode,

$$\rho = R\frac{a}{l}, \tag{5.2}$$

where a is the cross-sectional area and l is the length of the resistor. According to the dimension of Pt and Ti-Au electrodes, l = 700 nm and a = 700 x 200 = 1.4 x 10^5 nm^2. The calculated ρ is thus ~2.4 x 10^{-3} Ω cm, which is two orders of magnitude higher than that of pure Pt (1.04 x 10^{-5} Ω cm[126]). This result is in good agreement with literature, meaning that the deposited Pt electrode is in ohmic contact with the pre-evaporated Ti-Au electrodes. This validates the conductivity measurements of single particles by top contact.

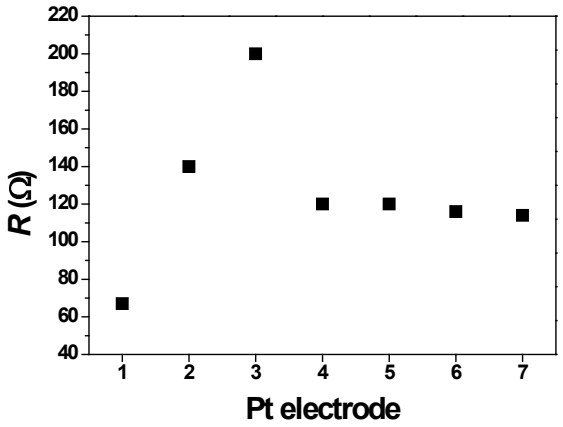

Figure 5.7. Resistance between Ti-Au electrodes connected by FIB deposited Pt electrodes.

5.4 Summary and conclusions

In this chapter, I have demonstrated nanoscopic conductivity measurement of single core-shell and bulk particles by microscopic four-point probe method. In the bottom contact, the contact resistance dominates the measured V/I; while in the top contact, the contact resistance can be neglected. Using the top contact geometry, I measured V/I values of both, Ag core-shell particles and Au bulk particles. The

conductivity of Ag core-shell particles is ~0.1 S/cm. The inhomogeneous Ag layer and the vulcanization of Ag in air are the two possible reasons for this low conductivity. The *V*/*I* value of bulk Au particles is ~100 Ω. An ad-hoc formula is required for the conductivity calculation of bulk particles, which will be accomplished in the near future. The final aim of this study is to measure the conductivity of single particles (bulk and core-shell) of conjugated polymers with a diameter of several micrometers, which will be performed in the near future.

Chapter 6 Concluding Remarks

6.1 Summary and conclusions

In this thesis I addressed the topographic, electric (surface potential and conductivity), and dielectric (dielectric constant) characterization of thin films of a conjugated polymer blend, PPy:PSS. The methods I used were scanning probe techniques, in particular atomic force microscopy (AFM), Kelvin probe force microscopy (KPFM), and scanning conductive torsional mode microscopy (SCTMM).

I started with a combined KPFM and SCTMM study on a model system of gold nanoparticles (AuNPs) embedded in a thin polystyrene (PS) film to combine the advantages of both techniques (**Chapter 3**). I varied the arrangements of AuNPs in the PS film to mimic the structure of a conjugated polymer blend, PPy:PSS. KPFM measurements on individual AuNPs reveal that the measured surface potential is influenced by the embedding depth and by the dielectric properties of the non-conductive PS film. KPFM measurements on clusters of AuNPs reveal that the measured surface potential of an AuNP is influenced as well by the surface potential of the AuNPs surrounding it (a halo is seen on the surface potential image). The lateral resolution of KPFM is thus reduced (for such a system) to several hundred nanometers. This makes it difficult to investigate morphological or structural data of nanoscopic features. Analyzing the same sample by SCTMM, however, provides complementary information. The study on individual AuNPs tells when the PS film is too thick to allow for current flow, while the study on clusters tells where percolation channels are formed.

With information gained from the Au/PS model system, I interpreted KPFM and SCTMM results of thick PPy:PSS films (~80 nm). The complementary KPFM and SCTMM study helps me to correlate the round domains in the height image to the conductive PPy domains (20 – 30 nm in diameter), and the surroundings to the non-conductive PSS matrix. The difference in the surface potential and current signal of the PPy domains reveals that each PPy domain consists of smaller PPy sub-domains (<10 nm). The formation of PPy domains (instead of homogeneously dispersed in the PSS matrix) is due to poor compatibility between PPy (more hydrophobic) and PSS (more hydrophilic) during the synthesis. And the size of the domains is consistent with data obtained by dynamic light scattering measurements.

As a water based polymer blend, the content of water also influences the morphologic, electric (surface potential) and dielectric (dielectric constant) properties of PPy:PSS films (thick and thin ones). This, I demonstrated by KPFM in the $F_{2\omega}$-mode (**Chapter 4**). $F_{2\omega}$ is used to measure changes of the dielectric constant, which in turn is sensitive to water. I investigated a series of PPy:PSS films upon changing relative humidity (RH). The topography of unannealed thick films (~60 nm) changed at high RH (~90%) due to the swelling of PSS, while that of annealed films remained almost unchanged. This is due to the reduced water sorption of the annealed PSS. The surface potential and the dielectric constant of thick films also changed for both annealed and unannealed ones upon changing RH. To understand the mechanism of the influence of RH on the morphology and on the electric properties, I performed a similar KPFM study on thin PPy:PSS films.

The KPFM results (changes of topography and dielectric constants upon RH) of thin PPy:PSS films are consistent with those of thick ones. Changes of topography of unannealed thin films were irreversible due to swelling and dewetting of the PSS on HOPG. The swelling of the PSS also changed the surface composition of PPy:PSS films (local rearrangement of PPy and PSS). This rearrangement could only be detected by $F_{2\omega}$-imaging, and not by the "standard"

KPFM surface potential imaging. $F_{2\omega}$-imaging is thus more sensitive to water sorption than the topographic imaging. The annealed PPy:PSS films (both thin and thick ones) exhibit stronger resistance to water sorption. This explains why the device performance of devices based on conjugated polymers is improved after thermal annealing.

Due to the electro-coupling between PPy and PSS, the conductivity of PPy domains may change after they are embedded in the PSS matrix. To characterize the conductivity of single PPy particles with a diameter of a few micrometers, I developed a microscopic four-point probe method (**Chapter 5**). I started with metal and metal coated particles as models, and measured their conductivities by two geometries of the electrode array, i.e. "bottom contact" and "top contact". In the bottom contact geometry, the four contact areas between the particle and the electrodes, and the distance between the neighboring electrodes are different. The measured values of *V*/*I* (several TΩ) were thus dominated by the contact resistance not the conductivity of the particles. Using the top contact geometry, I was able to control more precisely the contact area and the distance between two neighboring electrodes. I measured values of *V*/*I* of both Ag core-shell particle (~100 kΩ) and Au bulk particle (~100 Ω). The conductivity of the Ag core-shell particle (~0.1 S/cm) is lower than that of pure Ag (6.3 x 10^5 S/cm). The vulcanization of Ag in air (~50 % of Ag) and the inhomogeneous Ag layer (nanoscopic domains) are the two reasons for the lower conductivity of these particles. The geometry of the Ag (core-shell) and Au (bulk) particles are different. A new formula is thus required to calculate the conductivity of the Au bulk particles from the measured values of *V*/*I*.

6.2 Outlook

I have demonstrated that KPFM and SCTMM are powerful characterization methods for resolving nanoscopic topographic and electric properties of conjugated polymer blends. The techniques and the way of combining KPFM and SCTMM to

characterize thin films are not restricted to the PPy:PSS blend only. They could be extended to other blends, e.g. P3HT:PVBM or PEDOT:PSS.

KPFM and SCTMM can also be extended to measurements on films incorporated in active devices, e.g. planar devices with electrodes connected to a conjugated polymer blend like PPy:PSS. By measuring surface potential (on and off) at the interface of the electrode and the thin film of polymers or polymer blends, one could study the charge transport mechanism. By this method one could also obtain spatial information of the space charge region. This study, together with the studies I introduce in this thesis, can be used to predict macroscopic device performance of organic semiconductors.

The dielectric imaging is now based on the detection of $\Delta A_{2\omega}$. In such a detection mode $F_{2\omega}$ is not directly measured, as explained in **Section 1.4.3**. $F_{2\omega}$ contains information on tip geometry and dielectric constant of samples. For the next step, one could calculate $F_{2\omega}$ from $\Delta A_{2\omega}$, according to some physical parameters (i.e. spring constant, quality factor) of the cantilever and the sensitivity of the photo diode detector. The dielectric constant of materials could thus be extracted from $F_{2\omega}$ by solving **Equation 4.2**. By this way one could obtain a direct nanoscopic mapping of the dielectric constant of samples.

I have demonstrated the conductivity measurement of metal particles with a microscopic four-point probe method. One could extend its application to measurements of conductive polymer particles (both core-shell and bulk ones), e.g. PPy based particles. By comparing the conductivity of single core-shell particles and the thin films they form, one could gain deeper understand of electrical properties of conductive colloidal particles.

Symbols and Abbreviations

A	amplitude
a	area
C	capacitance
	constant
d	diameter
	distance
	thickness
$đ$	average diameter
E	energy
	elastic modulus
e	elementary charge
F	force
f	frequency
h	height
I	current
k	spring constant
l	length
m	mass
M_n	number averaged molecular weight
M_w	weight averaged molecular weight
Q	charge
$\mathbf{Q}$	quality factor
r	distance
R	resistance
t	time

	thickness
V	voltage
	potential
z	tip-sample distance
ε_0	vacuum permittivity
ε_f	Fermi level energy
ε_r	relative permittivity
ε_{Vac}	vacuum level energy
$\hbar$	reduced Planck constant
ρ	resistivity
σ	conductivity
Φ	work function
φ	phase
ω	modulation frequency
2D	two dimensional
3D	three dimensional
AC	alternating current
AFM	atomic force microscopy
AM	amplitude modulation
AuNP	gold nanoparticle
c-AFM	conductive atomic force microscopy
DC	direct current
EDX	energy dispersive x-ray spectroscopy
FET	field effect transistor
FIB	focus ion beam
FM	frequency modulation
ITO	indium tin oxide
KPFM	Kelvin probe force microscopy
MEH-PPV	poly[2-methoxy,5-(2'-ethyl-hexyloxy)-p-phenylene

	vinylene]
OLED	organic light-emitting diode
P3HT	poly(3-hexylthiophene)
PCBM	6,6-phenyl-C_{61} butyric acid methyl ester
PEDOT	poly(3,4-ethylenedioxythiophene)
pH	potential for hydrogen ion concentration
PPV	poly(p-phenylene vinylene)
PPy	Polypyrrole
PS	polystyrene
PSS	poly(styrenesulfonate)
PSSH	poly(styrene sulfonic acid)
RH	relative humidity
RMS	root mean square
SAXS	small angle x-ray spectroscopy
SCTMM	scanning conductive torsional mode microscopy
SEM	scanning electron microscopy
STM	scanning tunneling microscopy
TEM	transmission electron microscopy
UHV	ultra high vacuum
UPS	ultraviolet photoelectron spectroscopy
WAXS	wide angle x-ray spectroscopy
XPS	x-ray photoelectron spectroscopy
XRD	x-ray diffraction

Appendix

A.1 Materials

The hydrodynamic radius of PPy:PSS was measured by dynamic light scattering in the group of Polymeranalytik by Christine Rosenauer. The wavelength of the laser beam is 632.8 nm. The dielectric spectroscopy measurements were performed by Konstantinos Mpoukouvalas.

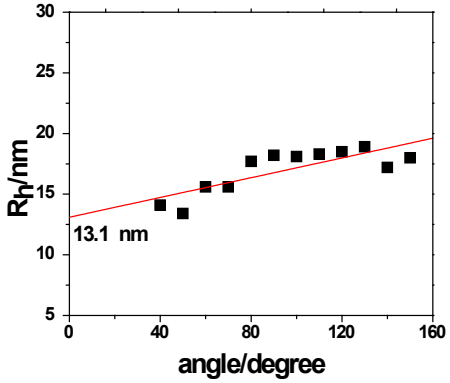

Figure A1. Hydrodynamic radius versus scanning angle.

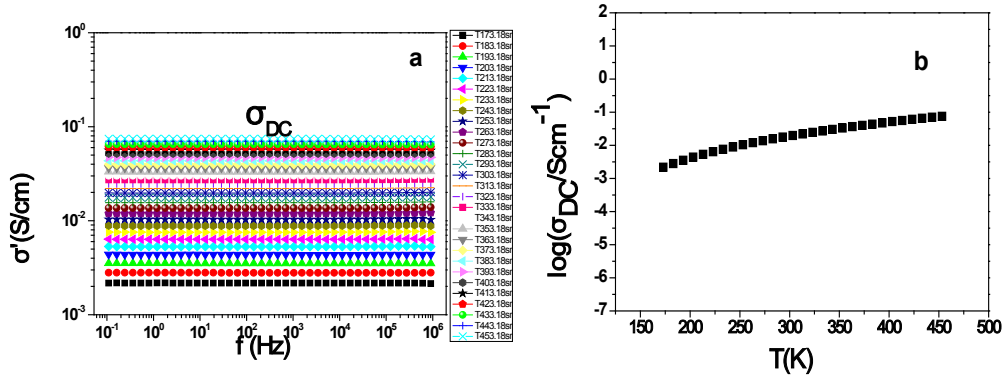

Figure A2. Dielectric spectroscopy of σ' versus frequency (a) and DC conductivity versus temperature (b).

A.2 Thickness measurement

To measure the thickness of a thin film (<150 nm), I scratched the film by a sharp needle and measured the surface profile across the scratch by tapping mode AFM (Dimension D3100 cl) with silicon cantilevers (OMLAC240 TN). The scan rate was set to be 0.8 Hz.

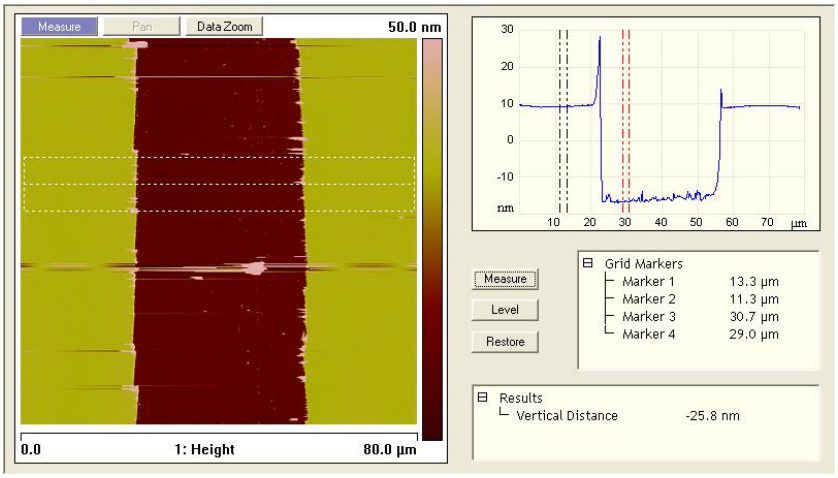

Figure A3. Thickness measurement of the PS film by step-height analysis.

A.3 Cantilevers

A.3.1 SEM images of cantilevers used in **Chapter 2** and **Chapter 3**

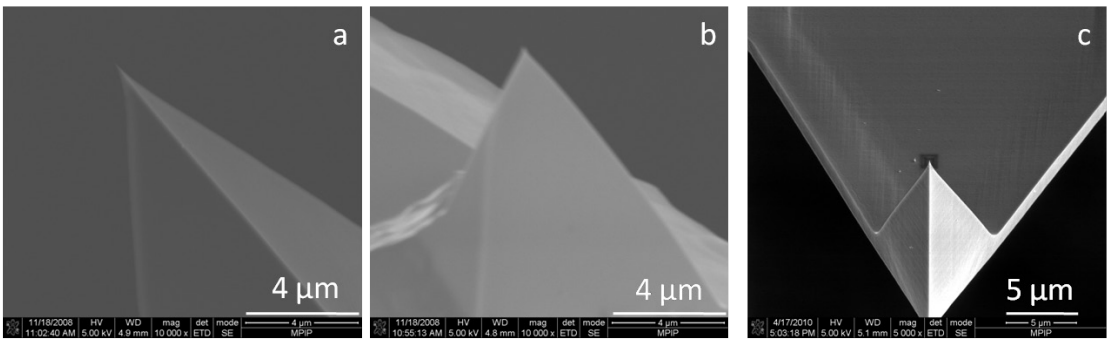

Figure A4 SEM images of different cantilevers before measurements: a) 70 kHz silicon cantilever; b) 70 kHz Pt-Ir coated conductive cantilever; c) 70 kHz Pt-Ti coated conductive cantilever.

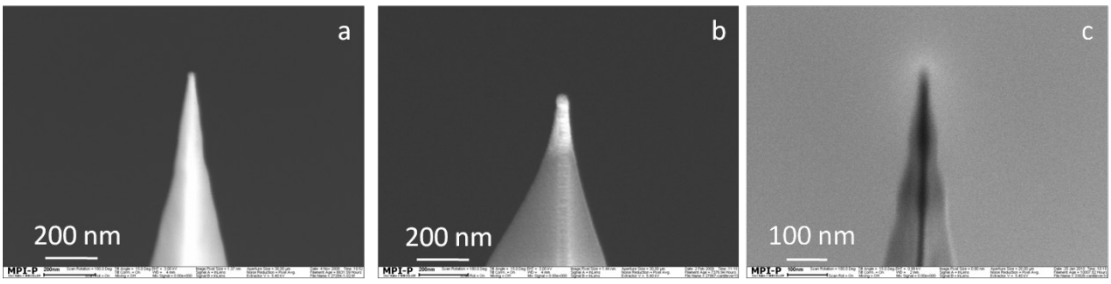

Figure A5 Representative SEM images of different cantilevers after measurements: a) 70 kHz silicon cantilever; b) 70 kHz Pt-Ir coated conductive cantilever; c) 70 kHz Pt-Ti coated conductive cantilever. SEM images in this figure were obtained by Maren Müller.

A.3.2 Work function and conductivity measurements of Pt-Ir cantilever

Work function and conductivity measurements of the Pt-Ir cantilevers were performed on freshly cleaved HOPG. The work function of the Pt-Ir cantilevers was calculated according to **Equation 1.6**.

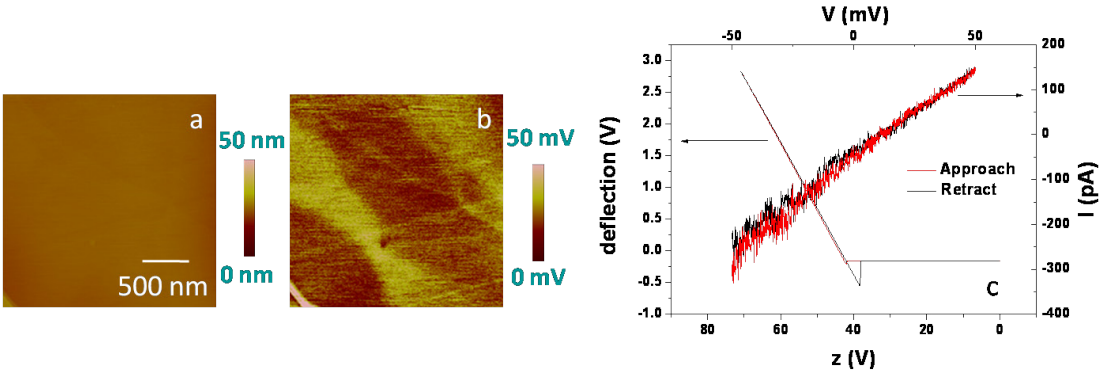

Figure A6. a) and b) representative height and surface potential images of HOPG measured by a Pt-Ir cantilever; c) representative *I-V* curve and deflection-distance curve of a Pt-Ir tip measured on HOPG.

A.4 Complementary information on Chapter 3

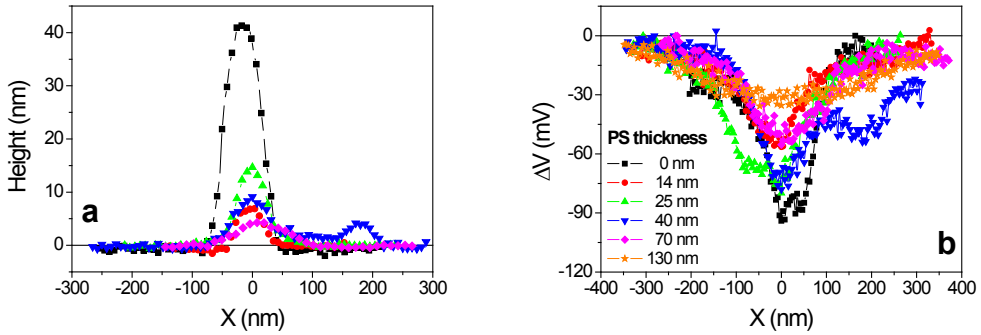

Figure A7. Cross-section profiles of topography (a) and surface potential (b) on samples with different *t*.

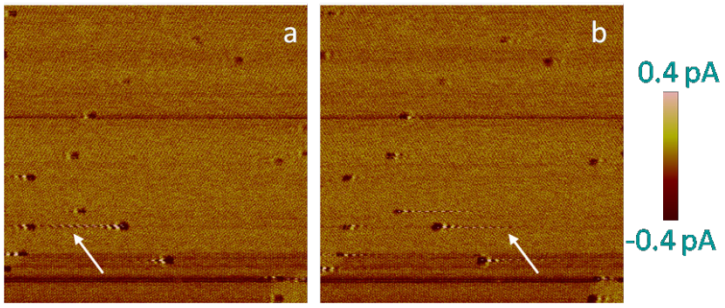

Figure A8. Current images of naked AuNPs on silicon substrate: a) recorded by the 'retrace' channel; b) recorded by the 'trace' channel.

A.5 Complementary information on Chapter 4

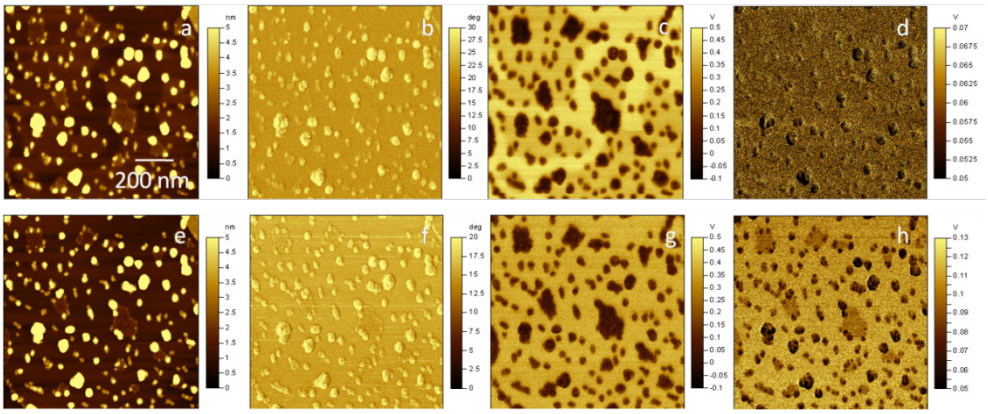

Figure A9. Height (a and e), phase (b and f), surface potential (c and g), and dielectric images (d and h) of unannealed thin PPy:PSS film: a), b), c) and d) in air, RH ≈ 20%; e), f), g) and h) in nitrogen, RH ≈ 8%.

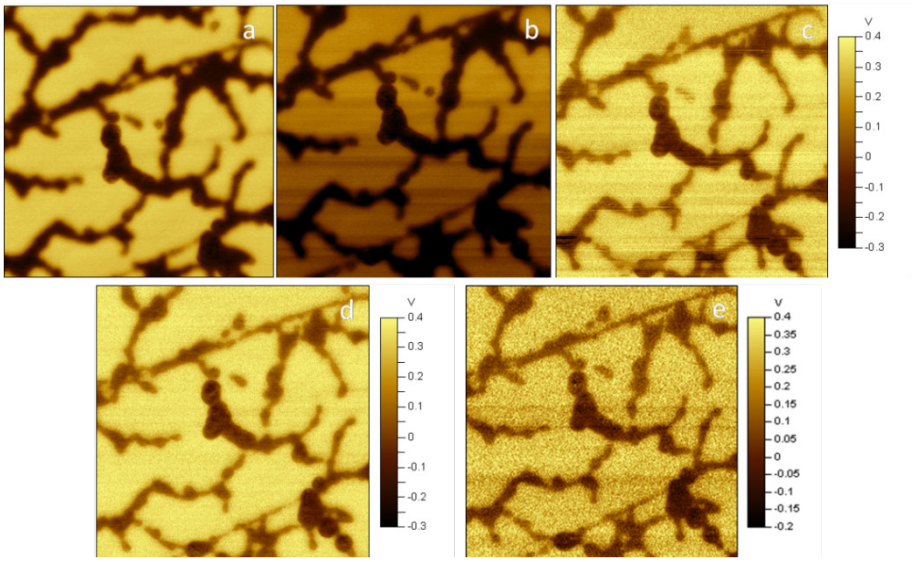

Figure A10. Surface potential images of unannealed thin PPy:PSS film at different RH: a) the 1st dry state, RH = 7%; b) RH = 50%; c) the 1st swollen state, RH = 80%; d) the 2nd dry state, RH = 7%; e) the 2nd swollen state, RH = 80%.

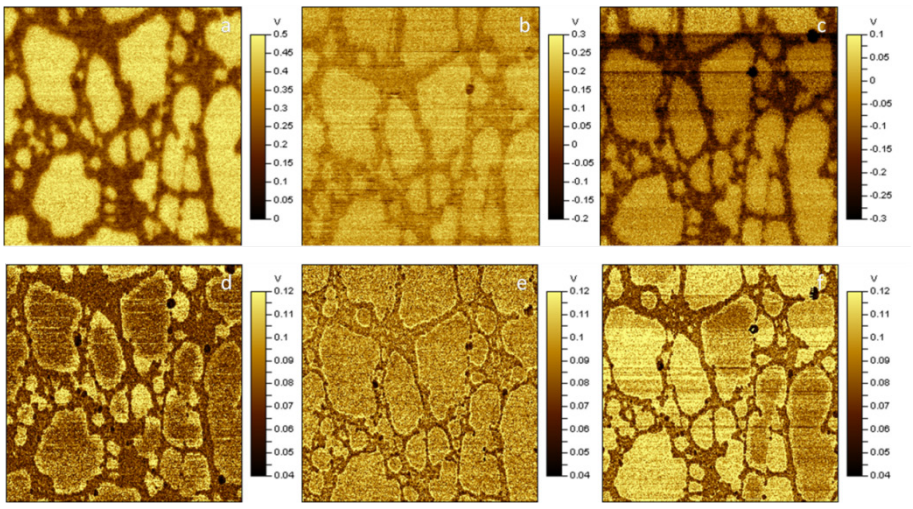

Figure A11. Surface potential (a, b, and c) and dielectric images (d, e, and f) of annealed thin PPy:PSS film at different RH: a) and d) the 1st dry state, RH = 7%; b) and e) the 1st swollen state, RH = 90%; c) the 2nd dry state, RH = 5%.

A.6 Complementary information on Chapter 5

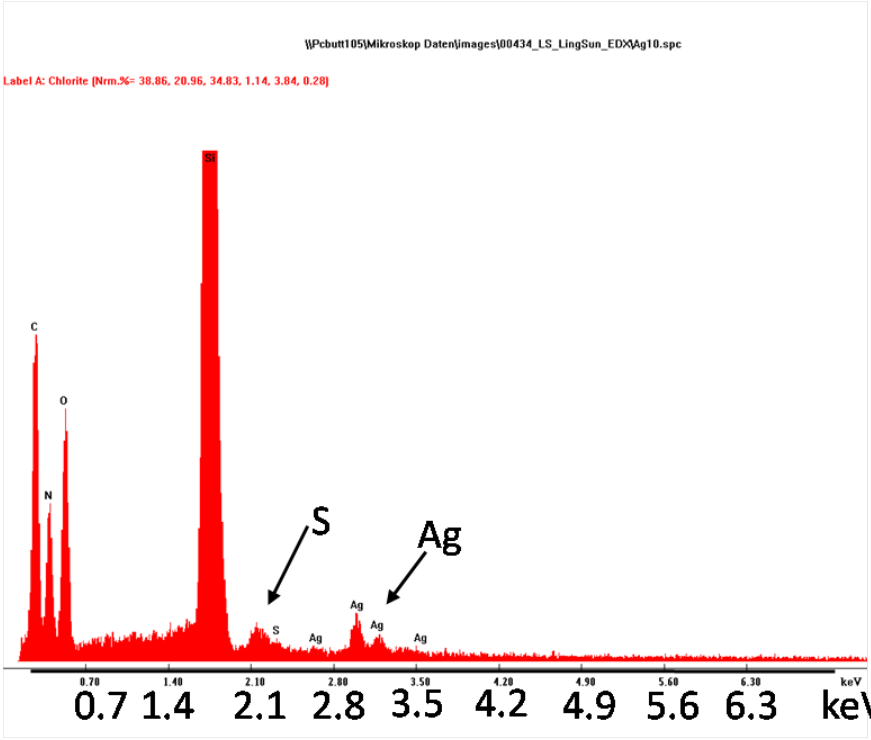

Figure A12. Representative EDX spectra of an Ag core-shell particle.

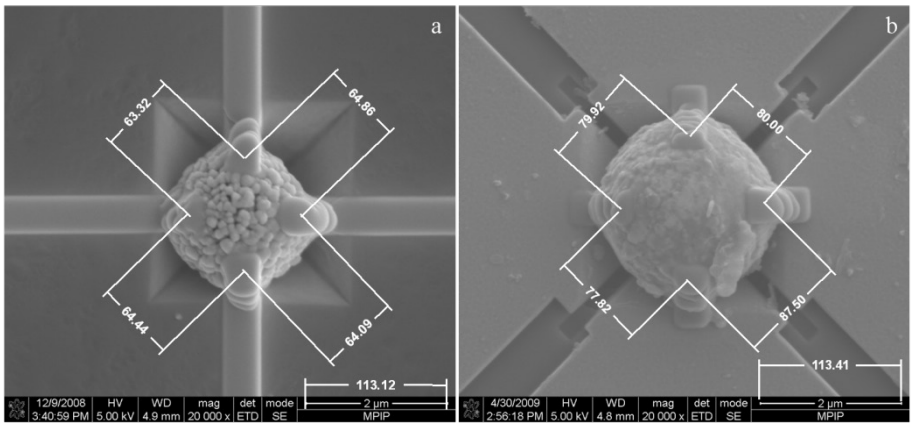

Figure A13. Representative SEM images of an Ag core-shell (a) and an Au bulk (b) particles in contact with four Pt electrodes.

Bibliography

(1) Ito, T.; Shirakaw.H; Ikeda, S. *J Polym. Sci. Part A:Polym. Chem.* **1974**, *12*, 11.
(2) Sariciftci, N. S.; Smilowitz, L.; Heeger, A. J.; Wudl, F. *Science* **1992**, *258*, 1474.
(3) Chiang, C. K.; Fincher, C. R.; Park, Y. W.; Heeger, A. J.; Shirakawa, H.; Louis, E. J.; Gau, S. C.; Macdiarmid, A. G. *Phys. Rev. Lett.* **1977**, *39*, 1098.
(4) Cornil, J.; Beljonne, D.; Calbert, J. P.; Bredas, J. L. *Adv. Mater.* **2001**, *13*, 1053.
(5) Li, Y. F.; Hou, J. H. *Major Classes of Conjugated Polymers and Synthetic strategies*; CRC Press: Boca Raton, **2008**.
(6) Moons, E. *J. Phys.-Condes. Matter* **2002**, *14*, 12235.
(7) Kros, A.; Nolte, R. J. M.; Sommerdijk, N. *Adv. Mater.* **2002**, *14*, 1779.
(8) Singh, T. B.; Sariciftci, N. S. *Annu. Rev. Mater. Research* **2006**, *36*, 199.
(9) Kus, M.; Okur, S. *Sens. Actuator B-Chem.* **2009**, *143*, 177.
(10) Ito, T.; Shirakawa, H.; Ikeda, S. *J Polym. Sci. Part A:Polym. Chem.* **1975**, *13*, 1943.
(11) Street, G. B.; Clarke, T. C. *IBM J. Res. Dev.* **1981**, *25*, 51.
(12) Wernet, W.; Wegner, G. *Makromol. Chem.:Macromol. Chem. Phys.* **1987**, *188*, 1465.
(13) Wienk, M. M.; Kroon, J. M.; Verhees, W. J. H.; Knol, J.; Hummelen, J. C.; van Hal, P. A.; Janssen, R. A. J. *Angew. Chem.Int. Ed.* **2003**, *42*, 3371.
(14) Chen, H. Y.; Hou, J. H.; Zhang, S. Q.; Liang, Y. Y.; Yang, G. W.; Yang, Y.; Yu, L. P.; Wu, Y.; Li, G. *Nat. Photonics* **2009**, *3*, 649.
(15) Giridharagopal, R.; Ginger, D. S. *J. phys. Chem. Lett.* **2010**, *1*, 1160.
(16) Nardes, A. M., *Dissertation*, Technische Universiteit Eindhoven and University of Sao Paulo, **2007**.
(17) Elschner, A.; Bruder, F.; Heuer, H. W.; Jonas, F.; Karbach, A.; Kirchmeyer, S.; Thurm, S. *Synth. Met.* **2000**, *111*, 139.
(18) Kirchmeyer, S.; Reuter, K. *J. Mater. Chem.* **2005**, *15*, 2077.
(19) Lee, T. W.; Chung, Y.; Kwon, O.; Park, J. J. *Adv. Funct. Mater.* **2007**, *17*, 390.
(20) de Kok, M. M.; Buechel, M.; Vulto, S. I. E.; van de Weijer, P.; Meulenkamp, E. A.; de Winter, S.; Mank, A. J. G.; Vorstenbosch, H. J. M.; Weijtens, C. H. L.; van Elsbergen, V. *Phys. Status Solidi A-Appl. Res.* **2004**, *201*, 1342.
(21) de Jong, M. P.; van Ijzendoorn, L. J.; de Voigt, M. J. A. *Appl. Phys. Lett.* **2000**, *77*, 2255.
(22) Chen, L. M.; Xu, Z.; Hong, Z. R.; Yang, Y. *J. Mater. Chem. 20*, 2575.
(23) Yan, H.; Lee, P.; Armstrong, N. R.; Graham, A.; Evmenenko, G. A.; Dutta, P.; Marks, T. J. *JACS* **2005**, *127*, 3172.
(24) Wang, J. J.; Sun, L.; Mpoukouvalas, K.; Fassbender, B.; Bonaccurso, E.;

Brunklaus, G.; Muehlebach, A.; Rime, F.; Butt, H. J.; Wegner, G. *Macromol. Chem. Phys.* **2009**, *210*, 1504.

(25) Wang, J. J.; Sun, L.; Mpoukouvalas, K.; Lienkamp, K.; Lieberwirth, I.; Fassbender, B.; Bonaccurso, E.; Brunklaus, G.; Muehlebach, A.; Beierlein, T.; Tilch, R.; Butt, H. J.; Wegner, G. *Adv. Mater.* **2009**, *21*, 1137.

(26) Muhlebach, A.; Hafner, A.; Rime, F.; Mpoukouvalas, K.; Sun, L.; Wang, J. J.; Wegner, G.; Beierlein, T. *Chimia* **2010**, *64*, 49.

(27) Goodhew, P. J.; Humphreys, J.; Beanland, R. *Electron Microscopy and Analysis*; Taylor and Francis: London, New York, **2001**.

(28) Yamamoto, T.; Arai, M.; Kokubo, H.; Sasaki, S. *Macromolecules* **2003**, *36*, 7986.

(29) Hou, J. H.; Huo, L. J.; He, C.; Yang, C. H.; Li, Y. F. *Macromolecules* **2006**, *39*, 594.

(30) Woo, C. H.; Thompson, B. C.; Kim, B. J.; Toney, M. F.; Frechet, J. M. J. *J. Am. Chem. Soc.* **2008**, *130*, 16324.

(31) Olsen, B. D.; Segalman, R. A. *Macromolecules* **2005***, 38,* 10127.

(32) Chiu, M. Y.; Jeng, U. S.; Su, C. H.; Liang, K. S.; Wei, K. H. *Adv. Mater.* **2008**, *20*, 2573.

(33) Siegbahn, K. M. *Nobel Lectures: Physics* **1981**.

(34) Koch, N.; Vollmer, A.; Elschner, A. *Appl. Phys. Lett.* **2007**, *90* 4351.

(35) Germack, D. S.; Chan, C. K.; Hamadani, B. H.; Richter, L. J.; Fischer, D. A.; Gundlach, D. J.; DeLongchamp, D. M. *Appl. Phys. Lett.* **2009**, *94* 23330.

(36) Prater, C. B.; Butt, H. J.; Hansma, P. K. *Nature* **1990**, *345*, 839.

(37) Pingree, L. S. C.; Reid, O. G.; Ginger, D. S. *Adv. Mater.* **2009**, *21*, 19.

(38) Ishida, T.; Mizutani, W.; Choi, N.; Akiba, U.; Fujihira, M.; Tokumoto, H. *J. Phys. Chem. B* **2000**, *104*, 11680.

(39) Nardes, A. M.; Kemerink, M.; Janssen, R. A. J.; Bastiaansen, J. A. M.; Kiggen, N. M. M.; Langeveld, B. M. W.; van Breemen, A.; de Kok, M. M. *Adv. Mater.* **2007**, *19*, 1196.

(40) Kemerink, M.; Alvarado, S. F.; Muller, P.; Koenraad, P. M.; Salemink, H. W. M.; Wolter, J. H.; Janssen, R. A. J. *Phys. Rev. B* **2004**, *70*, 13.

(41) Berger, R.; Butt, H.-J.; Retschke, M.; Weber, S. *Macromol. Rapid Commun.* **2009**, *30*, 1167.

(42) Sun, L.; Wang, J. J.; Bonaccurso, E. *J. Phys. Chem. C* **2010**, *114*, 7161.

(43) Weber, S.; Haberkorn, N.; Theato, P.; Berger, R. *Nano Lett.* **2010** *10*, 1194.

(44) Chiesa, M.; Burgi, L.; Kim, J. S.; Shikler, R.; Friend, R. H.; Sirringhaus, H. *Nano Lett.* **2005**, *5*, 559.

(45) Palermo, V.; Palma, M.; Samori, P. *Adv. Mater.* **2006**, *18*, 145.

(46) Jacobs, H. O.; Leuchtmann, P.; Homan, O. J.; Stemmer, A. *J. Appl. Phys.* **1998**, *84*, 1168.

(47) Charrier, D. S. H.; Kemerink, M.; Smalbrugge, B. E.; de Vries, T.; Janssen, R. A. J. *ACS Nano* **2008**, *2*, 622.

(48) Kawano, K.; Pacios, R.; Poplavskyy, D.; Nelson, J.; Bradley, D. D. C.; Durrant, J. R. *Sol. Energy Mater. Sol. Cells* **2006**, *90*, 3520.

(49) Okuzaki, H.; Kondo, T.; Kunugi, T. *Polymer* **1999**, *40*, 995.
(50) Lv, X.; Hong, L. J.; Li, Y.; Yang, M. J. *J. Appl. Polym. Sci.* **2009**, *112*, 1287.
(51) Okuzaki, H.; Suzuki, H.; Ito, T. *Synth. Met.* **2009**, *159*, 2233.
(52) Benitez, J. J.; de la Fuente, O. R.; Diez-Perez, I.; Sanz, F.; Salmeron, M. *J. Chem. Phys.* **2005**, *123* 10470.
(53) Lu, W.; Xiong, Y.; Hassanien, A.; Zhao, W.; Zheng, M.; Chen, L. W. *Nano Lett.* **2009**, *9*, 1668.
(54) Vernitskaya, T. V.; Efimov, O. N. *Russian Chem. Rev.* **1997**, *66*, 443.
(55) Cui, X. D.; Primak, A.; Zarate, X.; Tomfohr, J.; Sankey, O. F.; Moore, A. L.; Moore, T. A.; Gust, D.; Harris, G.; Lindsay, S. M. *Science* **2001**, *294*, 571.
(56) Cabrini, S.; Barsotti, R. J.; Carpentiero, A.; Businaro, L.; Zaccaria, R. P.; Stellacci, F.; Di Fabrizio, E.; A V S Amer Inst Physics: Orlando, FL, **2005**, p 2806.
(57) Haiss, W.; Wang, C. S.; Grace, I.; Batsanov, A. S.; Schiffrin, D. J.; Higgins, S. J.; Bryce, M. R.; Lambert, C. J.; Nichols, R. J. *Nat. Mater.* **2006**, *5*, 995.
(58) Roy, S.; Vedala, H.; Roy, A. D.; Kim, D. H.; Doud, M.; Mathee, K.; Shin, H. K.; Shimamoto, N.; Prasad, V.; Choi, W. B. *Nano Lett.* **2008**, *8*, 26.
(59) Binnig, G.; Quate, C. F.; Gerber, C. *Phys. Rev. Lett.* **1986**, *56*, 930.
(60) Binnig, G.; Rohrer, H. *Helv. Phys. Acta* **1982**, *55*, 726.
(61) Schwoerer, M.; Wolf, H. C. *Organic Molecular Solids*; Willey-VCH: Weinheim, 2007.
(62) Chen, C. J. *Phys. Rev. Lett.* **1990**, *65*, 448.
(63) Binnig, G.; Quate, C. F.; Gerber, C. *Phys. Rev. Lett.* **1986**, *56*, 930.
(64) Martin, Y.; Williams, C. C.; Wickramasinghe, H. K. *J. Appl. Phys.* **1987**, *61*, 4723.
(65) Zhong, Q.; Inniss, D.; Kjoller, K.; Elings, V. B. *Surf. Sci.* **1993**, *290*, L688.
(66) Albrecht, T. R.; Grutter, P.; Horne, D.; Rugar, D. *J. Appl. Phys.* **1991**, *69*, 668.
(67) Prater, C. B.; Maivald, P. G.; Kjoller, K. J.; Heaton, M. G. *Tapping Mode Imaging Applications and Technology*, Veeco application notes AN04, Rev A1.
(68) Garcia, R.; Perez, R. *Surf. Sci. Rep.* **2002**, *47*, 197.
(69) Olbrich, A.; Ebersberger, B.; Boit, C. *Appl. Phys. Lett.* **1998**, *73*, 3114.
(70) Houze, F.; Meyer, R.; Schneegans, O.; Boyer, L. *Appl. Phys. Lett.* **1996**, *69*, 1975.
(71) Yang, R. Q.; Garcia, A.; Korystov, D.; Mikhailovsky, A.; Bazan, G. C.; Nguyen, T. Q. *JACS* **2006**, *128*, 16532.
(72) Harris, P.; Huang, L.; Su, C. *Electical testing of soft delicate samples using Torsional Resonance Mode and TUNA*, Veeco application notes AN107, **2007**.
(73) Huang, L.; Su, C. M. *Ultramicroscopy* **2004**, *100*, 277.
(74) Song, Y.; Bhushan, B. *J Appl. Phys.* **2006**, *99*, 94911.
(75) Glatzel, T.; Lux-Steiner, M. C.; Strassburg, E.; Boag, A.; Rosenwaks, Y. *Principles of Kelvin Probe Force Microscopy*; Springer, **2007**; Vol. 1.
(76) Schönenberger, C.; Alvarado, S. F. *Phys. Rev. Lett.* **1990**, *65*, 3162.

(77) Hudlet, S.; Saintjean, M.; Roulet, B.; Berger, J.; Guthmann, C. *J. Appl. Phys.* **1995**, *77*, 3308.
(78) Liscio, A.; Palermo, V.; Gentilini, D.; Nolde, F.; Mullen, K.; Samori, P. *Adv. Funct. Mater.* **2006**, *16*, 1407.
(79) Abraham, D. W.; Williams, C.; Slinkman, J.; Wickramasinghe, H. K. *J. Vac. Sci. Technol. B* **1991**, *9*, 703.
(80) Baumgart, C.; Helm, M.; Schmidt, H. *Phys. Rev. B* **2009**, *80*, 085305.
(81) Alexander, J.; Magonov, S.; Moeller, M. *J. Vac. Sci. Technol. B* **2009**, *27*, 903.
(82) Slinker, J. D.; DeFranco, J. A.; Jaquith, M. J.; Silveira, W. R.; Zhong, Y. W.; Moran-Mirabal, J. M.; Craighead, H. G.; Abruna, H. D.; Marohn, J. A.; Malliaras, G. G. *Nat. Mater.* **2007**, *6*, 894.
(83) Jacobs, H. O.; Knapp, H. F.; Muller, S.; Stemmer, A. *Ultramicroscopy* **1997**, *69*, 39.
(84) Magonov, S.; Alexander, J. *Advanced Atomic Force Microscopy: Exploring Measurements of Local Electric Properties*, Agilent technologies application note, 5989-9740EN, **2008**.
(85) Serry, F.; Kjoller, K.; Thornton, J.; Tech, R.; Cook, D. *Electric Force Microscopy, Surface Potential Imaging, and Surface Electric Modification with the Atomic Force Microscope (AFM)*, Vecco application notes AN27, **2004**.
(86) Agilent Technologies Inc., *Agilent 5500 User's Guide*, N9410-90001, **2008**.
(87) Kitamura, S.; Suzuki, K.; Iwatsuki, M. *Appl. Surf. Sci.* **1999**, *140*, 265.
(88) Zerweck, U.; Loppacher, C.; Otto, T.; Grafstrom, S.; Eng, L. M. *Phys. Rev. B* **2005**, *71* 12542.
(89) Lu, W.; Xiong, Y.; Chen, L. W. *J. Phys. Chem. C* **2009**, *113*, 10337.
(90) Verdaguer, A.; Sacha, G. M.; Luna, M.; Frank Ogletree, D.; Salmeron, M. *J. Chem. Phys.* **2005**, *123* 12470.
(91) Gomez-Monivas, S.; Saenz, J. J.; Carminati, R.; Greffet, J. J. *Appl. Phys. Lett.* **2000**, *76*, 2955.
(92) Frens, G. *Nature:Phys. Sci.* **1973**, *241*, 20.
(93) Bai, D.; Hardwick, C. L.; Berron, B. J.; Jennings, G. K. *J. Phys. Chem. B* **2007**, *111*, 11400.
(94) O'Neil, K. D.; Shaw, B.; Semenikhin, O. A. *J. Phys. Chem. B* **2007**, *111*, 9253.
(95) Mei, Y.; Lauterbach, K.; Hoffmann, M.; Borisov, O. V.; Ballauff, M.; Jusufi, A. *Phys. Rev. Lett.* **2006**, *97*, 4.
(96) FEI Company, *xT Nova NanoLab User's Manual*, 4022-262-52351, **2006**.
(97) This is the standard cleaning procedure of silicon wafer provided by Crys Tech GmbH.
(98) del Campo, A.; Boos, D.; Spiess, H. W.; Jonas, U. *Angew. Chem. Int. Ed.* **2005**, *44*, 4707.
(99) Mpoukouvalas, K.; Wang, J. J.; Tilch, R.; Butt, H. J.; Wegner, G. *J. Appl. Phys.* **2009**, *106* 6370.
(100) FEI Company, *Platinum Deposition Technical Note*, PN 4035-272-21851-B.
(101) Sommerhalter, C.; Matthes, T. W.; Glatzel, T.; Jager-Waldau, A.; Lux-Steiner,

M. C. *Appl. Phys. Lett.* **1999**, *75*, 286.
(102) Lide, D. R. *CRC Handbook of Chemistry and Physics*; CRC, Taylor & Francis: Boca Raton, **2006**.
(103) Periodic Table of Elements: Au, *Accessed on-line:09/05/2010*; http://EnvironmentalChemistry.com/yogi/periodic/Au.html.
(104) Atkins, P. W. *Physical Chemistry* 2nd ed.; repr. with corrections ed.; Oxford University Press: Oxford, **1984**.
(105) Michels, A.; Michels, C. *Philosoph. Mag.* **1932**, *13*, 1192.
(106) Bluhm, H.; Inoue, T.; Salmeron, M. *Surf. Sci.* **2000**, *462*, L599.
(107) Liscio, A.; Palermo, V.; Mullen, K.; Samori, P. *J. Phys. Chem. C* **2008**, *112*, 17368.
(108) Gao, C. Y.; Leporatti, S.; Moya, S.; Donath, E.; Mohwald, H. *Chem.-Eur. J.* **2003**, *9*, 915.
(109) Pingree, L. S. C.; MacLeod, B. A.; Ginger, D. S. *J. Phys. Chem. C* **2008**, *112*, 7922.
(110) Zhang, X. H.; Maeda, N.; Craig, V. S. J. *Langmuir* **2006**, *22*, 5025.
(111) Kohler, R.; Donch, I.; Ott, P.; Laschewsky, A.; Fery, A.; Krastev, R. *Langmuir* **2009**, *25*, 11576.
(112) Dubreuil, F.; Elsner, N.; Fery, A. *Eu. Phys. J. E* **2003**, *12*, 215.
(113) Vinogradova, O. I.; Andrienko, D.; Lulevich, V. V.; Nordschild, S.; Sukhorukov, G. B. *Macromolecules* **2004**, *37*, 1113.
(114) Cherniavskaya, O.; Chen, L. W.; Weng, V.; Yuditsky, L.; Brus, L. E. *J. Phys. Chem. B* **2003**, *107*, 1525.
(115) Kymakis, E.; Koudoumas, E.; Franghiadakis, I.; Amaratunga, G. A. J. *J. Phys. D-Appl. Phys.* **2006**, *39*, 1058.
(116) Huang, J. S.; Miller, P. F.; Wilson, J. S.; de Mello, A. J.; de Mello, J. C.; Bradley, D. D. C. *Adv. Funct. Mater.* **2005**, *15*, 290.
(117) Seemann, R.; Herminghaus, S.; Jacobs, K. *Phys. Rev. Lett.* **2001**, *86*, 5534.
(118) Valdes, L. B. *Proc. Inst. Radio Engrs* **1954**, *42*, 420.
(119) Smits, F. M. *Bell Syst. Tech. J.* **1958**, *37*, 711.
(120) van der Pauw, L. J. *Philips Res. Rep.* **1958**, *13*, 1.
(121) Andrienko, D.; *Four-point conductivity measurements of spherical nanoparticles*, unpublished results, **2009**.
(122) Periodic Table of Elements: Ag, *Accessed on-line:09/05/2010*; http://EnvironmentalChemistry.com/yogi/periodic/Ag.html.
(123) Dhumure, S. S.; Lokhande, C. D. *Mater. Chem. Phys.* **1991**, *27*, 321.
(124) Grozdanov, I. *Appl. Surf. Sci.* **1995**, *84*, 325.
(125) El-Nahass, M. M.; Farag, A. A. M.; Ibrahim, E. M.; Abd-El-Rahman, S. *Vacuum* **2004**, *72*, 453.
(126) Periodic Table of Elements: Pt, *Accessed on-line:09/05/2010*; http://EnvironmentalChemistry.com/yogi/periodic/Pt.html.

Publications

- L. Sun, J. Wang, E. Bonaccurso*, *J. Phys. Chem .C* **2010**, 114, 7161.
- A. Mulebach*, A. Hafner, F. Rime, K. Mpoukouvalas, L. Sun, J. Wang, G. Wegner, T. Beierlein, *CHIMIA* **2010**, *64*, 49.
- J. Wang,* L. Sun, K. Mpoukouvalas, K. Lienkamp, I. Lieberwirth, B. Fassbender, E. Bonaccurso, G. Brunklaus, A. Muehlebach, T. Beierlein, R. Tilch, H. J. Butt, G. Wegner*, *Adv. Matter.* **2009**, *21*, 1137.
- J. Wang*, L. Sun, K. Mpoukouvalas, B. Fassbender, E. Bonaccurso, G. Brunklaus, A. Muehlebach, F. Rime, H-J. Butt, G. Wegner, *Macromol. Chem. Phys.* **2009**, *210*, 1504.

- L. Sun, J. Wang, H-J. Butt, E. Bonaccurso*, *Influence of Relative Humidity on Nanoscopic Topography and Dielectric Constant of Thin Films of PPy:PSS*, submitted.
- L. Sun, D. Andrienko, J. Wang, H-J Butt, G. Wegner, E. Bonaccurso*, *Nanoscopic Conductivity Measurement of Single Particle by Four-point Probe Method*, in preparation.

Presentations in international conferences

2010

MRS Spring Conference, San Francisco, USA, 5 Apr. – 9 Apr. 2010:

L. Sun, J. Wang, E. Bonaccurso (oral presentation): *Nanoscale Electronic Properties of a Model System and of a Conjugated Polymer Compound by Kelvin Probe Force Microscopy and Scanning Conductive Torsion Mode Microscopy*

L. Sun, J. Wang, E. Bonaccurso (poster presentation): *Humidity Dependence Study on Electronic Property of PPy:PSS by Kelvin Probe Force Microscopy*

ELOPTO 2010, Mainz, Germany, 14 Mar. – 17 Mar. 2010:

L. Sun[1], J.J. Wang, G. Wegner, H-J. Butt, E. Bonaccurso (poster presentation): *Nanoscale Electronic Properties of a Model System and of a Conjugated Polymer Compound by KPFM and SCTMM*

2009

Scanning Probe Microscopies and Organic Materials XVII, 15 Jun. – 17 Jun. 2009:

L. Sun, E. Bonaccurso, J. Wang, A. Muehlebach, H-J. Butt, G. Wegner (oral presentation): *Electrical Property Study of Gold (Au)/Polystyrene (PS) System by Atomic Force Microscopy*

2008

EMRS 2008, Strasbourg, France, 26 May. – 30 May. 2008:

L. Sun, J. Wang, W. Cheng, E. Bonaccurso, A. Muehlebach, H-J. Butt, G. Wegner (poster presentation): *Characterization of Thin Films of Redispersible Polypyrrole Composite Nanoparticles*